Spin-Dependent Electronic Structure of Re- and W-Based Semiconducting Transition Metal Dichalcogenides

Philipp Maria Eickholt

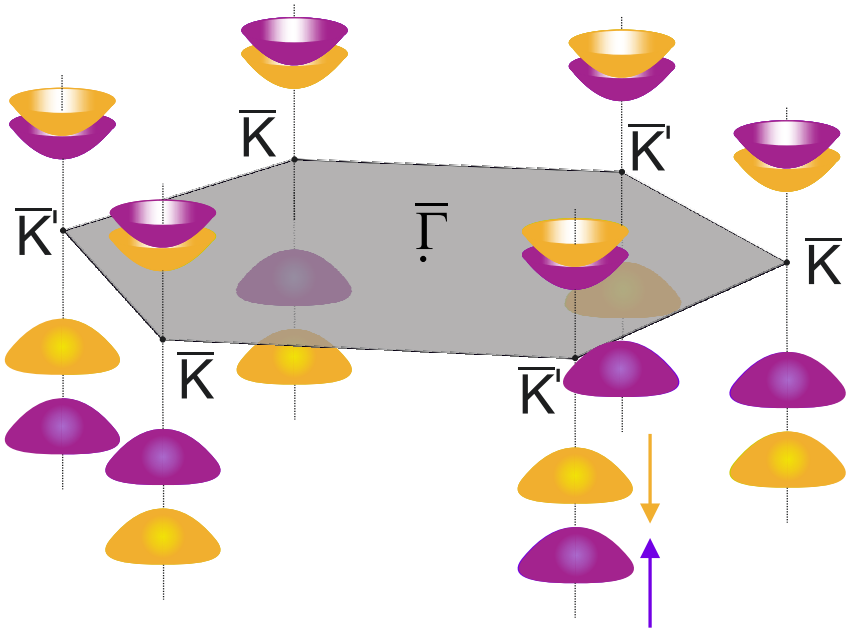

- 2019 -

WWU
MÜNSTER

Experimentelle Physik

Spin-Dependent Electronic Structure of Re- and W-Based Semiconducting Transition Metal Dichalcogenides

Inaugural-Dissertation
zur Erlangung des Doktorgrades
der Naturwissenschaften im Fachbereich Physik
der Mathematisch-Naturwissenschaftlichen Fakultät
der Westfälischen Wilhelms-Universität Münster

vorgelegt von

Philipp Maria Eickholt
aus Münster

- 2019 -

Dekan:	Prof. Dr. G. Wilde
Erster Gutachter:	Prof. Dr. M. Donath
Zweiter Gutachter:	apl. Prof. Dr. P. Krüger
Tag der mündlichen Prüfung:	28.06.2019
Tag der Promotion:	28.06.2019

Für Corinna

Cover: Sketch of the spin-dependent valley structure of the bands in single-layer WS_2 on Au(111) at the $\overline{K}$ and $\overline{K}'$ high-symmetry points. See Ch. 5 for details.

Abstract

The emphasis of this work is on the electronic structure of Re- and W- based semiconducting transition metal dichalcogenides. $ReSe_2$ has pronounced anisotropic optoelectronic properties, whereas single-layer WS_2 has a spin-dependent electronic structure. These attributes are highly appealing for electronic and optoelectronic devices. Of particular importance for the optoelectronic properties are the highest valence band, the lowest conduction band and the resulting band gap. The electronic structure of bulk $ReSe_2$ and single-layer WS_2 is experimentally accessed by spin- and angle-resolved photoemission and inverse photoemission for the occupied and unoccupied part, respectively.

In the case of $ReSe_2$, the present study reveals two valence band maxima with indistinguishable energy in the k_z-dependent band dispersion. One of them is located at the Z point, where the *GdW* calculation predicts the direct band gap. The other VBM appears at a non high-symmetry point in **k**-space along $\overline{\Gamma}$-$\overline{M}_1$. A conduction band minimum at $\overline{\Gamma}$ is found at 1.33 eV above the valence band maxima. Measurements of the occupied and unoccupied density of states point to a smaller fundamental band gap size than 1.33 eV. The anisotropic properties of $ReSe_2$ are reflected in the electronic structure. An anisotropic E vs $\mathbf{k}_{||}$ dispersion of the valence bands is observed. The direction perpendicular to the "diamond chains", i.e. $\overline{\Gamma}$-$\overline{M}_1$, has a much smaller bandwidth of the highest valence band than any other direction in **k**-space. Spin-resolved photoemission shows a remarkably high spin polarization of photoelectrons of up to 50% without background subtraction. This can partially be explained by a surface state that is identified in the data. However, the majority of the observed spin-polarization effects of photoelectrons is caused by the photoemission process.

Single-layer WS_2 is a non-centrosymmetric direct semiconductor. The total energy gap of single-layer WS_2/Au(111) is determined to 1.98 ± 0.04 eV, influenced by the screening of the Au substrate. The optoelectronic properties are dominated by the valence band maximum and conduction band minimum at the corner of the hexagonal Brillouin zone. Calculations and comparative measurements for bulk WS_2 show no significant influence of the Au substrate on the lowest conduction band and highest valence band of single-layer WS_2 at $\overline{\mathrm{K}}$ and $\overline{\mathrm{K}}'$. The valence band maximum is fully out-of-plane spin polarized at $\overline{\mathrm{K}}$. At $\overline{\mathrm{K}}'$ the same spin structure is observed, yet with opposite sign. The sign reversal of the spin polarization is also shown for the conduction bands. The valence band maximum is found to be spin split by 417 ± 23 meV, the conduction band minimum by 16 ± 7 meV. The sequence of the spin-split bands is the same below and above the Fermi level, i.e. the valence band maximum is oppositely out-of-plane spin-polarized than the conduction band minimum. As a consequence, the lowest transition is spin forbidden, i.e., optically dark. The first bright transition, involving the second conduction band, is 16 meV higher in energy than the band gap. The determined spin structure of the K valleys explains spin-forbidden "dark" excitons discussed in optical experiments.

Kurzfassung

Der Fokus dieser Arbeit liegt auf der elektronischen Struktur von Re- und W-basierten, halbleitenden Übergangsmetall-Dichalcogeniden. $ReSe_2$ weist ausgeprägt anisotrope opotoelektronische Eigenschaften auf, während Einzellagen WS_2 eine spinabhängige elektronische Struktur hat. Diese Eigenschaften machen die beiden Materialien zu vielversprechenden Kandidaten für elektronische und optoelektronische Bauelemente. Von besonderer Wichtigkeit sind dabei die Eigenschaften des höchsten Valenzbandes und des niedrigsten Leitungsbandes. Die elektronische Struktur wird in dieser Arbeit experimentell mit spin- und winkelaufgelöster Photoemission sowie spin- und winkelaufgelöster Inverser Photoemission im besetzten und unbesetzten Bereich untersucht.

Im Fall von volumenartigem $ReSe_2$ wurden zwei Valenzband Maxima mit ununterscheidbarer Energie in der k_z-abhängigen Band Dispersion entdeckt. Eines liegt, wie von der *GdW* Rechnung als Teil der direkten Bandlücke vorhergesagt, am Z Punkt, während das andere sich an einem nicht hochsymmetrischen Punkt entlang $\overline{\Gamma}$-$\overline{M}_1$ befindet. Ein Leitungsbandminimum an $\overline{\Gamma}$ wurde bei einer Energie von 1.33 eV oberhalb der Valenzband Maxima identifiziert. Messungen der besetzten und unbesetzten Zustandsdichte weisen auf eine fundamentale Bandlücke mit einer geringeren Energie als 1.33 eV hin. Die anisotropen Eigenschaften von $ReSe_2$ zeigen sich auch in der elektronischen Struktur. Eine vollständig anisotrope E gegen $\mathbf{k}_{||}$ Dispersion der Valenzbänder wird beobachtet. Dabei ist die Bandbreite des obersten Valenzbandes in $\overline{\Gamma}$-$\overline{M}_1$ Richtung deutlich schmaler als in jeder anderen Richtung des $\mathbf{k}$-Raumes. $\overline{\Gamma}$-$\overline{M}_1$ entspricht der Richtung senkrecht zu den Zick-Zack Ketten aus Re-Atomen („diamond chains“). Spinaufgelöste Messungen

zeigen eine bemerkenswert hohe Spinpolarisation der Photoelektronen von bis zu 50% ohne Abzug des Untergrundes. Dies kann teilweise mit einem Oberflächenzustand erklärt werden. Der Großteil der beobachteten Spinpolarisation ist aber auf den Photoemissionsprozess zurückzuführen.

Eine Einzellage von WS_2 ist ein nicht zentrosymmetrischer, direkter Halbleiter. Dieser wurde auf einem Au(111)-Substrat untersucht. Die fundamentale Energielücke ist zu (1.98 ± 0.04) eV bestimmt worden und wird beeinflusst von der dielektrischen Abschirmung des Au-Substrates. Die optoelektronischen Eigenschaften resultieren aus dem Valenzbandmaximum und Leitungsbandminimum in der Ecke der Brillouin-Zone. Rechnungen und Vergleichsmessungen mit volumenartigem WS_2 deuten auf keinen signifikanten Einfluss des Au-Substrates auf das niedrigste Leitungsband und höchste Valenzband nahe $\overline{\mathrm{K}}$ hin. Das Valenzbandmaximum bei $\overline{\mathrm{K}}$ ist vollständig senkrecht zur Oberfläche spinpolarisiert. Der $\overline{\mathrm{K}}'$-Punkt weißt dieselbe Spinstruktur mit entgegengesetztem Vorzeichen auf. Dieser Vorzeichenwechsel der Spinpolarisation wird auch für die Leitungsbänder beobachtet. Das Valenzbandmaximum ist spinaufgespalten mit einem Energieunterschied von (417 ± 23) meV. Für das Leitungsbandminimum wurde (16 ± 7) meV gemessen. Die Reihenfolge der spinaufgespaltenen Bänder ist oberhalb und unterhalb der Fermi-Energie identisch. Das Valenzbandmaximum ist somit entgegengesetzt senkrecht zur Oberfläche spinpolarisiert wie das Leitungsbandminimum. Als Konsequenz ist der energetisch niedrigste optische Übergang spinverboten und daher optisch dunkel. Der erste optisch helle Übergang ist mit dem zweiten Leitungband möglich und benötigt folglich eine um 16 meV höherer Energie als die fundamentale Bandlücke. Die hier bestimmte Spinstruktur der K-„Valleys“ erklärt das Zustandekommen von spinverbotenen „dunklen“ Exzitonen, die in optische Experimenten diskutiert werden.

Contents

List of Figures

Acronyms

ARPES	angle-resolved photoemission
AES	Auger electron spectroscopy
BL	beamline
BiL	bilayer
BZ	Brillouin zone
CB	conduction band
CBM	conduction-band minimum
CFSPE	constant final-state photoemission
DFT	density functional theory
DOS	density of states
EDC	energy distribution curve
FWHM	full width at half maximum

HiSOR	Hiroshima synchrotron radiation center
HVB	highest valence band
IPE	inverse photoemission
LCB	lowest conduction band
LDA	local density approximation
LEED	low-energy electron diffraction
MD	mirror domain
MFDE	momentum-forbidden dark excitons
SARPES	spin- and angle-resolved photoemission
SBZ	surface Brillouin zone
SFDE	spin-forbidden dark excitons
SIS	space inversion symmetry
SL	single-layer
SPLEED	spin polarized low-energy electron diffraction
SOC	spin-orbit coupling

SRIPE	spin- and angle-resolved inverse photoemission
SS	surface state(s)
STM	scanning tunneling microscopy
STS	scanning tunneling spectroscopy
TCS	target current spectroscopy
TMDC	transition metal dichalcogenide
TRIM	time-reversal invariant momenta
TRS	time-reversal symmetry
UHV	ultra-high-vacuum
VB	valence band
VBM	valence-band maximum
VLEED	very-low-energy electron diffraction
XPD	X-ray photoelectron diffraction
XPS	X-ray photoelectron spectroscopy

1

Introduction

The rise of mankind could not have happened without the ability to create tools out of suitable materials. Whole epochs of human history have been termed as materials, such as the stone, bronze or iron age. Throughout history, scientific research led to the discovery and development of an increasing amount of materials with customized properties for tools and other applications. Nowadays, in a historic period that is often described as the information age, the most important tools are electronic devices. In recent years, these devices are required to have an increasing performance while being down-scaled in size at the same time. As a consequence, suitable materials to build devices have also to be down-scaled, down to the very limit of single atomic layers. Studying the unique properties of these two-dimensional materials is not only pivotal to integrate them in possible applications but also fascinating from a fundamental research point of view. Novoselov's and Geim's (Novoselov *et al.*, 2004, 2005) discovery of extracting graphene via micromechanical exfoliation of graphite provided a simple way to prepare a two-dimensional single-layer (SL) of a layered material. As a result, a huge interest in layered materials arose. For instance, the European Union funds the "Graphene Flagship", a research initiative focused on graphene and other two-dimensional materials, with one billion euro.

Graphene has many exciting properties, such as extreme mechanic strength, high electric conductivity and high optical absorption. However, it's zero electronic band gap is a major disadvantage for modern information technology and opto-

electronics. In contrast, many members of the Transition Metal Dichalcogenide (TMDC) family are semiconducting and individual layers can be separated similar as in the case of graphene. Depending on the crystal structure and symmetry, the different TMDCs exhibit a variety of electronic properties. Low symmetric TMDCs result in especially complex and fascinating properties. Having inversion symmetry only, the anisotropic optoelectronic properties of $ReSe_2$ led this material into the focus of research. The underlying complex anisotropic electronic structure is experimentally investigated in the present thesis.

Beside the charge of the electron, it's spin degree of freedom is also utilized in modern information technology, e.g. in magnetic storage in hard drives. Spin effects are not restricted to magnetism. Spin-orbit coupling (SOC) can lead to a spin-dependent electronic structure that may be utilized in novel "spintronic" devices, such as a spin transistor (Datta and Das, 1990). Due to their specific crystal symmetry, semiconducting SL W- and Mo-based TMDCs have pronounced SOC-related spin effects that can potentially be utilized in future spintronic devices. Moreover, SL W- and Mo-based TMDCs have a spin-dependent highest valence band (HVB) and lowest conduction band (LCB) that are decisive for optical transitions. Therefore, the knowledge of this spin dependence is fundamental for designing optoelectronic devices made out of these TMDCs. The spin-dependent properties of HVB and LCB are also of fundamental research interest for the physics of excitons, i.e. bound electron-hole pairs, in TMDCs. Momentum-resolved studies of the valence bands (VBs) of SL W- and Mo-based TMDCs have been conducted (Zhang *et al.*, 2014b; Dendzik *et al.*, 2015; Miwa *et al.*, 2015; Grubisic Cabo *et al.*, 2015; Le *et al.*, 2015; Zhang *et al.*, 2016; Bruix *et al.*, 2016), yet without spin resolution on samples with uniform crystal orientation. In the case of the conduction bands (CBs), no momentum- or spin-resolved studies of the electronic structure have been reported. Thus, momentum- and spin-resolved experimental studies of the spin-dependent electronic structure, particularly the CBs, are desired.

The present thesis provides such experimental information of two important members of semiconducting TMDCs, with the focus on the properties of their band gaps. (i) Angle-resolved photoemission (ARPES) and angle-resolved in-

verse photoemission (IPE) are complementarily used to study the anisotropic VBs and CBs of layered low symmetric $ReSe_2$. The combined use of ARPES and IPE provides information about the type and the size of the band gap. (ii) Spin-resolved ARPES (SARPES) and IPE (SRIPE) allow to quantify the spin-dependent properties of the direct band gap of SL WS_2, particularly the spin texture and the spin-dependent energy splitting of the CBs.

The outline of the present thesis is as follows: chapter 2 introduces SOC-mediated spin effects as well as other electronic and optoelectronic properties of TMDCs. The experimental approach and details of the analysis are described in chapter 3. Chapter 4 focuses on the anisotropic electronic structure of layered $ReSe_2$. After a brief introduction to the basic crystal and electronic properties (Sec. 4.1), the crystal structure and the chemical composition of the sample is characterized in section 4.2. The unexpectedly pronounced spin effects in inversion-symmetric $ReSe_2$ are discussed in section 4.3. ARPES (Sec. 4.4) and IPE experiments (Sec. 4.5) study the HVB and LCB, respectively. Combining these results enable to deduce information about the size and the type of the band gap of $ReSe_2$. In section 4.6, a distinct direction in the anisotropic electronic structure is identified. Chapter 5 presents the results about SL WS_2 with the focus on the CBs. The characterization of the SL WS_2/Au(111) sample (Sec. 5.1.1) shows that it fulfills the structural and chemical requirements for further experiments. For comparison, in section 5.1.2, the properties of a bulk WS_2 sample are characterized. In section 5.2.1, the $E(\mathbf{k}_{||})$ dispersion of CBs in SL WS_2 on a Au(111) substrate is determined. A comparative IPE experiment with a bulk WS_2 sample (Sec. 5.2.2) indicates negligible influence of the Au(111) substrate on the CB minimum (CBM). Therefore, the experimentally quantified spin-dependent properties of CBM and VB maximum (VBM) of SL WS_2/Au(111) (Sec. 5.2.3) reflect the properties of a freestanding SL WS_2.

2

Spin-Dependent Band Structure of Transition Metal Dichalcogenides

The spin degree of freedom of electrons in crystalline solids is important and not only related to the magnetic properties. Even in the absence of a magnetic field, there are cases when the spin degeneracy is lifted. SOC is the driving force behind these spin effects. In the material class of TMDCs spin effects are of particular importance, especially in the semiconducting SL of tungsten- and molybdenum-based TMDCs. Other TMDC compounds have a spin-degenerate electronic structure. Nonetheless, particular optoelectronic properties, e.g. of anisotropic rhenium-based TMDCs, are interesting with respect to possible applications.

The goal of this chapter is to introduce SOC-mediated spin effects as well as other electronic and optoelectronic properties of TMDCs. In section 2.1 the origin of spin effects in the band structure of nonmagnetic solids is discussed. Special attention is given to symmetries which fundamentally determine if and what kind of spin-polarized states can exist within the solid. Section 2.2 introduces the different crystal structures and symmetries of TMDCs. Thickness-dependent properties (Sec. 2.3) and the occurrence of excitons (Sec. 2.4) will be discussed particularly. Finally, spin and valley physics of TMDCs and its deep connection with the spin-dependent band structure will be introduced in section 2.5.

2.1 Origin of Spin Effects in the Band Structure of Nonmagnetic Solids

Spin effects are often associated with ferromagnetic materials. However, these effects play a crucial role in nonmagnetic systems as well. The origins of the spin effects in nonmagnetic materials will be explained in this section. As a first step, the influence of the spin on the energy of electrons in nonmagnetic crystalline solids is described. Electrons move within the periodic lattice potential $V(\mathbf{r})$ and their behavior determines the fundamental properties of crystalline solids. Therefore, the properties of electrons within crystalline solids are studied experimentally and theoretically. The motion of such electrons can be described by a nonrelativistic one-electron Hamiltonian H_{nr} as

$$H_{\mathrm{nr}} = \frac{\hat{p}^2}{2m^*} + V(\mathbf{r}) = -\frac{\hbar^2}{2m^*}\nabla^2 + V(\mathbf{r}) \tag{2.1}$$

with the momentum operator $\hat{p}$, the reduced Planck constant $\hbar$, the nabla operator ∇ and the effective electron mass m^*. Solutions of this Schrödinger equation are electronic states that can be described by lattice periodic Bloch states $\Psi_n(\mathbf{r})$ with eigenvalues (energies) $\mathrm{E}_n(\mathbf{k})$. Both depend on the quantum number n. H_{nr} depends on the wave vector of the electron $\mathbf{k} = \mathbf{p}/\hbar$, but does not describe any dependence on the spin degree of freedom of electrons.

Based on a nonrelativistic approximation[1] of the Dirac equation, Wolfgang Pauli extended H_{nr} with relativistic correction terms (Winkler, 2003). Two of them depend on the electron spin. (i) The Zeeman term that describes the coupling of the electron's magnetic moment $\boldsymbol{\mu}$ due to its spin $\mathbf{S}$ to an external magnetic field. (ii) The spin-orbit coupling (SOC) term, which can be understood in the following way by considering an atom with a nucleus and an electron: the electron has an orbital angular momentum $\mathbf{L}$. Therefore, in its rest frame the nucleus is a moving charge and creates a magnetic field $\mathbf{B}$ that depends on $\mathbf{L}$. The electron's magnetic moment $\boldsymbol{\mu}$ then couples to $\mathbf{B}$, i.e., the electron spin $\mathbf{S}$ is coupling to the orbital

[1] Neglecting relativistic effects on electrons, i.e. for slow electrons.

momentum **L**. In a crystalline solid, the SOC term can be written as:

$$H_{\mathrm{SOC}} = -\frac{\hbar}{2m^{*2}c^2}(\nabla V \times \mathbf{k}) \cdot \mathbf{S} \tag{2.2}$$

with c being the velocity of the light. Including H_{SOC}, the Bloch solutions $\Psi_{n,m_s}(\mathbf{r})$ now also depend on the spin quantum number m_s.

H_{SOC} itself depends on the gradient of the potential V(**r**). The gradient can exist due to the asymmetric potential at the surface and due to the slope of the atomic core potential. The former depends on the asymmetric charge distribution along one or more axes at the surface. A more asymmetric distribution leads to stronger effects. The axes with asymmetric charge distribution affect the orientation of the spin-polarization vector. An asymmetry along the surface normal leads to a spin splitting that can be qualitatively described by the Rashba-Bychkov model, which is explained later in this section. The magnitude of the atomic part of SOC, λ, can be estimated (Haken and Wolf, 2002) and is proportional to $Z\overline{(1/r^3)}$ with the atomic number Z and the expectation value of the distance $\overline{(1/r^3)}$ between electron and nucleus. For hydrogen-like atoms, r is equal to the Bohr radius $a_0 \propto (1/Z)$ and in this rough approximation it follows

$$\lambda \propto Z^4 \,. \tag{2.3}$$

With (2.3), it becomes evident that SOC-induced effects are mainly observed in heavy elements with a high atomic number Z.

Importantly, SOC alone does not lift the twofold degeneracy of $E_{n,m_s}(\mathbf{k})$ due to the two possible values of m_s, denoted here as + and -. This so-called "Kramers degeneracy" is universal for systems with time-reversal symmetry (TRS) and space inversion symmetry (SIS). TRS results in E(**k**,+) = E(-**k**,-), whereas SIS leads to E(**k**,+) = E(-**k**,+). As a result in systems with both symmetries it follows the twofold degeneracy E(**k**,+) = E(**k**,-). In the absence of an external magnetic field, crystalline solids always fulfill TRS. However, SIS can be broken, leading to the lifting of Kramers degeneracy, for several reasons.

(i) Some crystal structures such as zinc blende and wurtzite are noncentrosymmetric, i.e. they do not have SIS. A prominent example is GaAs, which grows in a zink blende structure. Here, the breaking of Kramers degeneracy leads to a **k**-dependent splitting of E(**k**,+) and E(**k**,-) (Luo *et al.*, 2009). This spin splitting was described by Dresselhaus (1955). Alternatively to the Dresselhaus spin splitting, noncentrosymmetric structures can give rise to the bulk Rashba effect (Zhang *et al.*, 2014a) with similar spin textures as in the case of the normal Rashba-Bychkov-effect that is described below.

(ii) At the crystal surface, the SIS is always broken and, as a consequence, the confinement potential is not symmetric. Additional electronic states at the surface may occur. These states are (quasi-) two-dimensional, i.e. electrons are confined within the surface plane, and can be spin split even if the bulk potential is space inversion symmetric. This was experimentally first shown for the famous Shockley surface state of Au(111) (LaShell *et al.*, 1996; Hoesch *et al.*, 2004; Wissing *et al.*, 2013; Tusche *et al.*, 2015) and later for numerous other surfaces or interfaces (Krasovskii, 2015). For quasi-free electronic states, occurring at the (111) surface of nobel metals, spin splitting effects can be qualitatively described by the "Rashba-Bychkov" model (Bychkov and Rashba, 1984) for a two-dimensional electron gas under the influence of a perpendicular external electric field[2]. Within this model, the energy of quasi-free electrons with spin quantum number + and - is

$$E_{\pm} = E_0 + \frac{\hbar^2 \mathbf{k}_{\parallel}^2}{2m^*} \pm \alpha_R |\mathbf{k}_{\parallel}| \tag{2.4}$$

and is illustrated in figure 2.1. The Rashba parameter α_R represents the strength of the spin splitting and is proportional to the perpendicular potential gradient: $\alpha_R \propto \frac{\mathrm{d}V}{\mathrm{d}z}$. Spin splittings with similar spin textures as in figure 2.1 are often referred to as Rashba effect in the literature. Note that bulk (Bloch) states can also be affected by the surface potential. According to Krasovskii and Chulkov (2011), these states are spin split locally within the surface region, although Kramers degenracy is present in the bulk.

[2]The Rashba-Bychkov model underestimates the strength of the spin splitting in case of surface states by several orders of magnitude (LaShell *et al.*, 1996).

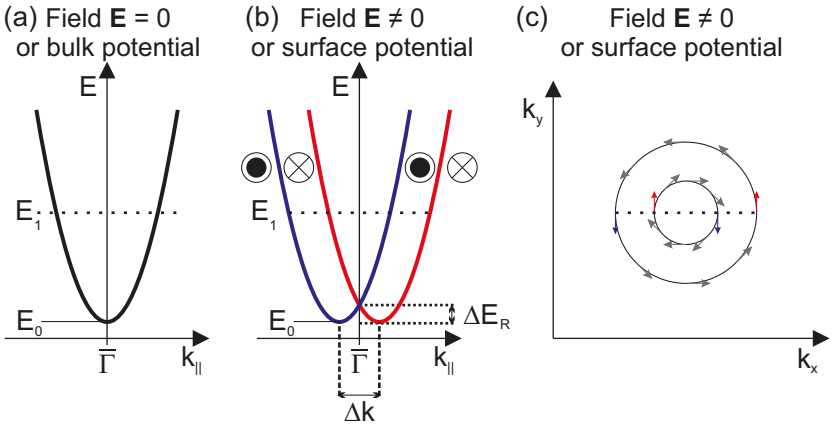

Figure 2.1: Illustration of the Rashba-Bychkov effect. In a two-dimensional free electron gas the electrons have a parabolic dispersion with a twofold degeneracy (a). Under the influence of an external electric field **E** the degeneracy is lifted and the parabola splits into two parabolas seperated by Δ**k** (b). The difference between the crossing point and the bottom of the parabolas E_0 is measured by the Rashba energy E_R. The spin splitting and spin texture is **k**-dependent. At an energy E_1 above E_0 the parabolas form two circles in **k**-space with opposite and **k**-dependent spin directions (c). The Rashba-Bychkov effect also describes qualitatively the spin splitting and spin texture of surface states at the (111) surfaces of noble metals with asymmetric confinement potentials.

Many surface states show complex spin-textures which cannot be explained in terms of the Rashba-Bychkov model. For example, at the Tl/Ge(111) surface the spin-polarization vector rotates from in-plane to out-of-plane (from parallel to perpendicular to the surface) (Eickholt *et al.*, 2016). To explain complex spin-textures one has to incorporate the symmetry of the surface (Oguchi and Shishidou, 2009) which defines the allowed directions of the spin-polarization vector at given points in **k**-space. To illustrate the effect of the symmetry, three important examples are given. (i) At time-reversal invariant momenta (TRIM) points, the spin is degenerate. The simplest example is the $\overline{\Gamma}$ point, i.e. the center of the surface Brillouin zone (SBZ). (ii) Since the spin behaves like a pseudovector, it follows that at any point in **k**-space within a mirror plane only spin polarization perpendicular to it is nondegenerate. Hence, two orthogonally mirror planes result in vanishing spin polarization. (iii) At any point in **k**-space with C3 surface symmetry (Schoenflies notation) the spin polarization can only be out-of-plane. A good example are the corners ($\overline{\text{K}}$-points) of a hexagonal SBZ.

Importantly, without a magnetic field, SOC-derived spin splittings never give rise to a net spin polarization when considering the whole system. When spin-polarized electronic states with a wave vector **k** are found, the electronic states at -**k** will be oppositely spin polarized. This results in a zero net spin polarization, as demanded by TRS.

In summary, SOC can heavily modify the electronic structure of crystalline solids. Spin-dependent energies can occur when the Kramers degeneracy is broken, which is always the case at surfaces. Obviously, these effects are important in (layered) two-dimensional systems such as TMDCs. Using the basics described above, specific effects of SOC on TMDCs will be discussed in section 2.5.

2.2 Crystal Structure and Symmetry of TMDCs

TMDCs have been studied extensively in the 1950s and 1960s. Many structural, electrical and optoelectronical properties already have been known by that time (Wilson and Yoffe, 1969). TMDCs consist of a transition metal M sandwiched between two layers of chalcogen atoms X (with X= S, Se or Te) leading to a 1:2 stoichiometry. There is strong bonding within this X-M-X trilayer, while in between the trilayers only weak van-der-Waals bonding exists. Conventionally, a X-M-X trilayer, even though not strictly being a single atomic layer, is called a single-layer (SL) from now on.

There are 39 stable compositions of TMDCs (Bernadi *et al.*, 2017) which can grow in one or several structures. All these structures originate from either the octahedral T-phase or the trigonal prismatic H-phase. Various stacking polytypes result in eleven different structures of TMDCs (Katzke *et al.*, 2004).

The most common structures, the 2H and 1T structures are shown in figure 2.2. The number in the nomenclatures refers to the amount of layers forming the unit cell, whereas H and T refers to the originating primary phase. Note that due to different stacking two 2H polytypes for TMDCs with 1:2 stoichiometry exist, defined as $2H_a$ and $2H_c$. $2H_a$ is found at metallic TMDCs such as NbS_2 and TaS_2, whereas $2H_c$ is the structure of many semiconducting compounds such as MoS_2 and WS_2 (Han *et al.*, 2018). The two 2H polytypes have different positions of the

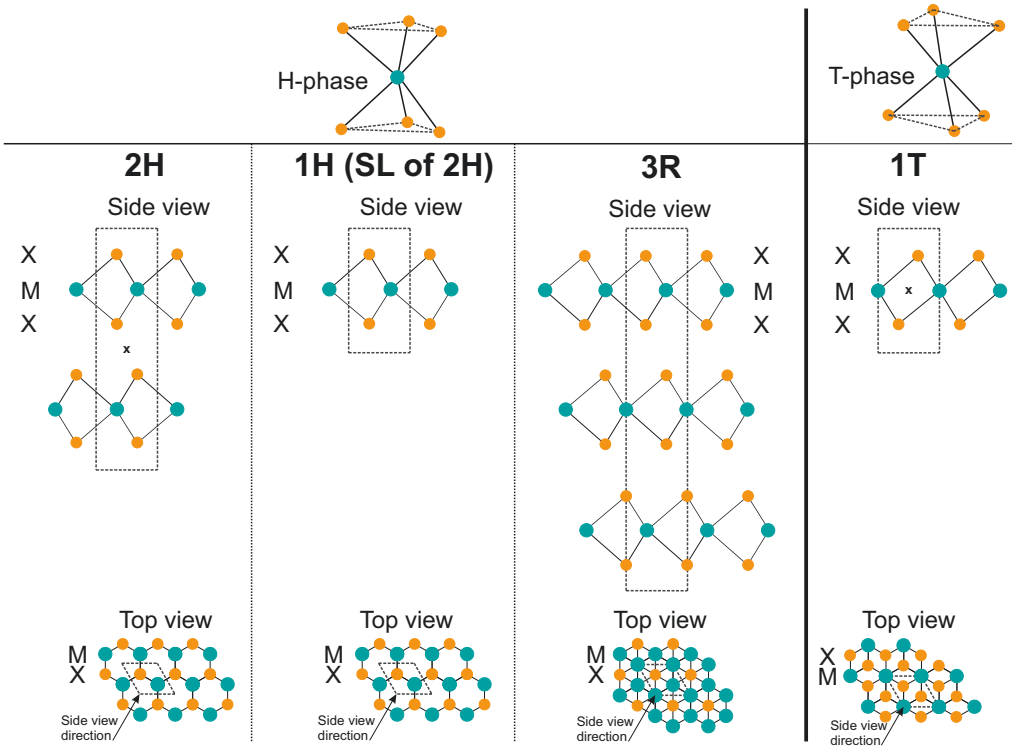

Figure 2.2: Illustration of polytypes of the trigonal prismatic H-phase and the octahedral T-phase, both consisting of two tetrahedrons. The T-phase is constructed by rotating one tetrahedron 180° with respect to the other one. Top and side view of the structures. Blue and orange dots symbolize metal and chalcogen atoms, respectively. Note that in the top view only the respective uppermost visible atom is shown. The dashed boxes indicate the primitive unit cells with (if present) the inversion center noted by a small x. The 2H and 1T structures are centrosymmetric, while the 1H and 3R structures lack space inversion symmetry.

M and X atoms within the unit cell (see (Katzke *et al.*, 2004)). Nonetheless, both polytypes exhibit the same $P6_3/mmc$ symmetry and are usually not distinguished in the literature. Accordingly, the structure of WS_2 in chapter 5 will be simply called 2H. Importantly, all 2H polytypes have an inversion center in between the layers. However, the SL of a 2H polytype, referred to as 1H, consequently lacks this inversion center. As a result the spin-degeneracy is lifted in 1H.

Note that another polytype originating from the H phase exists that is called 3R (see Fig. 2.2). The R is referring to the rhombohedral symmetry of the 3R structure. Just like 1H, the 3R polytype also lacks an inversion center.

The T-phase has only one layer per unit cell leading to only one polytype called 1T. However, some compounds such as ReS_2 and $ReSe_2$ grow in a distorted 1T

structure (see Fig. 4.1 in chapter 4). This so-called 1T′ structure has a triclinic $P\bar{1}$ symmetry, i.e. only inversion symmetry, and therefore gives rise to highly anisotropic properties.

2.3 Thickness Dependent Properties of TMDCs

It is easy to create a stable SL, bilayer, trilayer or multilayer out of a layered TMDC by micromechanical exfoliation. Therefore, this class of materials is a playground to study and utilize phenomena caused by reduced thickness. Thin films can have unique properties deviating from the respective bulk material. For example, quantum well states that occur due to the perpendicular confinement of electrons in thin films have been extensively studied (Chiang, T.C., 2000). Layered materials such as TMDCs have only weak coupling in between the SL. Nonetheless reducing the thickness and ultimately the dimensionality of bulk TMDCs leads to pronounced effects in these materials too.

In fact, tungsten- and molybdenum-based TMDCs are famous for their thickness-dependent properties. In 2010, Mak *et al.* (2010) found that SL MoS_2 has a strong photoluminescence, much stronger than the respective bulk material. They concluded that 1H SL MoS_2 is a direct semiconductor, whereas multilayer and bulk MoS_2 are indirect semiconductors. The effect is caused by different orbital contributions of the electronic states at $\overline{\Gamma}$ and $\overline{K}$. The interlayer interaction, present in multilayer and bulk samples, strongly shifts the VBM at $\overline{\Gamma}$ to higher energies, whereas $\overline{K}$ is mostly unaffected (Ramasubramaniam *et al.*, 2011). In the CBs the position of the CBM shifts from Q (halfway $\overline{\Gamma}$-$\overline{K}$) to $\overline{K}$, when reducing the thickness to a SL. As a result, a thickness-dependent direct-indirect crossover of the band gap is generally observed in tungsten and molybdenum based TMDCs (Roldán and Guinea, 2017).

When reducing the thickness of the material, other interactions than the interlayer interaction become important. At small thicknesses the material is more and more influenced by properties of the environment. Even if there is no bonding between the environment and the few-layer material, the dielectric function of the environment ϵ_{Env} may be different to the one of the bulk material ϵ_{Bulk}. If ϵ_{Env}

is lower than ϵ_{Bulk}, for instance in the case of a freestanding thin semiconducting layer, the Coulomb interaction created by electrons or holes is less screened. As a consequence, the contribution of the self-energy, that is in a simplified picture related to the interaction between charges (Wang *et al.*, 2018), to the absolute energy of electrons and holes is increased. Accordingly, the energy to create an unbound electron-hole pair is increased, i.e. the quasiparticle band gap E_{gap} is increased. The effect is well established and was utilized to engineer band gaps in TMDCs by making use of the dielectric environment (Raja *et al.*, 2017; LaMountain *et al.*, 2018).

2.4 Excitons in TMDCs

The Coulomb interaction gives rise to another phenomenon in thin semiconducting films that is particularly interesting in the case of TMDCs. When an electron is excited to the CB, a hole is created in VB. Due to the attractive Coulomb force between hole and electron they can form a bound electron-hole pair, a so-called neutral exciton. In this case the positions of electron and hole are correlated (see sketch in Fig. 2.3 (a)). A short summary about excitons in TMDCs and their connection to the spin-dependent band structure is given in the following, while a detailed description is available in the literature (Wang *et al.*, 2018).

In SL TMDCs the exciton's size is on the order of a few nm, smaller than the well known Wannier-Mott excitons (Wang *et al.*, 2018) of semiconductors such as GaAs (Nam *et al.*, 1976). Despite the smaller size, excitons in TMDCs can be quantitatively described in the Wannier-Mott description within the effective mass approximation (Wang *et al.*, 2018). The description results in a hydrogen-like series of exciton states with the quasiparticle band gap energy E_{gap} being equivalent to the continuum energy within a hydrogen atom. The "binding energy" of excitons $E_{\text{exc,b}}$ usually is very small, for instance 4 meV in case of GaAs (Nam *et al.*, 1976). However in SL TMDCs, the exciton binding energy is orders of magnitude higher in the order of electron volts (Ramasubramaniam, 2012; Cheiwchanchamnangij and Lambrecht, 2012). The three main reasons according to (Wang *et al.*, 2018) are: (i) the rather small electron-hole separation in SL TMDCs due to the reduced

dimensionality. (ii) The high effective masses of electrons m_e and holes m_h in the K-Valleys of TMDCs gives rise to a high reduced mass $\mu = m_e m_h/(m_e + m_h)$ which is proportinal to $E_{\mathrm{exc,b}}$ in a hydrogen-like model (Chernikov *et al.*, 2014). (iii) The dielectric environment leads to weak screening (especially in out-of-plane direction) and therefore high Coulomb interaction.

Due to the high exciton binding energies in SL TMDCs the respective optical spectrum is dominated by excitonic effects. A schematic optical spectrum of an ideal SL TMDC with one series of exciton states is sketched in figure 2.3 (c). The band gap seen in optical experiments is $E_{\mathrm{gap,opt}} = E_{\mathrm{gap}} - E_{\mathrm{exc,b}}$. The precise determination of $E_{\mathrm{exc,b}}$ requires the knowledge of $E_{\mathrm{gap,opt}}$ by optical experiments as well as the determination of E_{gap}. The latter is not trivial. It can be indirectly approximated using optical methods with help of model calculations and further assumptions (Chernikov *et al.*, 2014; He *et al.*, 2014). A direct way of determining E_{gap} is possible by means of a combination of direct and inverse photoemission as used in this thesis or by scanning tunneling spectroscopy (Ugeda *et al.*, 2014; Bruix *et al.*, 2016; Rigosi *et al.*, 2016). The determination of E_{gap} with STS is particularly difficult due to tip induced band bending and the fact that predominantly electronic states with zero parallel momentum contribute to the tunneling current in STS (Tersoff and Hamann, 1983, 1985; Zhang *et al.*, 2015; Murray *et al.*, 2019). Thus, the combination of direct and inverse photoemission is the most promising way to precisely determine E_{gap} and hence, together with optical experiments, $E_{\mathrm{exc,b}}$.

The optical properties of TMDCs and the physics of excitons are deeply connected with the spin-dependent band structure as discussed in the subsequent section.

2.5 Spin and Valley Physics in TMDCs

The present section will describe SOC-related effects within the electronic structure specifically in TMDCs. Therefore, it is useful to distinguish between inversion symmetric and inversion asymmetric TMDCs.

Common structures of bulk TMDCs are always inversion symmetric with the exception of the 3R structure, where spin polarization has been observed (Suzuki *et al.*, 2014). 1T and 1T′ structures preserve SIS independent of the number of layers. Note that at the surface of bulk systems, despite Kramers degeneracy, spin-dependent effects in the band structure are still possible (see Sec. 2.1).

Recently, an interesting feature of inversion symmetric 2H bulk TMDCs was discovered. In the 2H structure the unit cell consists of two layers that are rotated 180 degree to each other, ensuring SIS (see Fig. 2.2). However, locally, within a SL, inversion symmetry is broken. Since SOC is mainly anchored at the individual nuclear sites, the symmetry of individual atom sites matters and can lead to so-called ”hidden spin polarization” in centrosymmetric bulk materials in general (Zhang *et al.*, 2014a). States localized within a single layer of the 2H structure can be spin polarized, while global space inversion symmetry is retained due to the other oppositely spin-polarized layer, i.e. opposite spins are spatially separated. This spin polarization can be detected by photoemission techniques due to the finite escape depth or selective excitations of electrons. The effect is referred to as ”spin-layer locking” and has been observed with spin- and angle-resolved photoemission in bulk WSe_2 (Riley *et al.*, 2014) and MoS_2 (Razzoli *et al.*, 2017).

In addition to the effects described above, more spin polarization effects can be expected in inversion asymmetric systems. Beside the 3R structure, importantly the 1H structure (SL of the 2H structure) lacks inversion symmetry. The same is true for any odd number of layers in a few-layer system with H structure that can not be considered as bulk material. Prominent examples are the tungsten- and molybdenum-based TMDCs. As mentioned before, in these systems the properties of SL are of particular importance. The spin-related effects will be discussed here by means of the example of SL WS_2.

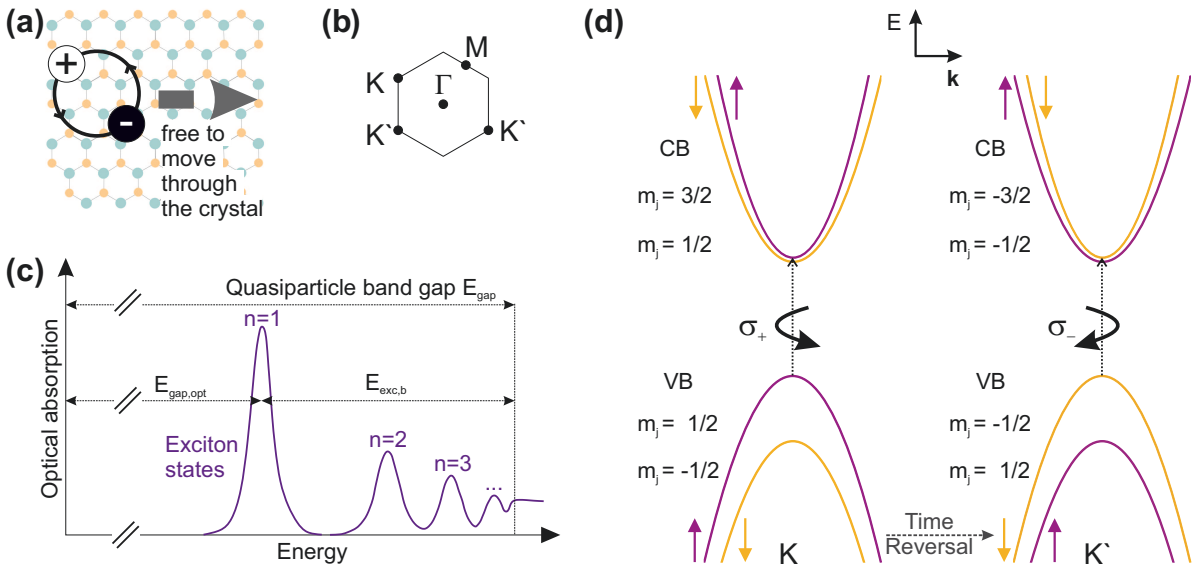

Figure 2.3: (a) Schematic real-space representation, adapted from Wang *et al.* (2018), of a Wannier-Mott exciton indicating the spatial correlation of electron and hole. The grey arrow indicates the center of mass motion of the whole exciton. (b) The 1H SL TMDC BZ with the distinguishable K and K′ points. (c) Schematic optical absorption spectra of an ideal SL TMDC with one series of excitonic states. The sketch is used to illustrate the connection of exciton binding energy $E_{\mathrm{exc,b}}$ with the optical and quasiparticle band gap ($E_{\mathrm{gap,opt}}$ and E_{gap}). Adapted from Wang *et al.* (2018). (d) Illustration of the coupled spin and valley physics in tungsten-based 1H SL TMDCs. The upper two VB and lower two CB are sketched around the K and K′ valleys. The respective secondary total angular momentum quantum number m_j resulting from the predominant orbital character of the bands is given according to Mak *et al.* (2012). The K (K′) valley can be selectively populated by using σ_+ (σ_-) light that induces the transition of the highest VB to the second lowest CB at K (K′).

The fundamental band gap in SL WS_2 is located in the corner of the Brillouin zone (BZ) at the K high symmetry point, where spin polarization is possible. This is in contrast to other semiconductors such as GaAs, where the fundamental band gap is at a TRIM point (the Γ point) and consequently the spin is degenerate. The spin-dependent band gap of SL WS_2 is an important feature specifying possible optical transitions. It also gives rise to the so-called ”valley physics” (Xiao *et al.*, 2012) as discussed in the following.

A schematic band structure of the upper VBs and lower CBs around the K and K′ high-symmetry points is sketched in figure 2.3 (d). The related BZ is shown in (b). Note that in the case of the 1H structure the BZ is two-dimensional and therefore

identical to the SBZ. Consequently, the usage of bars to indicate symmetry points of the SBZ is optional. The band structure around K and K′ points is often referred to as "K and K′ valleys". The two sublattices, occupied with a transition metal M and two chalcogens X, respectively, result in a BZ with threefold symmetry and distinguishable K and K′ points. K and K′ feature the same E vs **k** dispersion yet with opposite direction of out-of-plane spin polarization. Therefore, looking at the HVB one can say the spin is locked to a valley, i.e. to K or K′.

The concept of "valleytronics" (Yu and Yao, 2017) makes use of the two nonequivalent valleys. Similar to the electron's spin index, i.e. "+" or "-", a valley index of $\tau = \pm 1$ is given for the K and K′ valley. The idea is to use this valley index as an information carrier in the same way as the spin is used in spintronic applications. The idea became popular with the emergence of graphene with its two nonequivalent but spin-degenerate K valleys (Xiao *et al.*, 2007). To utilize the valley index for applications, valleys have to be selectively occupied, i.e valley polarization has to be achieved.

The broken inversion symmetry in 1H SL TMDCs allows to distinguish between K and K′ by using circularly polarized light. The optical selection rules for right circularly polarized (σ_+) and left circulary polarized (σ_-) light require the secondary total angular momentum quantum number m_j to be changed by +1 and -1, respectively. The spin quantum number m_s remains unchanged in the transition, i.e. no spin flip is allowed.

Consider the HVB at K in figure 2.3 (d). Due to the absence of inversion symmetry, the spin degeneracy of the highest VB is lifted by SOC and it has $m_j = 1/2$. The second VB (with $m_j = -1/2$) is well separated in energy and can be neglected, when exciting the VBM resonantly with light. On the other hand, the two CBs ($m_j = 1/2$ and $m_j = 3/2$) are separated by just a few meV (compare Ch. 5) and can be accessed with similar energies. Consequently, using σ_+ light, which results in $\Delta m_j = 1$, a transition between the HVB and the second LCB is possible. With σ_- light, which requires $\Delta m_j = -1$, no optical transition is possible. Due to time-reversal symmetry, the situation is opposite at the K′ valley. Here, the HVB has $m_j = -1/2$ and CBs have $m_j = -1/2$ and $m_j = -3/2$. Therefore, using σ_- light the transition between the HVB and second LCB is possible, whereas σ_+ can not excite electrons in the K′ valley. As a result, the K and K′ valley can

be selectively excited with circular polarized light, i.e. valley polarization can be achieved. Experimentally this was first shown for MoS_2 (Mak *et al.*, 2012; Zeng *et al.*, 2012). Note that this way of achieving valley polarization would not work if the HVB is spin degenerate. Since spin orientations can be assigned to the nonequivalent valleys, the physics of systems such as SL WS_2 can be described as coupled spin and valley physics (Xiao *et al.*, 2012).

The interplay of the spin of HVB and LCB and dipole selection rules not only predefine fundamental optical direct transitions, it also influences the luminescence of the material. If an exciton is created via resonant photon absorption, it is optically bright, i.e. it can decay radiatively. However, the exciton can scatter with electrons, phonons, defects or other excitons resulting in a spin flip or change of momentum (Wang *et al.*, 2018). This way an exciton may be modified in a way that radiative recombination is no longer possible. A change of momentum results in two different types of momentum-forbidden dark excitons (MFDE). The inter-valley exciton consists of an electron in the K valley while the hole is in the K′ valley. In addition, the so-called intra-valley MFDE can exist with the hole at the K point and the electron in the other local minimum along Γ-K, known as the Q point.

Spin-forbidden dark excitons (SFDE) are closely related to the spin-dependent CBs. Consider an exciton with the electron and the hole both sitting in $m_j = m_s = 1/2$ states , as it is the case for the LCB and HVB at K in figure 2.3. The radiative recombination is spin forbidden in this case. Therefore the creation of SFDE reduces the luminescence and affects possible applications (Echeverry *et al.*, 2016) such as excitonic lasers (Ye *et al.*, 2015). The amount and rate of SFDE depends on the underlying spin-dependent CB structure. For a better understanding of the SFDE and related optical and electronic phenomena, the exact knowledge of the energy splitting and spin polarization of the CBs at K and K′ is pivotal. In the case of SL WS_2 this knowledge is obtained by conducting combined spin-resolved direct and inverse photoemission experiments, as presented in chapter 5.

3

Methods

Understanding the electronic and optoelectronic phenomena of semiconducting TMDCs introduced in the preceding chapter requires a profound knowledge of the underlying electronic structure. Most prominently, this includes the HVB and LCB. The standard technique to study the occupied electronic structure, i.e. VBs, with momentum resolution is angle-resolved photoemission (ARPES). If necessary, spin resolution can be added (SARPES). Naturally, ARPES has no access to the unoccupied electronic states, i.e. CBs. To get this information, one has to rely on either pump-probe techniques, e.g. two-photon photoemission, or make use of the time- reversed process, i.e. Inverse Photoemission. Angle-resolved Inverse Photoemission (IPE) enables momentum-resolved studies of the CBs, optionally with spin resolution (SRIPE).

Combined SARPES and SRIPE experiments provide comprehensive information about spin and energy of the HVB and LCB and the electronic band gap which is confined by them. Because of their surface sensitivity, SARPES and SRIPE are especially suitable for, but not limited to, studies of two-dimensional layered materials. A detailed description of (S)ARPES and (SR)IPE can be found in the literature (Pendry, 1981; Dose, 1985; Smith, 1988; Himpsel, 1990; Donath, 1994; Hüfner, 2003; Damascelli, 2004; Donath, 2018).

In the following section 3.1, the basic concepts of (S)ARPES and (SR)IPE and the respective relevant aspects for this thesis will be briefly described. Details on how to obtain information about the perpendicular momentum k_z and the spin

polarization are given in section 3.1.1 and section 3.1.2, respectively. Subsequently, in section 3.2, details of the experimental setups at the University of Münster and at the Hiroshima Synchrotron Radiation Center (HiSOR) are described.

3.1 Spin- and Angle-Resolved (Inverse) Photoemission

The photoelectric effect was discovered by Hertz (1887) and described by Einstein (1905) and is the basic principle of ARPES. The process is sketched in figure 3.1 (a). An incoming photon with energy $h\nu$ excites an electron of an occupied initial state $|i\rangle$ to a final state $|f\rangle$ above the vacuum energy E_V. Eventually this electron is then emitted from the crystal. The analogous principle of IPE is sketched in figure 3.1 (b). An incoming electron makes a transition into an unoccupied final state $|f\rangle$ of the sample, thereby emitting a photon. Therefore, IPE provides information about the unoccupied electronic structure above and below E_V.

The probability of the transition in ARPES and IPE can be described within the dipole approximation via a transition matrix element $\langle f|\mathbf{A}\cdot\mathbf{p}|i\rangle$, in which $\mathbf{A}$ is the vector potential of the light and $\mathbf{p}$ is the momentum operator. As a consequence, the symmetry of $|i\rangle$ and $|f\rangle$ as well as the light polarization and geometry of the experiment are decisive for the amount of photoelectrons (photons) detected in ARPES (IPE). This can be utilized to obtain information about the symmetry of electronic states probed in photoemission techniques (Eberhardt and Himpsel, 1980).

The initial- and final-state energies (E_i and E_f) are referenced to the Fermi energy E_F, whereas the kinetic energy E_{kin} is referenced to the vacuum energy E_V. The latter differs from E_F by the work function Φ. From energy conservation follows

$$h\nu = E_f - E_i = E_{kin} + \Phi - E_i \tag{3.1}$$

for ARPES and

$$h\nu = E_i - E_f = E_{kin} + \Phi - E_f \tag{3.2}$$

in the case of IPE. In ARPES, measuring the energy $h\nu$ of the incident photons and E_{kin} of the emitted electrons allows to deduce the energy E_i of the occupied

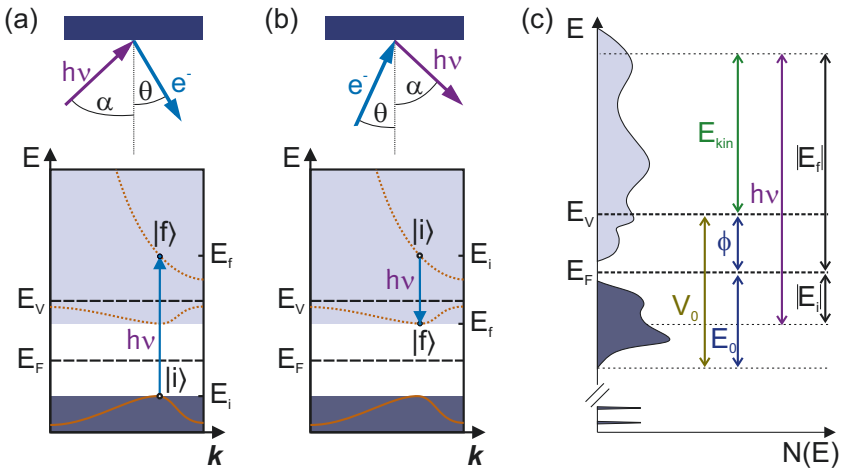

Figure 3.1: Illustration of the principle of ARPES (a) and IPE (b) in a semiconductor. In APRES, an electron populating an occupied initial state $|\mathrm{i}\rangle$ is excited by the incoming photon to a final state $|\mathrm{f}\rangle$ above $\mathrm{E_V}$ and eventually emitted from the sample. In IPE an incident electron at the angle θ couples to the initial state $|\mathrm{i}\rangle$ above the vacuum energy $\mathrm{E_V}$. In the following, a radiative transition into an unoccupied final state $|\mathrm{f}\rangle$ can occur. Thereby a photon is emitted at the angle α with the energy $\mathrm{h}\nu$. In (c), an exemplary ARPES transition is sketched in order to illustrate the definition of the relevant quantities used in sections 3.1 and 3.1.1.

initial state. Equally in IPE, measuring E_{kin} of the incident electrons and $h\nu$ of the emitted photons allows to deduce the energy E_{f} of the unoccupied final state.

The photon momentum for energies used in typical ARPES experiments, including energies used in this thesis ($h\nu \leq 150$ eV), is much smaller than the typical BZ size of a solid. Therefore, the transition between initial state $|\mathrm{i}\rangle$ and final state $|\mathrm{f}\rangle$ is vertical within the reduced-zone scheme[1], i.e. $\mathbf{k}_{\mathrm{f}} - \mathbf{k}_{\mathrm{i}} = 0$.

Upon leaving or entering the crystal, k_z is influenced by the surface potential of the crystal, while the momentum parallel to the surface $\mathbf{k}_{||}$ is conserved. Thus, the value of $k_{||}$ of the probed initial and final states in ARPES and IPE, respectively, can be deduced from the momentum of the electron (with the mass m_e) in vacuum k_{vac} and the emission (incidence) angle θ as follows:

$$k_{||} = k_{vac} \sin\theta = \sqrt{\frac{2m_e}{\hbar^2}} \sqrt{E_{\mathrm{kin}}} \sin\theta. \tag{3.3}$$

[1]For the momentum conservation within the extended-zone scheme it follows $\mathbf{k}_{\mathrm{f}} - \mathbf{k}_{\mathrm{i}} = \mathbf{G}$. In this depiction it can be seen that a reciprocal lattice vector $\mathbf{G}$ is involved in momentum conservation. Indeed, the electron needs additional momentum to reach the excited state (Mahan, 1970) which is provided by the crystal in form of $\mathbf{G}$.

By using equation 3.3, the electronic dispersion E($\mathbf{k}_{\parallel}$) can be determined. For two-dimensional electronic states, e.g. surface or interface states, E($\mathbf{k}_{\parallel}$) contains the full information, since k_z is not a good quantum number in this case. The same is true for two-dimensional single-layer materials if they can be considered as (quasi-) freestanding. However, in bulk materials, such as single crystals or bulk layered materials with non-vanishing interlayer coupling, electronic states will depend on k_z in general. In the following section, approaches to deduce the E(k_z) information are described.

3.1.1 Obtaining the Perpendicular Momentum k_z

Several complex methods were developed to obtain information about k_z, including a triangulation method (Kane, 1964) and the combined use of very-low-energy electron diffraction and constant final state ARPES (VLEED-CFSPE) (Strocov *et al.*, 1997, 1998, 2001). The triangulation method involves several measurements of the same transition on different sample surfaces of the material and is therefore not suitable for layered materials with one preferred orientation.

VLEED-CFSPE can determine the E($\mathbf{k}_{\parallel}$) on a high symmetry line of the SBZ with k_z fixed at a previously with VLEED determined value (Strocov *et al.*, 2001). It involves changing the photon energy in ARPES for every value of $k_{\parallel}$, in order to use a constant final state and get the E($\mathbf{k}_{\parallel}$) for a single given k_z. Therefore, VLEED-CFSPE is impractical when mapping the band structure for a specific band at an unknown non-high-symmetry point in $\mathbf{k}$-space, for instance the VBM of $ReSe_2$ as described in chapter 4.

An alternative way of determining k_z in ARPES is applied in this thesis and involves the *a priori* assumption of a nearly-free-electron like final state $|\mathrm{f}\rangle$ (Himpsel, 1980; Damascelli, 2004). With this assumption the $E_\mathrm{f}(\mathbf{k})$ dispersion is

$$E_\mathrm{f}(\mathbf{k}) = \frac{\hbar^2\mathbf{k}^2}{2m_e} - |E_0| = \frac{\hbar^2(\boldsymbol{k}_{\parallel}{}^2 + k_\mathrm{z}^2)}{2m_e} - |E_0|. \tag{3.4}$$

with the bottom of the VB E_0 and E_f being referenced to $\mathrm{E_F}$ as described in figure 3.1 (c). Using equation 3.3 and considering $E_\mathrm{kin} = E_\mathrm{f} - E_\mathrm{V}$, the perpendicular momentum can be described as

$$k_z = \frac{1}{\hbar}\sqrt{2m_e(E_{\text{kin}}\cos^2\theta + |E_0| + \Phi)}. \tag{3.5}$$

The energy from the bottom of the VB to the vacuum level is called inner potential $V_0 = |E_0| + \Phi$. It can be seen as reference energy of the electron inside the crystal. Performing photon-energy-dependent measurements at normal electron emission, i.e. $\mathbf{k}_{\parallel} = 0$, V_0 can be determined by the periodicity of the E(k_z) dispersion.

It is important to note that the accuracy of this method is limited by the assumption of nearly-free-electron like final states. While this is often a justified assumption for states far above E_V, in principle, the bulk final state can largely deviate from a free-electron behavior. In this case the assumption of the method is violated and therefore the accuracy of the k_z determination is lowered.

3.1.2 Obtaining Spin Resolution*

This section provides a short summary on how spin resolution in ARPES and IPE is achieved at the setups at the university of Münster and at the HiSOR in Hiroshima. A detailed description about spin resolution in photoemission techniques can be found in the supplement of Eickholt *et al.* (2018b).

In SARPES a spin polarization detector has to be used after the photoelectrons have passed an energy analyzer. Low-energy scattering on a high-Z material can result in an asymmetry $A = (n_{\text{l}} - n_{\text{r}})/(n_{\text{l}} + n_{\text{r}})$ between left- and right-scattered electrons (n_{l} and n_{r}), caused by SOC. Alternatively, a magnetic target can be used. Here, two measurements on the oppositely magnetized target (**M** and **-M**) lead to an asymmetry $A = (n_{\mathbf{M}} - n_{\text{-}\mathbf{M}})/(n_{\mathbf{M}} + n_{\text{-}\mathbf{M}})$.

The obtained scattering asymmetry reflects the spin polarization of the incoming electrons. The spin separation is, however, not complete. The spin-resolving power of the detector is characterized by the so-called Sherman function S, defined by the scattering asymmetry A for a 100% polarized electron beam. Provided the Sherman function S of a detector is known from an inde-

* Text excerpts of this subsection have been published in the supplement of Eickholt *et al.* (2018b). Reprinted with permission from Eickholt *et al.* (2018b). Copyright (2018) by the American Physical Society.

pendent calibration measurement, the spin polarization of the photoelectrons $P = (N_\uparrow - N_\downarrow)/(N_\uparrow + N_\downarrow)$ is given by

$$P = \frac{A}{S}. \tag{3.6}$$

The individual or sometimes called partial spin-up and spin-down data $N_\uparrow$ and $N_\downarrow$ are obtained from the spin polarization P and the total number of electrons $n = n_\mathrm{l} + n_\mathrm{r}$ (or $n = n_\mathbf{M} + n_{\text{-}\mathbf{M}}$) by

$$N_{\uparrow,\downarrow} = \frac{N}{2}(1 \pm P) = \frac{N}{2}(1 \pm \frac{A}{S}) \tag{3.7}$$

with $N = N_\uparrow + N_\downarrow = n$. n denotes the number of electrons measured with the non-ideal spin-polarization detector, N the number of electrons measured with an hypothetically ideal spin polarization detector. In the case of different sensitivities of the electron detectors for left and right scattering (e.g. SPLEED detector) additional apparatus asymmetries appear that have to be taken care of. One possibility is to perform two separate measurements with same experimental conditions but with reversed spin polarization. For instance, this is achieved when measuring a magnetic sample, by reversing its magnetization. When performing the two measurements a and b, the spin polarization is calculated as

$$P = \frac{1}{S}\frac{\sqrt{n_{l,a}n_{r,b}} - \sqrt{n_{r,a}n_{l,b}}}{\sqrt{n_{l,a}n_{r,b}} + \sqrt{n_{r,a}n_{l,b}}}. \tag{3.8}$$

For the nonmagnetic material studied in this thesis, the apparatus asymmetry of the SPLEED detector were taken care of by assuming a spin-independent background and correcting the apparatus asymmetry accordingly. The validity of this approach in case of SL WS_2 (Sec. 5.2.3) is proved by the observation of two *fully spin-polarized* features with *opposite spin polarization* in the *same spectrum*. Any different handling of the apparatus asymmetry would lead to an unphysical result in this case. More detailed descriptions about the described issues are found in the literature, see, e.g. (Kessler, 1985; Kisker, 1985; Johnson, 1997).

In IPE, spin resolution is achieved by using a spin-polarized electron beam. However, the spin polarization P of the electron beam is not 100%. For the setup in Münster it is $P = 29\%$ (Stolwijk *et al.*, 2014). The incomplete spin polarization of the electron beam in IPE plays the same role as the incomplete spin separation

of the spin polarization detector in ARPES. Therefore, to obtain the individual spin spectra, the equivalent procedure as in ARPES has to be applied. P has to be known from an independent calibration measurement. Here, $n_{\uparrow,\downarrow}$ denote the number of photons detected for the two opposite spin-polarization directions of the electron beam. The observed asymmetry in the number of photons $A = (n_\uparrow - n_\downarrow)/(n_\uparrow + n_\downarrow)$ is smaller than the asymmetry for a hypothetically 100% spin-polarized beam $A/P = (N_\uparrow - N_\downarrow)/(N_\uparrow + N_\downarrow)$. The individual spin spectra are obtained from the beam spin polarization P and the total number of photons $N = N_\uparrow + N_\downarrow = n_\uparrow + n_\downarrow$ by

$$N_{\uparrow,\downarrow} = \frac{N}{2}(1 \pm \frac{A}{P}). \tag{3.9}$$

In the case of non-collinearity between the spin-quantization axes of sample and spin polarization detector or electron source, this angle ζ has to be taken into account. Equation 3.9 modifies to

$$N_{\uparrow,\downarrow} = \frac{N}{2}(1 \pm \frac{A}{P \sin\zeta}). \tag{3.10}$$

Equation 3.10 has to be used to obtain partial spin spectra with out-of-plane spin polarization, as measured in chapter 5.

3.2 Experimental Setups*

Surface sensitive methods such as ARPES or IPE have to be performed in ultra-high-vacuum (UHV) (p$< 10^{-9}$ mbar) to avoid contamination of sample surfaces. The base pressure of the experimental (S)ARPES and (SR)IPE setups is p$\approx 10^{-11}$ mbar. At this pressure the surfaces of samples such as $ReSe_2$ and WS_2 stay clean for at least several days and possibly much longer. Furthermore, ARPES and IPE require single-oriented samples for **k**-resolution. The experimental setups include methods for *in-situ* preparing, cleaning and characterization of the sample surface. Micromechanical exfoliation can be applied to create well ordered and clean sample surfaces when studying weakly-bound layered materials (Novoselov *et al.*, 2005). SL samples such as $WS_2/Au(111)$ (see Ch. 5) are cleaned by annealing.

* Text excerpts of this section have been published in Eickholt *et al.* (2018a,b). Reprinted with permission from Eickholt *et al.* (2018a,b). Copyright (2018) by the American Physical Society.

A standard technique to characterize the surface structure is low-energy electron diffraction" (LEED) which is highly surface sensitive and generates an image of the reciprocal lattice of the sample surface (Ertl and Küppers, 1985; Henk, 2001). This image allows to deduce the information about the periodic spatial structure. In addition, LEED was used to align the sample for IPE or ARPES. To get information about non-periodic impurities, the element sensitive Auger electron spectroscopy (AES) (Rivière, 1973; Narumand and Childs, 1999) was applied.

Target current spectroscopy (TCS) has been used to obtain the work function Φ_{Sample} of the samples. TCS measures the sample current as a function of the energy e·U of the incoming electrons. Φ can be deduced from the onset of the TCS spectrum. Determining Φ_{Sample} requires the knowledge of the work function of the electron source. It can be obtained via independent calibration measurements of a sample with a known work function. In chapters 4 and 5 the TCS spectra are depicted with reference to the Fermi energy by using Φ_{Sample}.

3.2.1 Experiments at the University of Münster

The setup in Münster was used for the measurements of $ReSe_2$ in section 4.5 and WS_2 in Chap. 5. The UHV system consists of three chambers connected by a transfer and storage system (see Fig. 3.2). The "*preparation chamber*" has a load-lock and the sample surfaces can be cleaned and characterized. Heating of the samples is performed within this chamber while the micromechanical exfoliation was done within the load-lock at a pressure of $p \approx 10^{-8}$ mbar. LEED and AES are used for characterization of the sample surface. Further information about local electronic and structural properties can be obtained by a scanning tunneling microscope (STM)[2] located in a separate chamber.

The "*analysis chamber*" contains the combined SARPES and SRIPE setup (see Fig. 3.2) and is made out of μ-metal to shield external magnetic fields that heavily influence low-energy electrons.

SARPES measurements are performed with unpolarized light of a gas discharge lamp (HIS 13 by FOCUS GmbH) using the He I α line ($h\nu = 21.22\,eV$). The illumi-

[2] An introduction and details to STM are given in (Binnig and Rohrer, 1983; Bai, 2000).

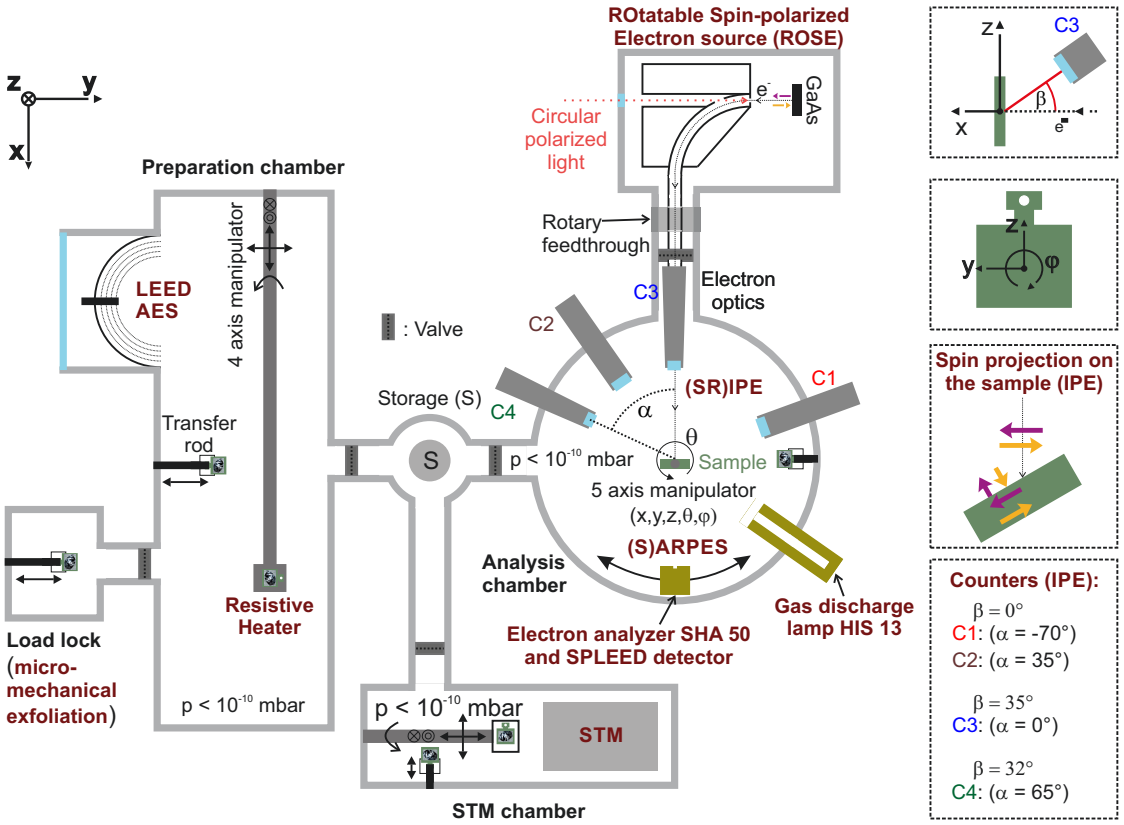

Figure 3.2: Overview of the UHV setup in Münster and details of the combined SRIPE and SARPES setup with the electron source (Stolwijk *et al.*, 2014) in *"horizontal configuration"*. The spin projection onto the sample in this configuration is depicted in the second lowest right panel.

nated area on the sample is within the mm range. For detecting the photoemitted electrons, a simulated 50 mm hemispherical analyzer (SHA 50 by FOCUS GmbH) is used. It is mounted on a goniometer for angle-resolved measurements. In the present work the energy resolution was about 160 meV full width at half maximum (FWHM). The angular resolution is about $\Delta\theta_{\mathrm{PE}} \approx 1^\circ$ (Budke *et al.*, 2007a). The spin polarization of the emitted electrons is detected via spin-polarized low-energy electron diffraction (SPLEED) of a W(100) crystal (Feder and Kirschner, 1981; Yu *et al.*, 2007). This detector has a Sherman function of $S = 0.24 \pm 0.03$ (Budke *et al.*, 2007a) and is simultaneously sensitive to two spin components: (i) perpendicular to the surface (out-of-plane) and (ii) within the surface and parallel to $\mathbf{k}_{\|}$.

For spin-resolved IPE, a spin-polarized electron source provides an electron beam of about 3 mm diameter with a beam divergence (Zumbülte *et al.*, 2015) of about $\pm 1.5°$. Considering this beam divergence, the momentum resolution of an electronic state[3] 1 eV above E_F is ± 0.03 Å^{-1}. The spin polarization of the electron beam is $P = 0.29 \pm 0.03$. The required spin direction can be set by mechanically rotating the spin-polarized electron source (Stolwijk *et al.*, 2014). In the "*vertical configuration*" the setup is sensitive to the in-plane spin component that is perpendicular to $\mathbf{k}_{\parallel}$ and sometimes called "Rashba component" in the literature. In the "*horizontal configuration*" and for off-normal electron incidence on the sample, the setup is sensitive to the out-of-plane and in-plane parallel spin components simultaneously (see inset of Fig. 3.2). In many cases one of these two spin components is prohibited by symmetry considerations or can be excluded with additional measurements. In section 5.2.3 the spin-quantization axis of electronic states is out-of-plane and the electron beam is transversely spin polarized. As a consequence, the spin sensitivity is zero for normal electron incidence and increases with increasing angle of incidence θ as depicted in figure 3.2.

Emitted photons are detected by a band-pass-type gas detector with a mean detection energy of $h\nu = 9.9$ eV (Budke *et al.*, 2007b). The detector uses the ionization threshold of acetone as high pass, and the transmission cutoff of a CaF_2 window as low pass. A detailed description, including operating modes[4], is published (Thiede *et al.*, 2018). Four detectors, called C1, C2, C3 and C4, are installed at different positions and can be used to gain information on the spatial emission characteristics. C1 and C4 can be moved close to the sample to maximize the count rates due to the increase of the solid angle of the detectors.

The described electron source and gas detectors result in an apparatus function of the SRIPE experiment that is Gaussian shaped with a total energy resolution of $\Delta E_{IPE} = 350$ meV FWHM (Budke *et al.*, 2007b). If not otherwise noted, the experiments in Münster were performed at room temperature.

[3] Considering the photon detection energy of $h\nu = 9.9$ eV and a typical workfunction of $\phi = 5$ eV.

[4] Here, the detector is operated in the proportional mode with Acetone for the IPE data in chapter 5 with exception of mirror domain SL WS_2. The latter and the $ReSe_2$ data are gained by using the Geiger-Müller regime of the detector with a mixture of argon and acetone.

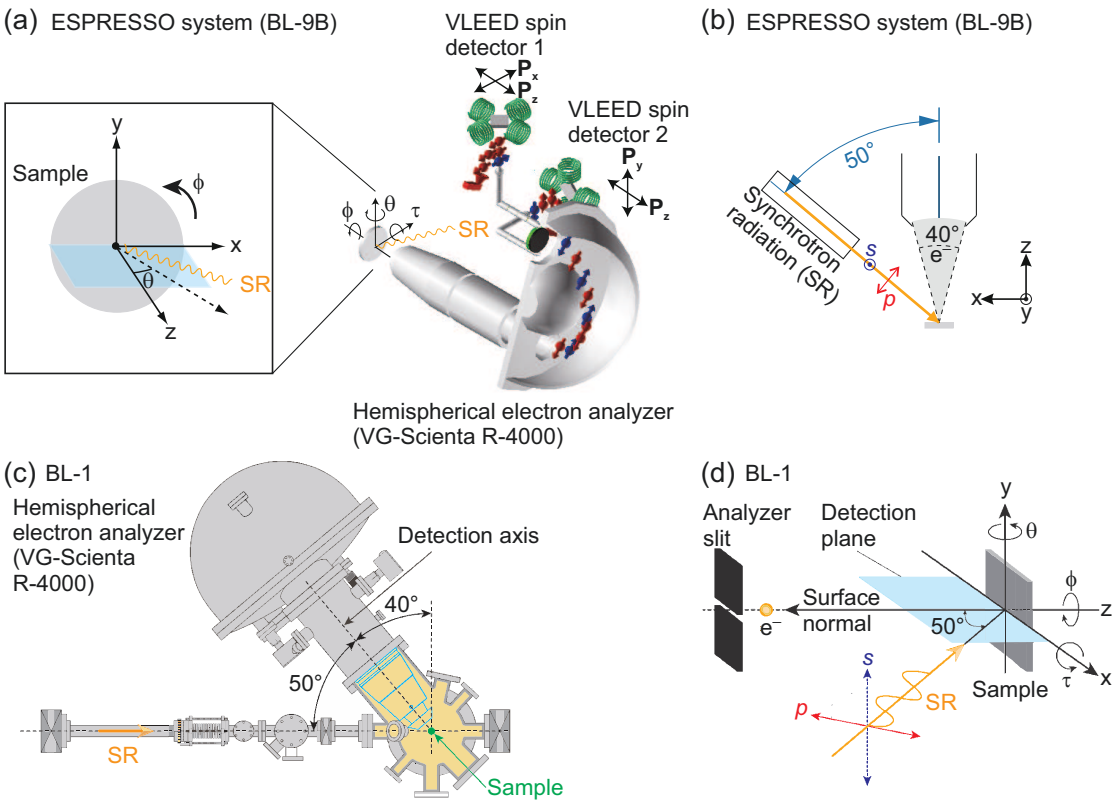

Figure 3.3: (a,b) Details of the experimental geometry and schematic of the ESPRESSO system (HiSOR BL-9B), including the VLEED spin detector. Adapted from Okuda *et al.* (2015); Miyamoto (2016). (c,d) Schematic of the analysis UHV chamber (c) and details of the experimental geometry (d) of HiSOR BL-1 (Schwier, 2016). Both setups are equipped with a 6-axis manipulator allowing adjustment of *x,y,z,* polar (θ), azimuthal (ϕ), and tilt angle (τ).

3.2.2 Photoemission Experiments at HiSOR

The occupied electronic structure of bulk $ReSe_2$ and ReS_2 was investigated at beamlines BL-9B and BL-1. Micromechanical exfoliation of the samples was performed by using a fork to grab the adhesive tape in the load-lock of BL-9B and the preparation chamber of BL-1, respectively . During this process the pressure was better than 4×10^{-10} mbar. Both beamlines have installed a "VG Scienta R4000" electron analyzer for ARPES and a 6-axis manipulator (*x,y,z,* polar θ, azimuthal ϕ and tilt angle τ). The angular resolution is better than 1° for θ, ϕ and τ. Different experimental parameters (slit sizes, pass energy of the analzer and photon energy) result in different total energy resolutions of 60 meV FWHM and 120 meV FWHM

for the experiments at BL-9B and BL-1[5] , respectively. The illuminated area, i.e. the investigated area in ARPES, is slightly larger (2.0 mm and 0.7 mm in horizontal and vertical direction in Fig. 3.3) at BL-9B than at BL-1 (0.5 mm and 1.5 mm). In both setups the light incidence lies within the "detection plane" (defined as in Fig. 3.3) and has an angle of 50° to the surface normal. If not otherwise noted, experiments have been performed with *p*-polarized light at a sample temperature of 150 K and at a pressure better than 1×10^{-10} mbar.

At BL-9B spin resolution can be added to ARPES utilizing the ESPRESSO VLEED spin detector (Okuda *et al.*, 2008, 2015) that is sketched in figure 3.3 (a). Electrons, after passing the energy analyzer, are guided into one of the two VLEED detectors on a magnetized Fe(001)p(1×1)-O target. The targets are magnetized by a pair of coils. The Sherman function was $S = 0.28$ during the measurements. Each of the two orthogonally placed VLEED detectors can analyze two independent spin-polarization directions. By using both of the detectors, 3D spin sensitivity is achieved. Applying spin resolution at BL-9B slightly decreases the total energy resolution, in the present work to about 70 meV FWHM.

[5]The energy resolution decreases with increasing photon energy. The given value refers to a photon energy of 150 eV, the largest photon energy used in experiments at BL-1.

4

Anisotropic Electronic Structure of $ReSe_2$*

Layered semiconducting transition metal dichalcogenides are promising materials for optoelectronic applications due to their fascinating electrical and optical properties (see Ch.2). WX_2 and MoX_2 (with X = S, Se) are regarded as prototypical materials. However, a direct band gap, necessary in optical applications, is only realized in a SL of these materials (see Ch. 5 and (Mak *et al.*, 2010; Cheiwchanchamnangij and Lambrecht, 2012; Jin *et al.*, 2013; Cappelluti *et al.*, 2013; Zhang *et al.*, 2014a; Yeh *et al.*, 2015)). Moreover, the hexagonal crystal structure of WX_2 and MoX_2 results in an isotropic in-plane response to the polarization of incident light (Arora *et al.*, 2017).

In contrast, the Re-based TMDCs (ReX_2) are reported to have anisotropic in-plane physical properties (Wolverson *et al.*, 2014; Chenet *et al.*, 2015; Cui *et al.*, 2015; Lin *et al.*, 2015; Zhao *et al.*, 2015; Zhong *et al.*, 2015; Nagler *et al.*, 2016; Qiao *et al.*, 2016; Arora *et al.*, 2017) due to their distorted 1*T* structure (denoted as 1*T*′) and the formation of Re-Re chains of "diamond-shaped" clusters, shortly called "diamond chains", along the *a*-axis (Lamfers *et al.*, 1996). Furthermore, ReX_2 is predicted to have weak interlayer coupling and, hence, only a small dependence of the band structure on the crystal thickness (Tongay *et al.*, 2014). Consequently,

* Figures and text excerpts of this chapter have been published in Eickholt *et al.* (2018a). Reprinted with permission from Eickholt *et al.* (2018a). Copyright (2018) by the American Physical Society. If not otherwise noted, band structure calculations in this chapter were performed by J. Noky during his master thesis (Noky, 2017).

no indirect-to-direct band-gap crossover upon reducing the thickness is expected. However, there is an ongoing discussion (Marzik *et al.*, 1984; Tiong *et al.*, 1999; Ho *et al.*, 2001; Ho and Huang, 2004; Wolverson *et al.*, 2014; Yang *et al.*, 2015; Zhong *et al.*, 2015; Arora *et al.*, 2017; Hart *et al.*, 2017), whether Re-based TMDCs are direct or indirect semiconductors. To understand the anisotropic physical properties and the band gap, experimental and theoretical studies of the electronic structure are indispensable. Therefore the electronic structure of bulk $ReSe_2$ was studied with (S)ARPES and (SR)IPE.

The outline of this chapter is as follows. Basic structural properties and the results of different band structure calculations are discussed in section 4.1. The surface quality of the bulk $ReSe_2$ sample is characterized in section 4.2. In SARPES a surprisingly strong spin polarization is observed for centrosymmetric $ReSe_2$ and its sister material ReS_2 (Sec. 4.3). Photon-energy-dependent ARPES provides information about the position of the VBM in **k**-space (Sec. 4.4). Information about the unoccupied electronic structure and the resulting band gap is presented in section 4.5. Subsequently, a characteristic direction in the anisotropic occupied electronic structure of bulk $ReSe_2$ is extracted by an ARPES study in section 4.6.

4.1 Crystal Structure and Calculated Electronic Structure of $ReSe_2$

$ReSe_2$ crystallizes in a distorted 1*T* structure (1*T*′) (Lamfers *et al.*, 1996). The unit cell is depicted in Fig. 4.1 (a). The Re atoms form a parallelogram-like shape with an octahedral coordination of the Se atoms around it. This reduces the crystal symmetries down to one, i.e. only inversion symmetry is retained. Within a layer, the Re atoms build so-called ”diamond-chains” along the crystallographic *a*-axis [100] (see Fig. 4.1 (c)), leading to a pronounced in-plane anisotropy. The bulk crystal consists of these layers which are stacked on top of each other (see Fig. 4.1 (b) and (d)) and are weakly coupled, predominantly by van-der-Waals interaction. Note that the lattice vector **c** is not perpendicular to the layers resulting in a horizontal shift between them.

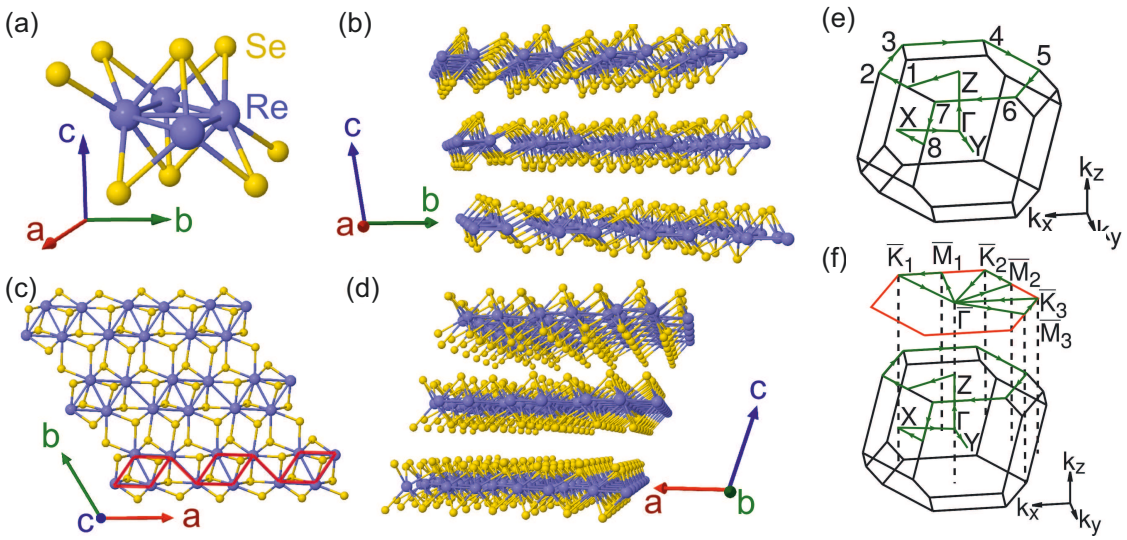

Figure 4.1: (a) Unit cell of 1T′-$ReSe_2$. (b) Side view of the bulk crystal along the *a*-axis, which is equivalent to [100]. (c) Top view along the *c*-axis with the "diamond chains" marked in red. (d) Side view of the bulk crystal along the *b*-axis. (e) Bulk BZ of $ReSe_2$. High-symmetry points are marked with capital letters. The path, along the band structure is calculated, is indicated by a green line with numbers. (f) SBZ with high-symmetry points in relation to the ones of the bulk.

In Fig. 4.1 (e) the bulk BZ of $ReSe_2$ is shown. It has a triclinic structure, so the irreducible part of the BZ is half of the full one. The SBZ, corresponding to an exfoliated surface, is shown in Fig. 4.1 (f) in red. It is almost hexagonal but the reduced symmetry leads to nonequivalent $\overline{\text{M}}$- and $\overline{\text{K}}$-points. Here, $\overline{\Gamma}$-$\overline{\text{M}}_1$ coincides with the real space direction perpendicular to the "diamond chains" and $\overline{\Gamma}$-$\overline{\text{K}}_3$ with the direction parallel to the chains. It is important to note that the reduced symmetry also leads to an interesting effect for two-dimensional cuts through the BZ: in these cuts inversion symmetry only holds for planes which contain Γ or Z. This is because the inversion center is at Γ.

When investigating the band structure of $ReSe_2$, it is important to note that each band is twofold degenerate due to inversion and time reversal symmetry. Firstly, band structure calculations within LDA and *GdW* approximations of bulk $ReSe_2$ are discussed regarding their results of the band gap. Computational details are published in Eickholt *et al.* (2018a). The LDA band structure is presented as dashed lines in Fig. 4.2 (e). Following the path depicted in Fig. 4.1 (e) it turns out

that bulk $ReSe_2$ has an indirect band gap of 0.98 eV. However, since the shown path covers only a small part of the BZ, calculations of the HVB and the LCB in the whole BZ were carried out. It results that in LDA the global VBM and CBM are both located away from any high symmetry line. The CBM is located at the edge of the BZ (see Fig. 4.2 (a)) at a point called Ξ. The position of the VBM in LDA is shown in Fig. 4.2 (c). It is located along the $\overline{\Gamma}$-$\overline{M}_1$ line of the SBZ but not at any special k_z. This point will be called Λ. Looking at the full BZ, LDA finds an indirect band gap of $E_G^{LDA} = 0.86\,\text{eV}$ in accordance with a recent study (Hart *et al.*, 2017).

Taking many-body effects into account by using the *GdW* approximation (Rohlfing, 2010), the band structure undergoes some drastic changes. The quasiparticle band structure is shown in Fig. 4.2 (e) with solid lines and colored dots. Bulk $ReSe_2$ is found to be a direct band gap material with a band gap of $E_G^{GdW} = 1.49\,\text{eV}$. Looking at the whole BZ shows that the VBM and the CBM are both located at the Z point (see Fig. 4.2 (b) and (d)). Additionally, the dispersion of the HVB on the Γ-Z line undergoes a strong change when including many-body effects. The band width is modified from $\approx 50\,\text{meV}$ in LDA to $\approx 200\,\text{meV}$ in *GdW*.

Considering the surface projected band structure, which is shown in Fig. 4.2 (f), the LCB exhibits a significantly flatter E(**k**) dispersion in comparison to the HVB. Within the VBs, a much smaller band width of the HVB along $\overline{\Gamma}$-$\overline{M}_1$ is found than along any other direction. This line corresponds in real space to the direction perpendicular to the "diamond chains". In the inset, the HVB is shown for different values of k_z. Note that the band maximum along $\overline{\Gamma}$-$\overline{M}_1$ is not for all k_z values at $\overline{\Gamma}$. The global maximum (i. e., the VBM) is reached for $k_z = 0.5\mathbf{c}^*$ at $\overline{\Gamma}$, i. e. at the Z point of the three-dimensional BZ ($\mathbf{c}^*$ is the reciprocal lattice vector corresponding to the third lattice vector).

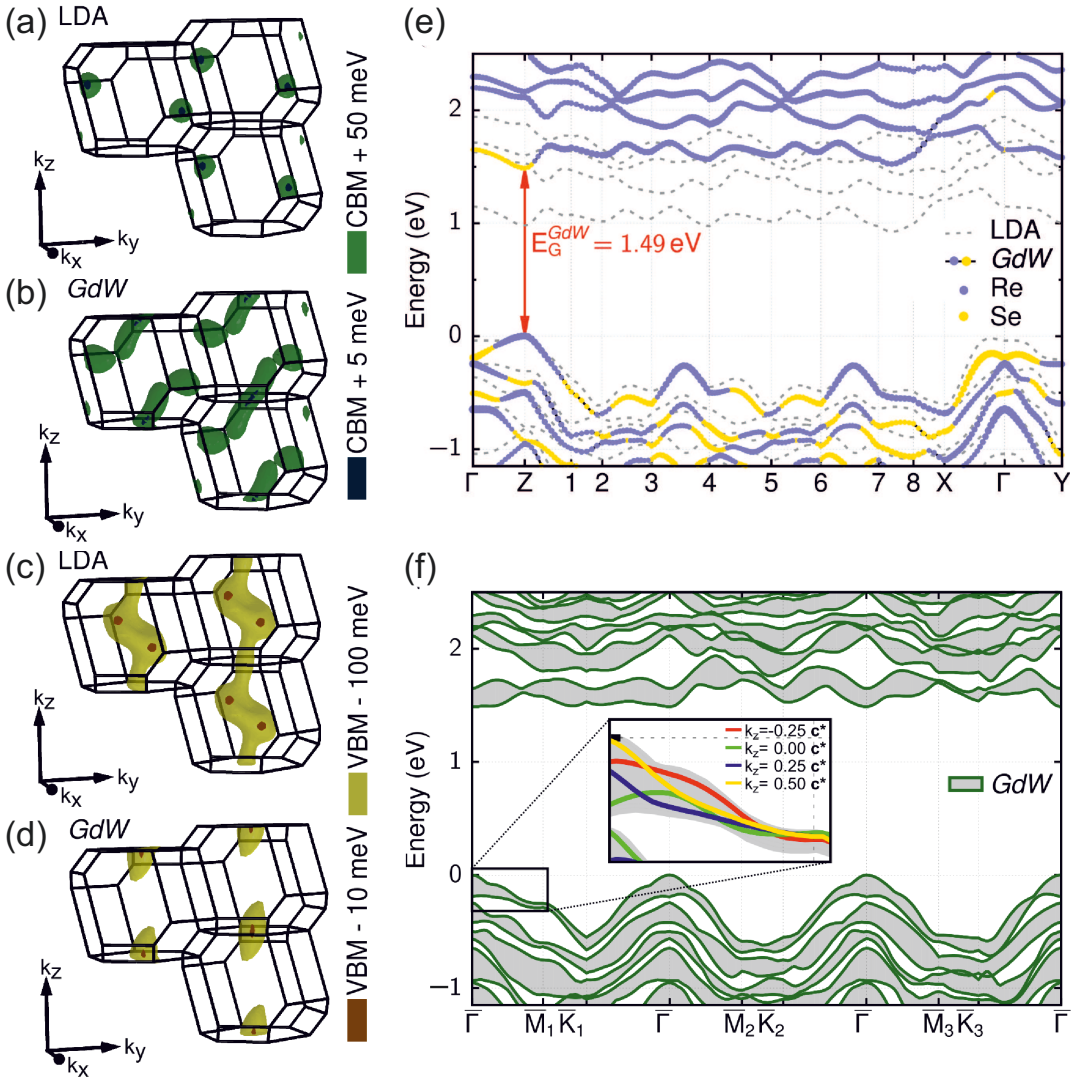

Figure 4.2: (a) Location of the CBM at Ξ according to LDA. (b) Location of the CBM at Z according to *GdW*. (c) Location of the VBM at Λ according to LDA. (d) Location of the VBM at Z according to *GdW*. (e) Band structure of bulk $ReSe_2$ in LDA (gray dashed) and *GdW*(gold and blue dots). The dot color shows the main band character, gold means Se-p-orbitals and blue Re-d-orbitals. (f) Bulk band structure projected along k_z. The inset shows the HVB for different fixed values of k_z.

4.2 Characterization of the $ReSe_2$ and ReS_2 Samples

The bulk $ReSe_2$ sample originates from the "2DSemiconductor" company[1]. (S)ARPES measurements have been performed at two beamlines, BL-1 and BL-9B, at HiSOR. The unoccupied electronic structure was studied with (SR)IPE at the University of Münster. The sample was prepared *in-situ* by mechanical exfoliation in both cases (compare Sec. 3.2.1 and 3.2.2).

Since the sample is semiconducting, a first important test is to look for possible sample charging during the measurements. In general this is more of an issue for IPE than for ARPES because of the order of magnitudes higher electron currents (μA vs nA) applied in the former. Temperature-dependent ARPES measurements showed the onset of sample charging for temperatures below 70 K. In order to avoid charging effects, the ARPES measurements were performed at a much higher sample temperature of 150 K. To increase sample conductivity, IPE measurements are conducted at room temperature. Charging effects in IPE are tested by performing two consecutive room-temperature measurements with different sample currents for normal electron incidence at the same sample position. The first measurement was conducted with a typical sample current of the IPE experiments of about 800 nA. The second measurement was performed with a low sample current of about 8 nA that is similar to sample currents occurring during ARPES experiments. The results are shown in figure 4.3 (a). The low sample current of 8 nA leads, despite long measuring time of about 12 h, to poor statistics in the respective measurement. Nonetheless, the spectra show no sign of an energy shift that indicates sample charging. It is unlikely that an energy shift already occurs at sample currents lower than 8 nA for two reasons. (i) ARPES is also operating with roughly the same emitted electron current in the order of nA. It shows no sign of sample charging above 70 K. (ii) The sample is intrinsically doped as can be deduced by the position of the VBM and the size of the band gap (Sec. 4.4 and 4.5). Hence, it is concluded that no significant sample charging is present during (S)ARPES and (SR)IPE measurements at 150 K and room temperature, respectively.

[1] http://www.2Dsemiconductors.com/

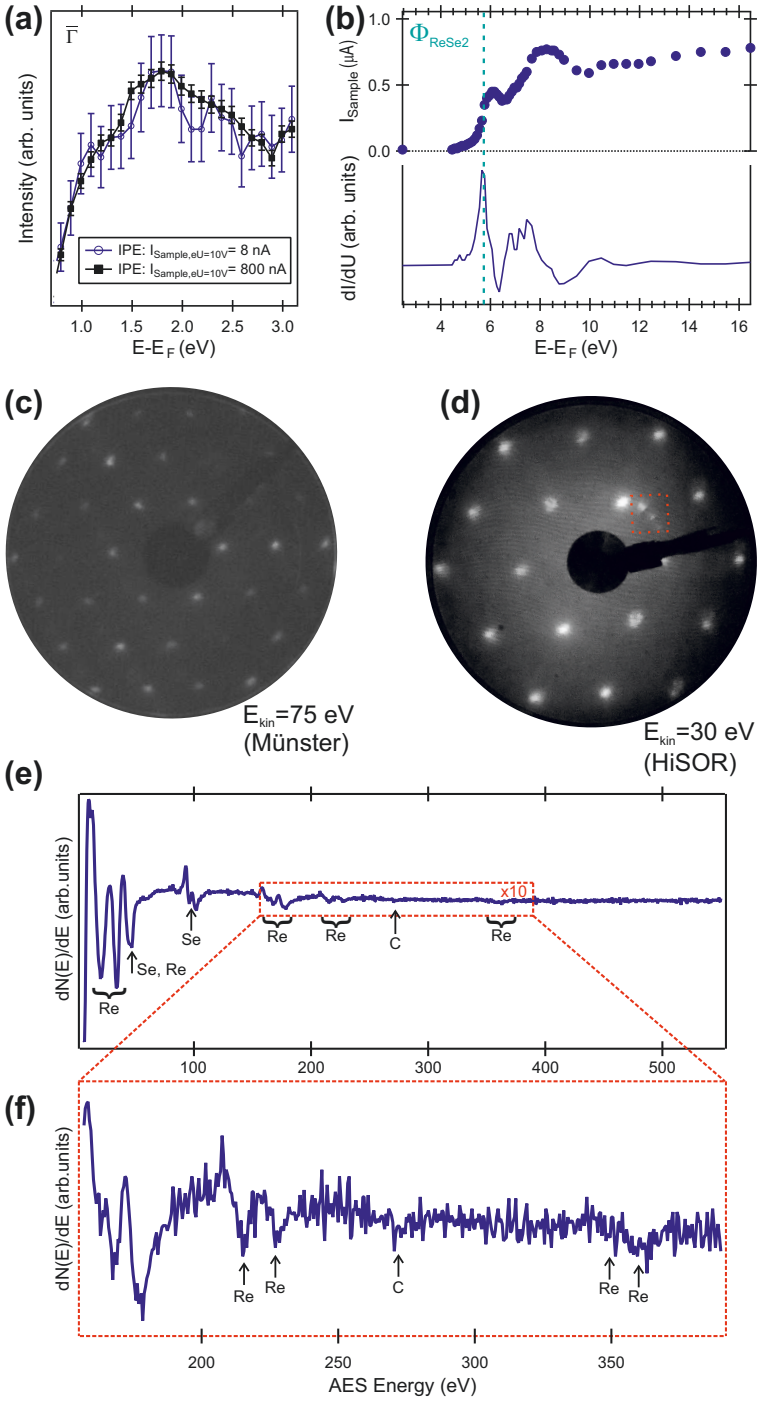

Figure 4.3: (a) IPE spectra at $\overline{\Gamma}$ for different incident electron currents. (b) TCS performed in Münster to determine the work function. (c) LEED image of $ReSe_2$ taken at the UHV setup in Münster before TCS and (SR)IPE measurements. (d) LEED pattern at $E = 30\,\text{eV}$ taken at BL-9B of HiSOR after (S)ARPES measurements. The screen was recorded manually with a camera. The spots within the red dashed box are artificial due to light reflection from the outside of the screen. (e) AES spectrum taken after (S)ARPES measurements at BL-9B (excitation energy of 3 keV). The dashed box indicates the area that is presented enlarged in (f). AES features are assigned according to standard spectra in Davis *et al.* (1976).

The sample quality was further checked by LEED, TCS and AES. LEED images were taken in the setups in Münster and at HiSOR (see Fig. 4.3 (c) and (d)). They clearly show the quasi-hexagonal structure, expected for $ReSe_2$. The electron beam spot size in LEED is larger than the average crystallite size of the sample. As a result, the LEED spots are broadened due to averaging over more than one crystallite, with possible slight misalignment of the contributing crystallites. This possible misalignment is estimated to smaller than one degree and contributes to broadening of the IPE and ARPES spectra due to the finite electron and light spot size (compare Ch. 3). A misalignment of one degree translates roughly into $0.02\,\text{Å}^{-1}$,$0.07\,\text{Å}^{-1}$ and $0.1\,\text{Å}^{-1}$ in **k**-space for hν=10 eV, hν=64 eV, and hν=150 eV photon energy, respectively.

Further, the chemical composition of the surface is investigated with AES. The expected[2] AES features of Re and Se are present in figure 4.3 (e) along with a small feature indicating minor residual carbon. The latter is only visible in the enlarged area of the spectrum in figure 4.3 (f). The AES spectrum was taken after (S)ARPES measurements at BL-9B. Note that during ARPES measurements, at a pressure of $p \approx 10^{-11}$ mbar, no change in the measured spectra was observed within a few days, indicating a highly inert surface under ultra-high vacuum conditions. Therefore, the residual carbon was likely present during photoemission experiments. Finally, the onset in TCS is used to determine the work function of the sample to $\phi = 5.76$ eV. At an energy of about 8 eV a peak is observed in the TCS spectrum. It is attributed to bands at this energy, with which the incident electrons can couple. The TCS measurements were performed in Münster with the same sample.

The ReS_2 sample, used to obtain additional information about the observed spin polarization, is characterized in appendix A.1. LEED and AES indicate a similar sample quality for ReS_2 as described above for $ReSe_2$.

[2] According to standard spectra in Davis *et al.* (1976).

4.3 Spin Signal in Inversion-Symmetric $ReSe_2$ (ReS_2)

The anisotropic properties of $ReSe_2$ are caused by its low symmetry. However, one symmetry is present in both, bulk and SL of $ReSe_2$: the space inversion symmetry that leads to Kramers degeneracy. As a result and in contrast to SL WS_2 (see Ch. 5), no spin-dependent electronic bulk states are expected for $ReSe_2$ and its sister material ReS_2, despite the strong SOC due to the heavy Re atoms.

While the electrons inside the crystal are not spin polarized, emitted photoelectrons can be spin polarized and potentially be utilized. In fact, the GaAs photocathode (Pierce and Meier, 1976), used in the present work as a spin-polarized electron source for SRIPE, is an example of this. Importantly, the different spin polarization of emitted photoelectrons and electrons inside the crystal are not due to a spin flip during the photoemission process. Spin-flip transitions typically only have an negligibly small effect on the spin polarization of photoelectrons (Wissing *et al.*, 2014). Rather than flipping the spin, the photoelectrons are spin polarized due to spin-dependent photoemission dipole matrix elements (Jozwiak *et al.*, 2011). Ultimately, this "extrinsic spin polarization" is originated by the distinct symmetry of the experiment and the sample.

Consequently, it was proposed to control and manipulate the spin polarization of photoelectrons by tuning experimental parameters (Kuroda *et al.*, 2016; Miyamoto *et al.*, 2018). Note that for time reversed transitions, i.e. in IPE, the tuning of spin polarization is also possible, as shown by SRIPE measurements of intrinsically unpolarized electronic states of W(110) in normal-electron-incidence geometry (Wortelen *et al.*, 2015). Given the knowledge of the experimental symmetry and the symmetry of the involved electronic states, spin effects can be described in the framework of the one-step model of photoemssion (Pendry, 1981; Henk *et al.*, 1996). In general, the less overall symmetry in experiment and sample, the more spin effects are possible. Therefore, $ReSe_2$ and ReS_2, due to their low symmetry, are perfect candidates for producing and potentially manipulating spin-polarized photoelectrons. A detailed analysis of the spin effects within the one-step model is challenging due to the low symmetry. Before doing these calculations, it is

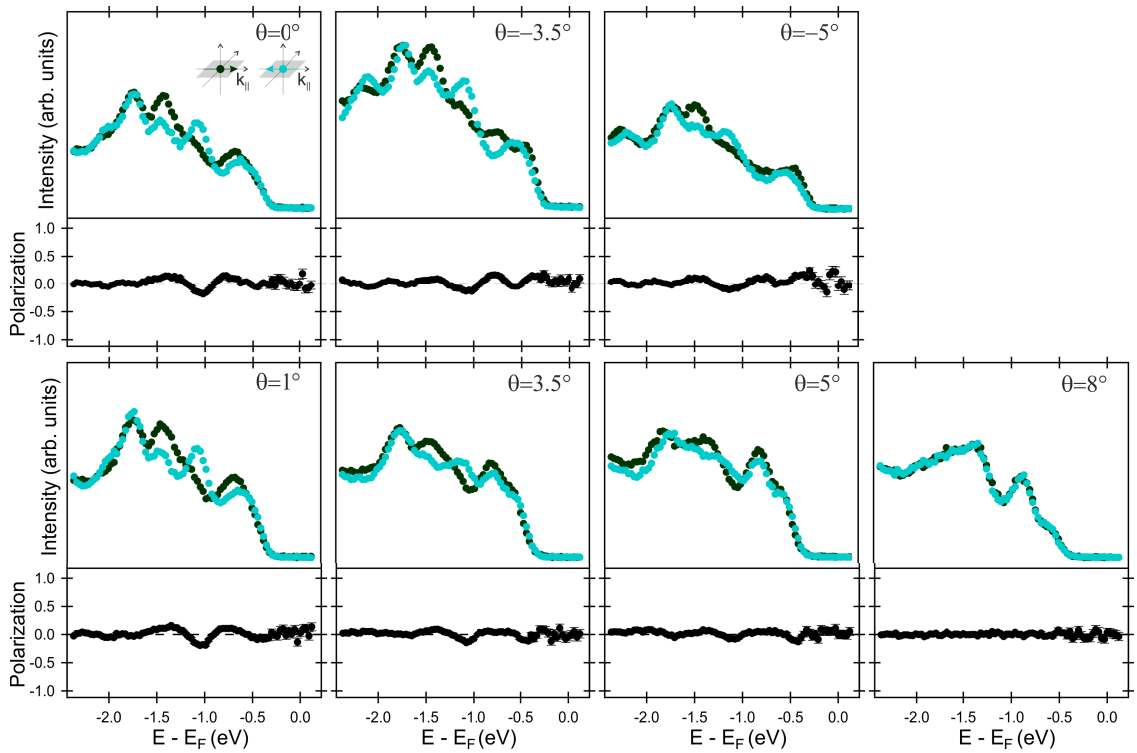

Figure 4.4: SARPES spectra and respective spin polarization P (as defined in section 3.1.2) of $ReSe_2$ with *p*- and *s*-polarized light (hν=21 eV) and sensitivity to the x component (green and cyan dots) of the spin polarization $\mathbf{P}_x$.

important to experimentally determine if possible spin effects exist.

SARPES measurements of $ReSe_2$ have been conducted at HiSOR BL-9B using (if not otherwise noted) *p*-polarized synchrotron light with an energy of hν =21 eV. The results are shown in Figs. 4.4, 4.5 and 4.6. Remarkably, high spin polarization of photoelectrons of up to 50 % without any background subtraction is observed. Some features, e.g. at about -2 eV for normal electron emission and $\mathbf{P}_y$ (Rashba) spin direction, have almost 100% spin polarization after background subtraction. As a consequence of the low symmetry, spin effects exist for any component of the spin polarization[3] $\mathbf{P}$, yet most pronounced in y direction.

In the following, possible effects contributing to the observed spin polarization will be discussed. First of all, it is important to distinguish between "intrinsic"

[3]The definition of $\mathbf{P}_x$, $\mathbf{P}_y$ and $\mathbf{P}_z$ is shown in the legend of figures 4.4, 4.5 and 4.6.

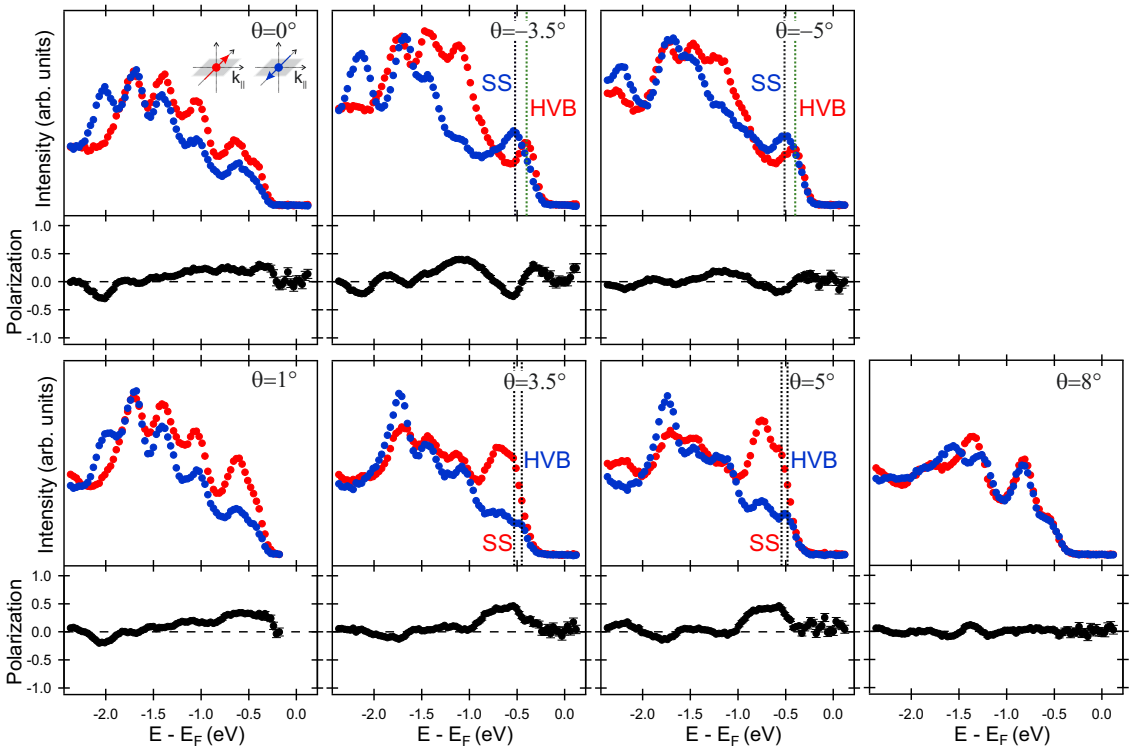

Figure 4.5: SARPES spectra and respective spin polarization P (as defined in section 3.1.2) of $ReSe_2$ with *p*- and *s*-polarized light (hν=21 eV) and sensitivity to the y component (red and blue dots) of the spin polarization $\mathbf{P}_y$. The marked features are discussed in the text.

spin polarization of surface states (SS) and extrinsic spin polarization of photoelectrons due to the photoemission process.

Intrinsic Spin Polarization due to Surface States:

Despite the bulk band structure being spin degenerate, SS can be spin polarized due to the inversion-symmetry-breaking surface. Such SS are predicted along $\overline{\Gamma}$-$\overline{M}_1$ by a DFT calculation (Fig. 4.7 (b)) of a supercell[4] (Krüger, 2016). The energy scale of the calculation is adjusted to the energies found in the experiment[5], i.e. the HVB at $\overline{\Gamma}$ is set to -0.4 eV. Bulk-derived bands (grey lines) are in areas of the surface-projected band structure (depicted by vertical blue bars). Some states,

[4]Consisting of five Se-Re-Se layers.
[5]See following sections.

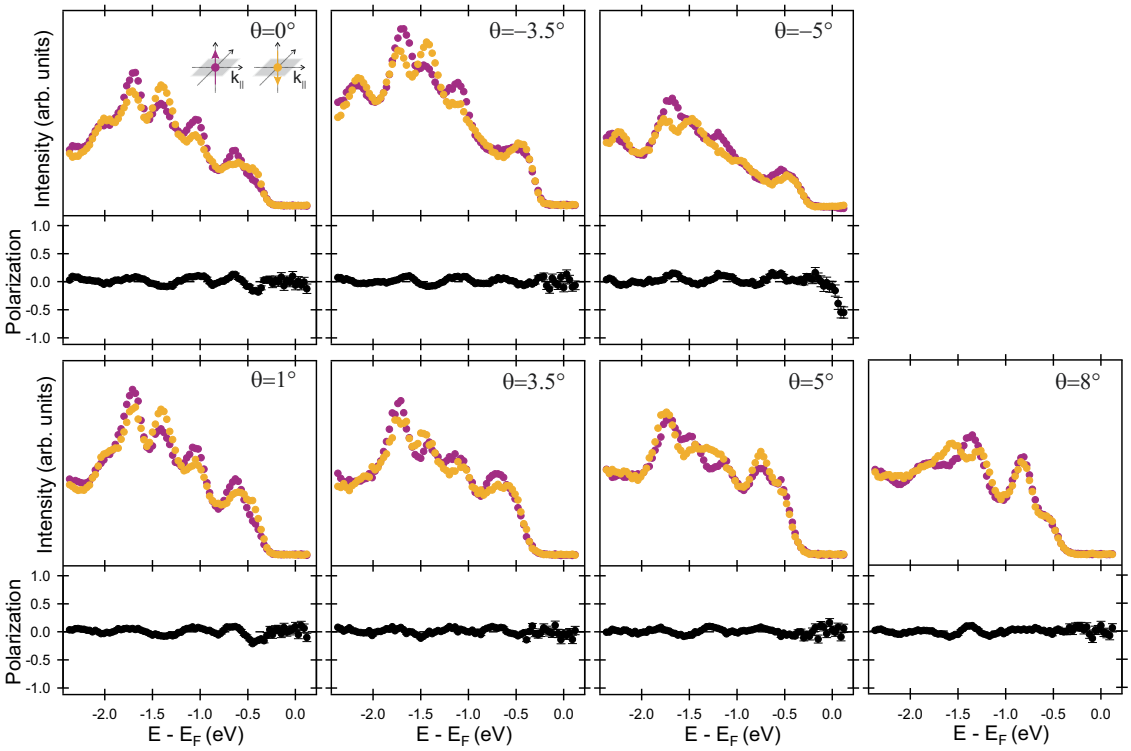

Figure 4.6: SARPES spectra and respective spin polarization P (as defined in section 3.1.2) of $ReSe_2$ with *p*- and *s*-polarized light (hν=21 eV) and sensitivity to the z component (yellow and purple dots) of the spin polarization $\mathbf{P}_z$.

highlighted as green lines, have energies outside the surface-projected bulk bands. These are surface bands.

The expectation value of the spin polarization within the first Se-Re-Se layer for the x (green and cyan points), y (blue and red points) and z (purple and yellow points) component is proportional to the size of the colored points, with values smaller than 0.2 neglected. Importantly, the calculation does not include extrinsic spin-polarization effects. Spin polarization is most pronounced in y and z direction around $\overline{\Gamma}$ at energies of about -0.6 eV, -1 eV, -1.6 eV and -2 eV. It is predominantly corresponding to the highlighted surface bands. Three calculated surface bands with energies of -0.6 eV, -1 eV and -1.6 eV at $\overline{\Gamma}$, are well separated from bulk states. The other surface bands are expected to overlap with bulk bands in the experiment. However, all of the predicted surface bands may contribute to the observed spin polarization in the SARPES experiment.

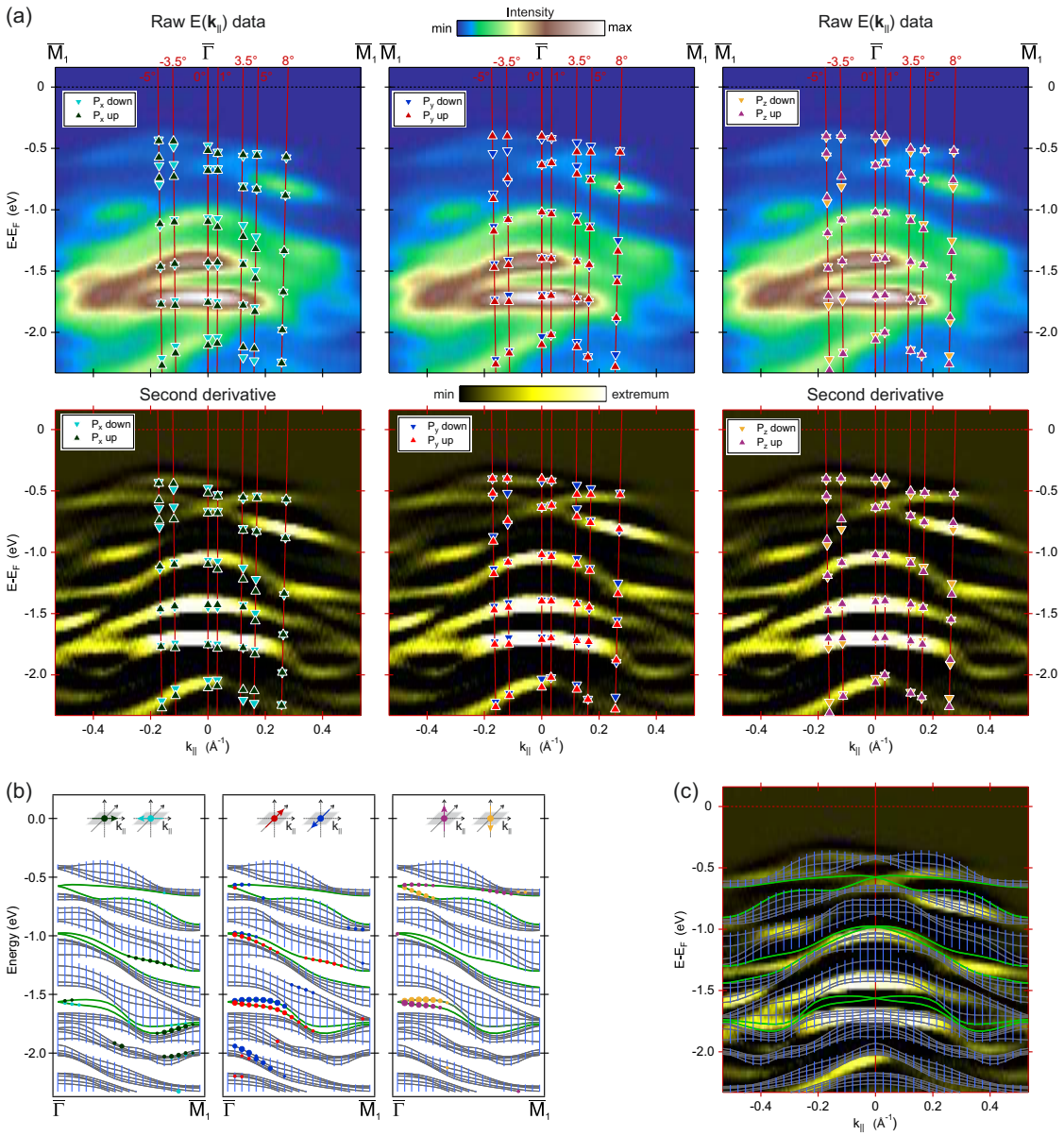

Figure 4.7: (a) ARPES measurement (hν=21 eV, *p*-pol. light) of $ReSe_2$ along $\overline{\Gamma}$-$\overline{M}_1$ together with the corresponding second derivative. Superimposed as colored triangles are the peak positions of the SARPES data for $\mathbf{P}_x$ (Fig. 4.4), $\mathbf{P}_y$ (Fig. 4.5) and $\mathbf{P}_z$ (Fig. 4.6) in the left, middle and right panel, respectively. The red lines correspond to the probed line in **k**-space of the respective SARPES spectrum for the given emission angle θ. (b) DFT calculation (for details see text) along $\overline{\Gamma}$-$\overline{M}_1$ of a supercell consisting of five Se-Re-Se layers. The calculation was performed by P. Krüger (2016). (c) Superposition of the calculation and the second derivative of the ARPES experiment.

In order to identify possible surface bands in the experimental data, the calculation is superimposed on the second derivative of the ARPES data (p-polarized light, hν=21 eV)[6] along $\overline{\Gamma}$-$\overline{M}_1$ in figure 4.7 (c). In the second-derivative representation a multitude of bands are identified, indicating a highly complex electronic structure of $ReSe_2$ that will be discussed in the subsequent sections. Here, the focus is on the existence of possible surface bands.

Most of the predicted surface bands (green lines) can not be clearly observed or distinguished from bulk bands in the experimental data. In general, for higher binding energies, the DFT calculation tends to have less agreement with the experimental data. However, the calculated surface band at about -0.6 eV is indisputably identified in the ARPES results. Therefore, the following discussion is focused on this surface band.

Due to the low symmetry of $ReSe_2$, bulk bands do not have to be symmetric around $\overline{\Gamma}$ (compare discussion in Sec. 4.6). In contrast, surface bands must be symmetric around $\overline{\Gamma}$. As a result, in the ARPES data, the highest (bulk) VB is overlapping with the surface band at approximately $k_{\|}$=0.2 Å^{-1}, whereas for negative $\mathbf{k}_{\|}$ the overlap begins at about $k_{\|}$=-0.3 Å^{-1}. This is also apparent in the peak positions[7] of the SARPES data for $\mathbf{P}_y$ (Fig. 4.5) that are symbolized by the colored triangles in the middle panel of figure 4.7 (a). SAPRES spectra with $\theta = -3.5°$ and $\theta = -5°$ probe the surface band in an area, where it is clearly separated from the HVB. The HVB is found at about -0.40 eV predominantly in the spin up channel (red dots), whereas the surface band is found at -0.52 eV in the spin down channel (blue dots). In the case of the corresponding spectra with positive θ (and $\mathbf{k}_{\|}$) the separation between HVB and the surface band is much smaller. The HVB appears for positive θ (and $\mathbf{k}_{\|}$) predominantly in the spin up channel at -0.45 eV and -0.48 eV for $\theta = 3.5°$ and $\theta = 5°$, respectively. The surface band is found at about -0.53 eV for spin down. In addition, another bulk band[8] is visible in both spin channels at about -0.7 eV, with spin up dominant.

[6] Note that with the given photon energy the cut in $\mathbf{k}$-space is within a plane close to the middle of the bulk BZ, i.e. close to Γ. Details on how to determine the orientation and position in $\mathbf{k}$-space of $ReSe_2$ are given in section 4.4.

[7] Obtained by second derivative analysis.

[8] For negative $\mathbf{k}_{\|}$ this band appears only with weak intensity in the ARPES and SARPES data.

Having identified the surface band in the ARPES and SARPES data, its effect on the observed spin polarization is discussed in the next step. Since the SARPES spectra show only a small spin polarization in x and z direction at energies around -0.5 eV, the discussion is restricted to the strong effects of the $\mathbf{P}_y$ component. When comparing a spectrum with positive θ (and $\mathbf{k}_{||}$) to the corresponding spectrum with negative θ (and $\mathbf{k}_{||}$), the intrinsic spin polarization of the surface band is expected to reverse due to TRS. A sign-reversal of $\mathbf{P}_y$ is observed in figure 4.5 for opposite angles θ. However, for positive angles θ the spin polarization is much larger. Obviously, the intrinsic spin polarization is superimposed by various extrinsic spin-polarization effects that, without further information, impede an indisputable analysis of the intrinsic spin polarization of the surface band. The dominance of extrinsic effects is also indicated by comparing the experimentally observed spin polarization with the predicted intrinsic spin polarization. While $\mathbf{P}_y$ and $\mathbf{P}_z$ are predicted to be similar for the discussed surface band (see Fig. 4.7 (b)), $\mathbf{P}_y$ is much larger in the experiment.

Extrinsic Spin Polarization due to the Geometry of Experimental and Sample:

The $\mathbf{P}_y$ component of the observed spin polarization is much larger than the other components not only at the energies of the SS, but also in a wide range of other energies. In addition, the spin up channel is dominating in the measurements with $\mathbf{P}_y$ sensitivity, whereas for the other spin components no dominant spin channel exists. The described effects can be explained with the geometry of the experiment. The directions of the incoming light and the emitted photoelectrons are in the same plane, the so-called detection plane (xz in Fig. 3.3). The spin-polarization vector of extrinsic effects $\mathbf{P}_E$ has to be perpendicular to the detection plane and more generally to any mirror plane of the system (Jozwiak *et al.*, 2011). Since the x and z components of spin polarization are within the detection plane, only the y component can be non-zero. The yz mirror plane is orthogonal to the detection plane and would suppress the y component. However, the symmetry of the yz mirror plane is broken when using *p*-polarized light, as done in the SARPES experiments with $ReSe_2$. Therefore, the y component of extrinsic spin polarization is observed.

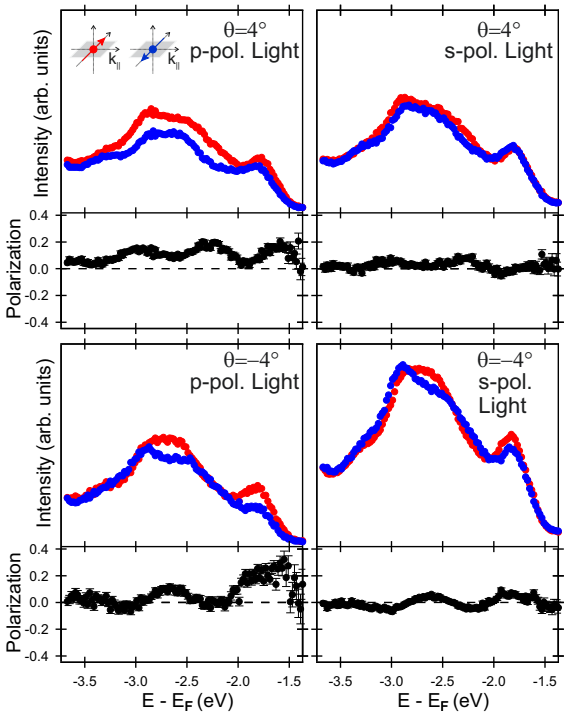

Figure 4.8: SARPES spectra and respective spin polarization P (as defined in section 3.1.2) of ReS_2 with *p*- and *s*-polarized light (hν=21 eV) and sensitivity to the y component (red and blue dots) of the spin polarization $\mathbf{P}_y$.

A further test of the nature of the observed spin polarization was made with *s*-polarized light. *s*-polarized light preserves the yz mirror-plane and impedes the y component of extrinsic spin polarization. Note that the low symmetry of ReS_2 and $ReSe_2$ samples also breaks the yz plane symmetry. Here, in principal spin effects can occur even with *s*-polarized light, yet less pronounced than for *p*-polarized light. SARPES measurements with *p*- and *s*-polarized light are compared for the sister material ReS_2.

Spectra with $\mathbf{P}_y$ sensitivity, for a positive and a negative angle θ, along a non-high-symmetry direction are shown in figure 4.8. Each spectrum was conducted with *p*- and *s*-polarized light of hν=21 eV. For *s*-polarized light, a **k**- and energy-dependent spin polarization with positive and negative values is observed. An additional spin-polarization effect is visible when using *p*-polarized light. Similar to $ReSe_2$, the red spin channel (spin up) dominates independent of the energy for ReS_2 as a result of extrinsic spin-polarization effects.

In summary, $ReSe_2$ shows remarkably high spin polarization of up to 50% without background subtraction, despite having spin-degenerate bulk bands. Due to the low crystal symmetry, spin polarization is observed along x,y and z direction. ARPES and SARPES measurements along $\overline{\Gamma}$-$\overline{M}_1$, consistent with a DFT calculation, indicate the existence of a spin-polarized surface band. However, the majority of the observed spin- polarization effects is caused by the photoemission process. As a result, the obtained polarization of photoelectrons mainly depends on the experimental geometry. Given sufficient working points, this dependence allows to utilize $ReSe_2$ as a photocathode with a spin polarization in the desired direction. To get a further insight in the strong spin effects of $ReSe_2$, one-step model calculations of the photoemission process, including the experimental symmetry, are desired.

4.4 Location of the Valence Band Maximum in the k_z Dependent Electronic Structure

There is an ongoing discussion whether $ReSe_2$ is an indirect or direct semiconductor and where the global VBM is located in **k**-space (Marzik *et al.*, 1984; Huang *et al.*, 1997; Ho *et al.*, 2001; Wolverson *et al.*, 2014; Tongay *et al.*, 2014; Zhao *et al.*, 2015; Arora *et al.*, 2017; Hart *et al.*, 2017). From a theoretical point of view (see Sec. 4.1) DFT-LDA calculations yield an indirect band gap with the CBM at the Ξ-point and the VBM located at Λ. Λ is a point on the $\overline{\Gamma}$-$\overline{M}_1$-line as seen in figure 4.1 (f). In contrast, a *GdW* calculation finds a direct band gap with a VBM at Z (i.e. at $\overline{\Gamma}$).

The position of the VBM is experimentally determined with ARPES. In the case of totally decoupled layers, as predicted by (Tongay *et al.*, 2014), the bands do not depend on k_z and hence not on the photon energy in ARPES. However, as discussed in section 4.1, significant k_z dispersion is expected. Therefore, photon-energy-dependent measurements with energies between hν=118 eV and hν=150 eV and *p*-polarized synchrotron light were conducted. The study is restricted to $\overline{\Gamma}$-$\overline{M}_1$ because all calculations predict the global VBM on this line.

Figure 4.9 (a) shows ARPES results displaying $E(\mathbf{k}_{\parallel})$ dispersions for photon energies between $h\nu = 118\,eV$ and $h\nu = 150\,eV$. Due to the high photon energies, each measurement covers the whole first BZ. In addition, for values of $k_{\parallel}$ larger than $0.53\,Å^{-1}$, the neighboring BZs are probed. It is important to note that a measurement at a certain photon energy creates cuts at different positions of the neighboring BZs for two reasons: (i) the cosine dependence of k_z on the electron emission angle θ (see Eq. 3.5). (ii) The vertical shift of neighboring BZs due to the triclinic structure (see Fig. 4.1). Therefore, the observed electronic structure in the two neighboring BZs can largely differ in measurements for the same photon energy because of the different k_z values. In addition, using p-polarized light, the intensities for positive and negative $k_{\parallel}$ values may be different because the light incidence angle breaks the symmetry of the experiment.

At first, the focus is set on the measurements for $k_{\parallel} = 0$. The corresponding energy distribution curves (EDCs) are shown in figure 4.10 (c) as red linescans. The spectra are fitted with Voigt functions and a linear background. The maxima of the highest bands are marked with green vertical bars. Figure 4.10 (d) shows these maxima at $\overline{\Gamma}$ (red squares) as a function of the photon energy. The fitting procedure is not unambiguous for all photon energies (see spectrum for $h\nu = 126\,eV$). Nevertheless, the band maxima depend clearly on the photon energy, giving evidence of a k_z dependence of the band structure.

For the energy of the highest band at $\overline{\Gamma}$ a minimum (at -0.55 eV) and a maximum (at -0.40 eV) is observed for photon energies of $h\nu = 122\,eV$ and $h\nu = 142\,eV$, respectively (see Fig. 4.10 (d)). Assuming a sinus-shaped k_z dispersion[9], the minimum and maximum of the k_z dispersion are estimated for $h\nu = 119.6\,eV$ and $h\nu = 142.3\,eV$, respectively. Extrema of the energy are expected at high symmetry points. Therefore, the maximum corresponds to either Γ or Z, with the minimum corresponding to the respective other high symmetry point. The assignment of the maximum to a high symmetry point is made by determining the inner potential for both of the possible cases. The energy maximum has to be at the Z point because it is not possible to reach any Γ point at $h\nu = 142.3\,eV$ with a reasonable assumption[10] of V_0. With the Γ (Z) point being reached at a photon energy of $h\nu = 119.6\,eV$ ($h\nu = 142.3\,eV$) it follows $V_0 = 18.5\,eV$. The obtained value for V_0

[9] This shape resembles the predicted k_z dispersion in figure 4.10 (d).

[10] Assuming a Γ-point is reached with $h\nu = 142.3\,eV$ results in a negative value of V_0 or $V_0 \approx 44\,eV$. The former is unphysical while the latter is significantly higher than any reported value of V_0.

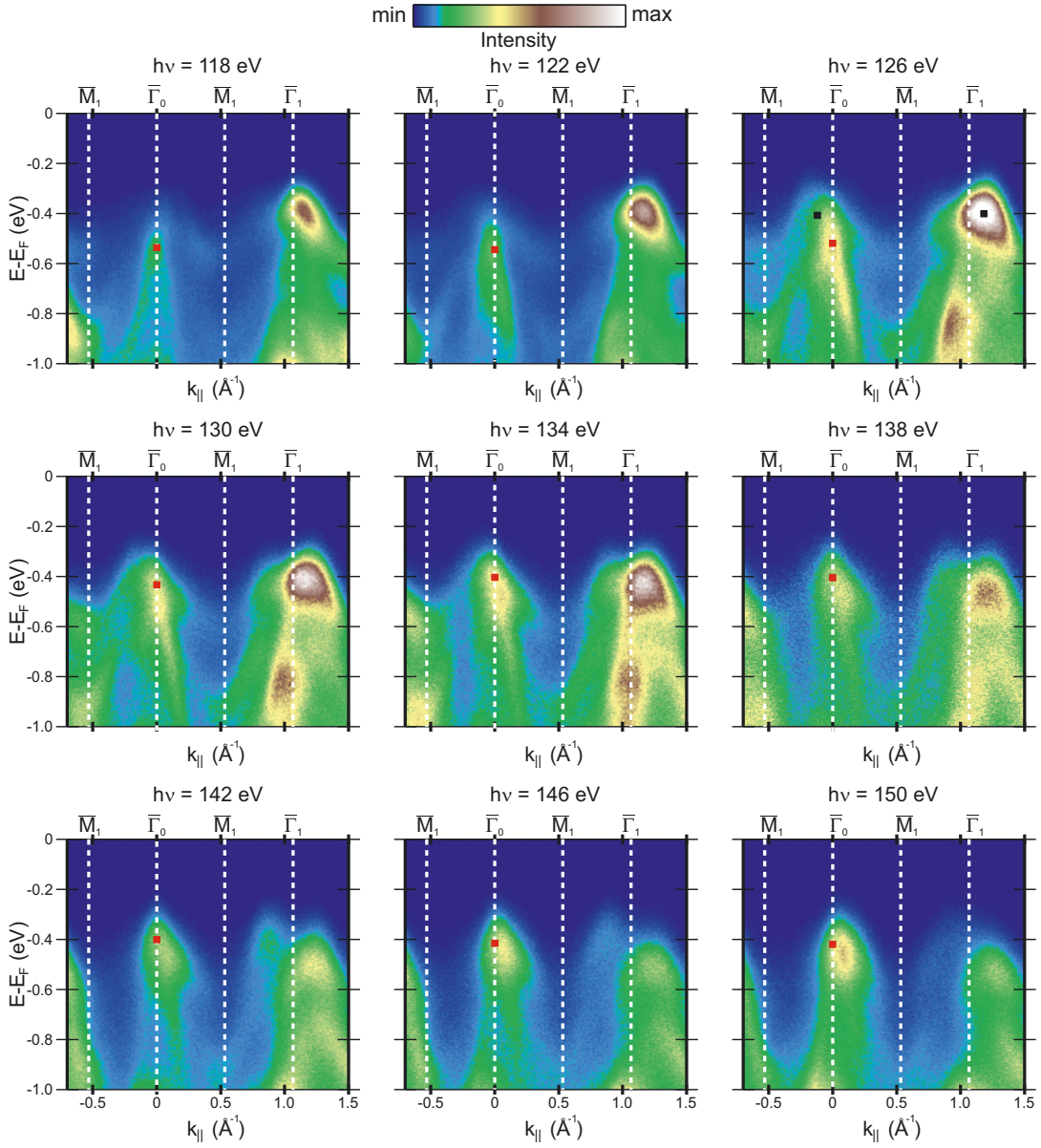

Figure 4.9: (a) ARPES measurements for different photon energies (between hν=118 eV and hν=150 eV) along the $\overline{\Gamma}$-$\overline{M}_1$ direction.

agrees well with a recent study (Hart *et al.*, 2017).

In figure 4.10 (d), in addition, the experimental results are compared with the *GdW*-calculated dispersion along Γ-Z (solid line). A band width of about 155 meV is found in good agreement with the *GdW* calculation. Note that the DFT-LDA

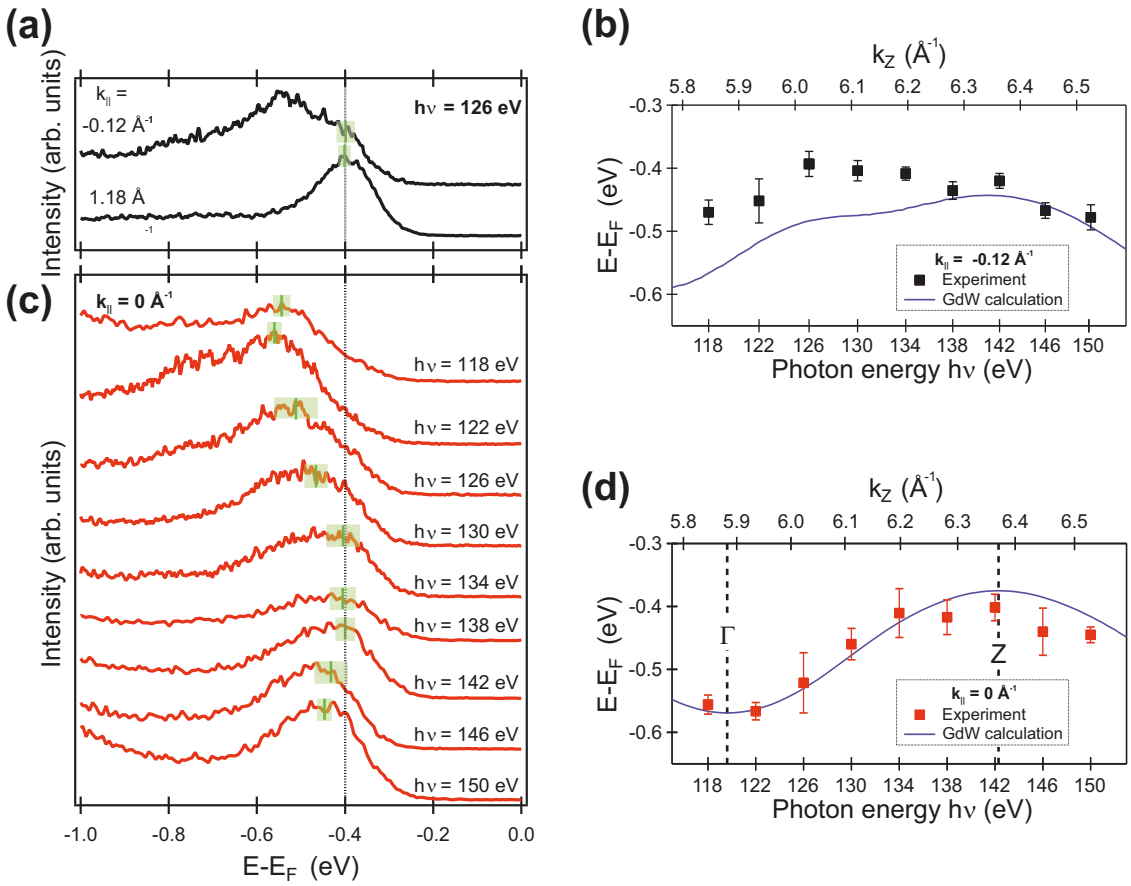

Figure 4.10: (a) and (c): EDCs of ARPES results in figure 4.9 for normal emission (red lines) and for certain points in **k**-space (black lines). The determined positions of the first feature of an EDC are shown as green stripes in (b) and as red and black squares in figure 4.9. (b) and (d) Energy vs k_z dispersion of the HVB for $k_{\|} = 0$ Å^{-1} (i.e. along Γ-Z) and $k_{\|} = -0.12\,\text{Å}^{-1}$. The k_z values are calculated using the final state free electron model with an inner potential of $V_0 = 18.5$ eV. The solid line is the calculated dispersion using *GdW* theory.

calculation yields a band width of only 50 meV, far below the experimental value. Thus, quasiparticle calculations result in a more precise description of the band structure in this case.

In a second step, the results for non-normal electron emission are discussed. Clear band maxima away from BZ centers are observed in figure 4.9. For example, for photon energies below $h\nu = 138$ eV, a maximum for $k_{\|} < 0\,\text{Å}^{-1}$ ($k_{\|} < \Gamma_0$) is observed. This maximum becomes centered at Γ_0 for about 140 eV. For $h\nu > 146$ eV, the maximum appears for positive values of $k_{\|}$. This behaviour is reproduced by

the *GdW* calculation. With increasing k_z, the calculation predicts the local VBM first at negative $k_{||}$ values. Then it appears at $k_{||} = 0\,\text{Å}^{-1}$ when approaching the Z point, where the global VBM is located in the calculation. When entering the next BZ, the local VBM is then located at values of $k_{||} > 0\,\text{Å}^{-1}$. An analogous behavior is found around the center of the second BZ.

Figure 4.10 (a) shows two EDCs taken at a photon energy of $h\nu = 126\,\text{eV}$, exemplary for band maxima at off-normal electron emission. Using the same fitting procedure as above, energies of -0.4 eV are obtained, indicated by green vertical bars. In addition, the energy values are shown as black squares in figure 4.9. Figure 4.10 (b) shows the band maxima as in figure 4.9 (d) but for off-normal electron emission at $k_{||} = -0.12\ \text{Å}^{-1}$ in comparison with the band maxima obtained from the GdW calculations. The wave-like photon-energy dependence in figure 4.10 (d) with a minimum at Γ and a maximum at Z changes into a two-peak structure with a new local maximum around $k_z = 6\ \text{Å}^{-1}$ and a reduced maximum between $k_z = 6.3\ \text{Å}^{-1}$ and $k_z = 6.4\ \text{Å}^{-1}$. While there is qualitative agreement between theory and experiment, the new maximum in experiment appears at lower energy as a saddle point in theory. The local maximum in the experimental data competes now with the band maximum at Z (see Fig. 4.10) within an estimated uncertainty of about 50 meV. The same analysis (not shown) of the band maxima for off-normal electron emission in the second BZ at $k_{||} = 1.18\ \text{Å}^{-1}$, obtaining the same results of a local maximum at a position in the second BZ equivalent to $k_z = 6\ \text{Å}^{-1}$ in the first BZ.

In summary, on the basis of the experimental data, it is not clear within experimental limits, whether the global VBM is at the above-described non high-symmetry point in **k**-space or at the Z point. The overall agreement between experiment and GdW theory is very good, i.e. within several tens of meV. A small quantitative deviation, however, remains about the absolute location of the VBM. With such a small energy difference between different local maxima of the VB, the controversial discussion in the literature about the type of the band gap in bulk $ReSe_2$ is comprehensible (Marzik *et al.*, 1984; Ho *et al.*, 2001; Ho and Huang, 2004; Wolverson *et al.*, 2014; Zhao *et al.*, 2015; Arora *et al.*, 2017; Hart *et al.*, 2017).

4.5 Unoccupied Electronic Structure and Band Gap of $ReSe_2$

The controversial discussion about the band gap, mentioned in the previous section, focuses mainly on the occupied part of the electronic structure, especially on the position of the VBM in **k**-space. The knowledge about the unoccupied electronic structure, relies only on calculations, since no **k**-resolved experimental study has been conducted so far. Of particular interest are the properties of the LCB and the fundamental electronic band gap. In this section, (SR)IPE is used to shed light on the unoccupied electronic structure of bulk $ReSe_2$. Combining these results with the ARPES data gives information about the size and type of the fundamental electronic band gap. A comparison of the determined band gap with data for the corresponding optical band gap allows to determine the exciton binding energy and gives insights into the physics of excitons in $ReSe_2$.

All (SR)IPE measurements are conducted at room temperature with the photon detector C2 (depicted in figure 3.2). Light with a photon detection energy of $h\nu$= 9.9 eV is detected without polarization analysis in (SR)IPE. Spin-resolved IPE measurements (see appendix A.2) show, in contrast to the SARPES results presented in section 4.3, no significant spin polarization with $\mathbf{P}_y$ (Rashba) spin sensitivity[11]. Due to the lack of spin effects the focus is set on spin-integrated measurements.

Figure 4.11 shows spin-integrated IPE data for several angle of electron incidence θ along several directions. Two broad features of varying shape are observed in all spectra. A multitude of bands contribute to these features. Spectra at the same angle θ along different directions are highlighted with the same colors. The spectra are different depending on the measured direction, reflecting the expected in-plane anisotropy. However, the broad features do not allow a more detailed analysis. Instead, the in-plane anisotropy and the connection to the real space structure of $ReSe_2$ will be discussed in the next section on the basis of ARPES data.

[11] This is despite the fact that for the CBs and VBs a similar amount of spin polarization is predicted in the calculations, as seen in figures 4.12 and 4.7.

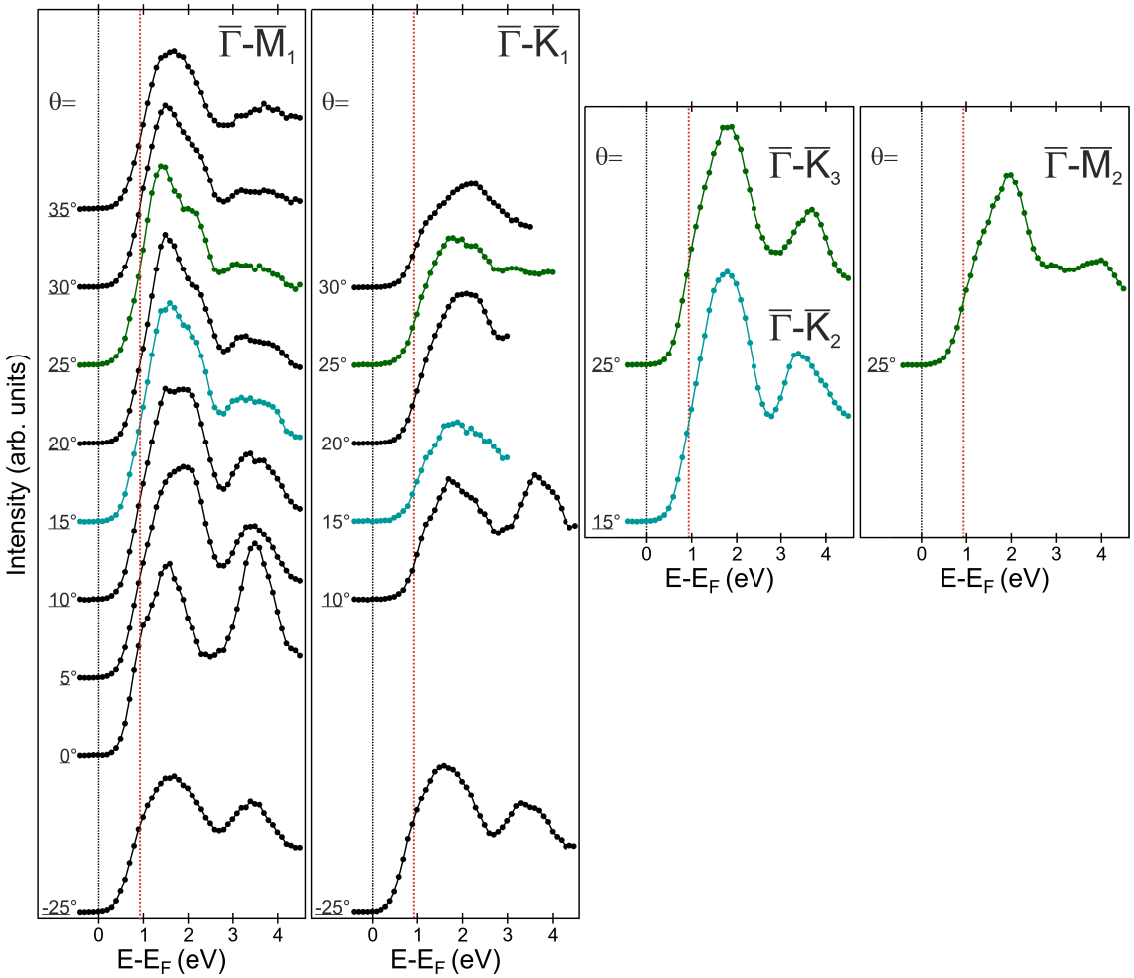

Figure 4.11: Spin-integrated IPE spectra of $ReSe_2$ along different directions. The color of the dots denote spectra with the same angle θ, taken at different directions. The red dashed line indicates the energy of the lowest-energy feature of the spectrum with $\theta = 0°$. Underlined angles θ highlight spectra that are part of the angle-integrated IPE data shown in figure 4.13. Spectra are normalized to the absorbed charge during the IPE experiment.

A $k_{\|}$-dependent dispersion is evident as the shape of the broad features is changing as a function of θ. Due to the overlapping bands, the exact position of these bands can not be determined precisely. Nonetheless, the data allow a few conclusions about the CBs. In order to compare experimental data along $\overline{\Gamma}$-$\overline{M}_1$ with the surface-projected calculated bands, the intensity of experimental data is plotted against $k_{\|}$ in an contour plot in figure 4.12. Each color-coded stripe in the figure corresponds to an IPE spectrum. High intensity appears as brown to white

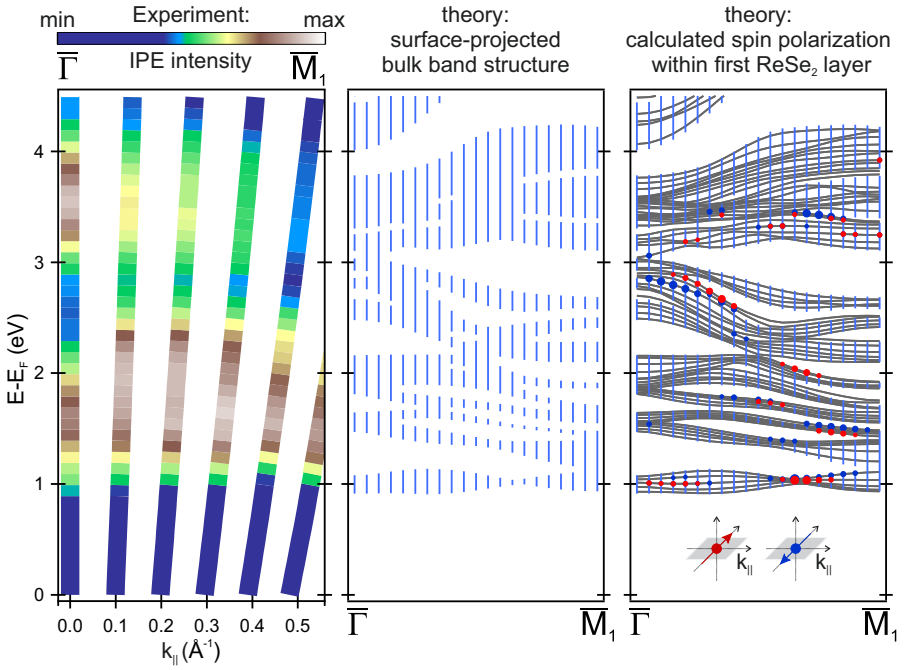

Figure 4.12: Left panel: intensity plot of the IPE data along $\overline{\Gamma}$-$\overline{M}_1$. Middle and right panel: the surface-projected bulk band structure of $ReSe_2$ along $\overline{\Gamma}$-$\overline{M}_1$ is presented as blue vertical bars. Right panel: DFT calculation of a supercell consisting of five Se-Re-Se layer. Grey lines represent calculated bands of the five-layer slab. In order to compare experimental data with the calculation, the calculated lowest CB at $\overline{\Gamma}$ is set to 0.93 eV. This is the lowest energy of a feature found in the spectrum for $\overline{\Gamma}$. The calculated spin polarization of the topmost Se-Re-Se layer is depicted in the right panel as red and blue dots for the $\mathbf{P}_y$ (Rashba) component. The calculations were performed by P. Krüger (2016).

color in the image representation, whereas low intensity in the spectra is depicted with green to blue colors. The width of the stripes indicates the **k**-resolution of the IPE experiment. The presentation is analogous to the contour-plots of ARPES data in this chapter. In the case of the IPE data, spectra have been conducted in steps of $\Delta\theta = 5°$. As a result, not the whole **k**-space is covered with experimental data.

Above the fundamental band gap two regions of low intensity, i.e. regions without bands, are observed. (i) Around $\overline{\Gamma}$ at energies between 2 eV and 3 eV. (ii) At $k_{||} > 0.3$ Å^{-1} for energies around 3 eV. The middle panel of figure 4.12 shows the calculated surface-projected bulk bands[12]. Gaps corresponding to (i) and (ii) are predicted by the calculation. A DFT calculation of a supercell consisting of

[12]The energy scale of this calculation is adjusted to the energy of the first feature found in the experiment, i.e. the calculated lowest CB at $\overline{\Gamma}$ is set to 0.93 eV above E_F.

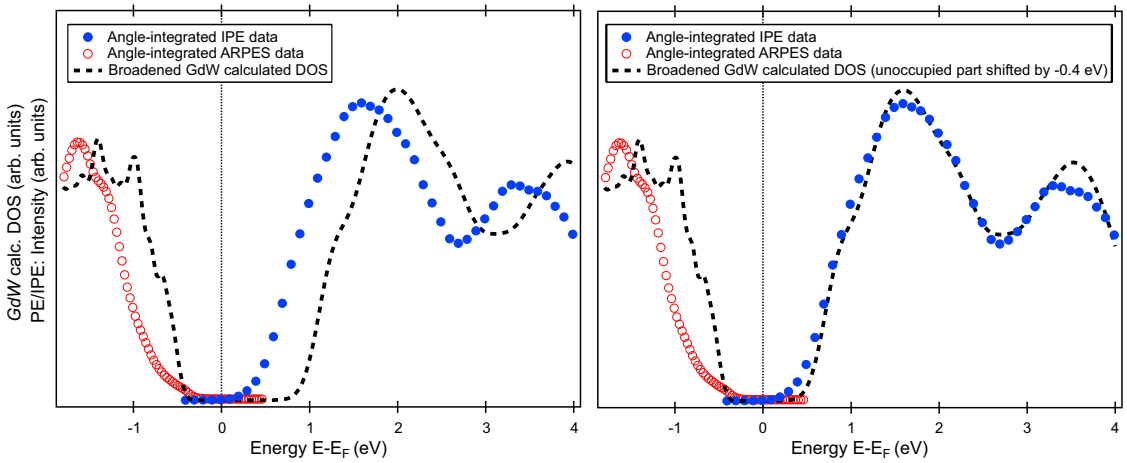

Figure 4.13: Comparison of *GdW* calculated DOS and angle-integrated ARPES and IPE data. The occupied (unoccucpied) calculated DOS is artificially broadened by a Gaussian function with 70 meV FWHM (630 meV FWHM). In the right panel, the calculated unoccupied DOS is shifted by 0.4 eV to lower energy resulting in remarkably good qualitative agreement with the angle-integrated IPE data (discussion see text).

five Se-Re-Se slabs (more details in Sec. 4.3) is presented in the right panel. Alike within the occupied electronic structure, surface-related bands are predicted, e.g. halfway along $\overline{\Gamma}$-$\overline{M}_1$ at about 2.5 eV. However, these bands are not strongly separated in energy from bulk bands and not present in the areas of (i) and (ii). In summary, the IPE data shows several bands separated by gaps. The multitude of bands impede more detailed conclusions.

Of particular importance are the position and energy of the CBM. Two approaches to gain information about the position and the size of the CBM have been made.

(i) The lowest-energy feature of the spectra is a shoulder at $E_{CBM,\overline{\Gamma}} = 0.93\,eV$ (determined by second derivative) that can clearly be seen in the spectrum for $\overline{\Gamma}$ ($\theta = 0°$) in figure 4.11. The red dashed line indicates its position in energy. The shoulder is not as pronounced visible in any other spectra. Considering the results about the VBM in the previous section, a band gap of $E_{Gap,\overline{\Gamma}} = 1.33$ at $\overline{\Gamma}$ is deduced. Since not the whole BZ was covered in the IPE data, it is not clear whether $E_{Gap,\overline{\Gamma}}$ is the fundamental band gap.

(ii) To obtain the size of the fundamental band gap, another approach is tried. The band gap of the *GdW*-calculated density of states (DOS) is corrected in a way that the resulting calculated DOS fits to the angle- and photon energy-integrated experimental data. This corrected band gap of the calculated DOS is an estimation of the actual fundamental band gap. Figure 4.13 shows the angle- and photon energy-integrated experimental data in comparison to the calculated DOS without and with adjusted band gap.

The ARPES data are shown as red dots. In ARPES, data of the whole SBZ exist for two different photon energies hν: 21 eV and 63 eV. ARPES measurements with 21 eV and 63 eV photon energies result in a k_z that is close to the k_z of Γ and Z, respectively. The angle-integrated ARPES data contain both of the possible VBMs at -0.4 eV that have been determined in the previous section.

The IPE data are shown as blue dots. In IPE, spectra with the same energy range were added up. These spectra are highlighted in figure 4.11 by underlined angles θ. The angle-integrated IPE spectra mainly represent the $\overline{\Gamma}$-$\overline{M}_1$ direction. Considering the photon detection energy, the IPE spectra probe in vicinity of the Z point. This means that only a small part of the bulk BZ is covered by the angle-integrated IPE data. However, the onset of the DOS can potentially be observed in IPE due to indirect transitions (compare discussion in Ch. 5).

The *GdW*-calculated DOS is represented by the dashed line in figure 4.13. The calculated HVB is set to an energy of -0.4 eV as found in the ARPES data. Furthermore, the calculated DOS has been broadened by convolution with a Gaussian function of 70 meV FWHM and 630 meV FWHM for the occupied and unoccupied DOS, respectively. The broadening does not only reflect the energy resolution of the experiment but also additional broadening due to faceting of the sample surface as discussed in Sec. 4.2. The calculated band gap for T=0 K is $E_{Gap,GdW} = 1.49$ eV.

The angle-integrated experimental data does not only depend on the DOS, but it is also crucially influenced by transition matrix elements. This is particularly pronounced in the case of the ARPES data, since polarized light has been used. Surprisingly the angle-integrated IPE data are extremely

Table 4.1: Experimentally determined electronic band gaps (EBG) and optical band gaps (OBG) of bulk $ReSe_2$. The EBG has been determined as the energy of the absorption edge in optical absorption (OA) experiments. In addition to OA, photoluminescence spectroscopy (PL) is used to determine optical properties.

Method	Temp.	EBG size	EBG type	OBG size	Source
see (i)	150 K/300 K	1.33 eV	direct		present work
see (ii)	150 K/300 K	1.09 eV	unclear		present work
OA	300 K	1.17 eV	indirect		(Marzik *et al.*, 1984)
OA	300 K	1.18 eV	indirect	1.305 eV	(Ho *et al.*, 2001)
ARPES	100 K	>1.40 eV	unclear		(Hart *et al.*, 2017)
PL	80 K			1.26 eV	(Zhao *et al.*, 2015)
OA	25 K	1.35 eV	indirect	1.387 eV	(Ho *et al.*, 2001)
OA,PL	10 K			1.37 eV	(Arora *et al.*, 2017)

similar to the calculated DOS, with both having two broad features. Apparently there is an energy shift between unoccupied experimental data and calculated DOS. Correcting this shift of about 0.4 eV, as done in the right panel of figure 4.11, results in a remarkable agreement of unoccupied experimental data and DOS. As a result, the size of the band gap is estimated as $E_{Gap,(ii)} = 1.09$ eV.

The results of (i) and (ii) are summarized in table 4.1 along with experimentally determined values from the literature for several sample temperatures. Note that the electronic band gap of semiconductors becomes smaller when increasing the temperature due to increased lattice length and electron-phonon interaction. In the presence of excitons, the electronic direct band gap has to be larger than the corresponding optical band gap. The band gap $E_{Gap,\bar{\Gamma}} = 1.33$, obtained by analysis (i), is larger than values of Ho *et al.* (2001) (1.305 eV) and Zhao *et al.* (2015) (1.26 eV) reported for the optical band gap at T = 300 K and T= 80 K, respectively. Considering the value of Zhao *et al.* (2015) and $E_{Gap,\bar{\Gamma}}$, this leads to an estimated exciton binding energy of $E_{ReSe_2,exc,b} = 0.07$ eV. However, this value should be seen as a rough estimate, since different sample temperatures were used in the study of Zhao *et al.* (2015) and the present work. Nonetheless, $E_{ReSe_2,exc,b}$ is in the same order of magnitude as the value of 0.12 eV reported in Arora *et al.* (2017).

The band gap size obtained by analysis (ii) is $E_{Gap,(ii)} = 1.09$ eV. Even though $E_{Gap,(ii)}$ is just a rough estimate, its value is clearly lower than any reported optical band gap and the *GdW*-calculated band gap. It is also way below $E_{Gap,\overline{\Gamma}}$ and the estimated gap size by Hart *et al.* (2017) of larger than 1.40 eV. However, $E_{Gap,(ii)}$ agrees with the results of other studies. It is in the order of presumably indirect band gaps that are determined as absorption edge energy in optical absorption experiments (see Tab. 4.1). Given the results of analysis (i) and (ii), the discussion about the band gap due to the different results in previous studies is not surprising.

Interestingly, the same discussion about the band gap arises in the case of the sister material ReS_2. Biswas *et al.* (2017) found the band gap of a ReS_2 to be 0.3 eV lower than the optical band gap[13].

In summary, the unoccupied electronic structure of bulk $ReSe_2$ has been studied by IPE. The spectra consist of two broad features with clear $\mathbf{k}_{\parallel}$-dependence. These features are composed of several overlapping bands. Regions without bands in the unoccupied electronic structure are identified consistently to the calculation. The band gap at $\overline{\Gamma}$ (presumably at the Z point) is found to be $E_{Gap,\overline{\Gamma}} = 1.33$ eV. Using the calculated DOS and angle-integrated experimental data, a much lower fundamental band gap size of $E_{Gap,(ii)} = 1.09$ eV is estimated. This size is consistent to some experimentally determined values found in the literature but contradicting to other experimental and theoretical studies. The electronic structure has an in-plane anisotropic character, as indicated by comparing IPE spectra along different high symmetry directions. This will be further discussed on the basis of ARPES results in the subsequent section.

[13] Biswas *et al.* (2017) evaporated Rb atoms on ReS_2 that result in surface-doping and, as a consequence, occupation of the LCB. They then determined the band gap with ARPES. Note that surface-doping may create a near-surface downward band bending. However, an increased band gap is expected in this case.

4.6 In-plane Anisotropy of $ReSe_2$

The structural anisotropy of the triclinic $ReSe_2$ is reflected in many anisotropic optical, electric, and optoelectronic properties as reported in the literature (Tiong *et al.*, 1999; Ho *et al.*, 2001; Ho and Huang, 2004; Zhang *et al.*, 2016; Arora *et al.*, 2017). To understand these properties, the band structure is examined in different directions in **k**-space by means of ARPES. Figure 4.14 shows ARPES measurements along the different $\overline{\Gamma}$-$\overline{M}$ and $\overline{\Gamma}$-$\overline{K}$ directions for *p*-polarized light with a photon energy of $h\nu = 63$ eV. The experiments were conducted at BL-9B of HiSOR. Measuring with a certain photon energy, i.e. k_z value, means probing a certain cut within the bulk BZ. Importantly, inversion symmetry within cuts probed in **k**-space are not expected for photon energies, where neither the Γ nor the Z point is reached. Here, for $h\nu = 63$ eV, the distance from the Z point is about 0.04 $Å^{-1}$. This is also reflected in the calculated *GdW* band structure (red lines in Fig. 4.14) which includes the k_z dependence: the bands are not symmetric with respect to $\overline{\Gamma}$.

Comparing the different E vs $\mathbf{k}_{\parallel}$ dispersions in Fig. 4.14, the $\overline{\Gamma}$-$\overline{M}_1$ direction stands out with the smallest band width of the HVB. To identify the other $\overline{\Gamma}$-$\overline{M}$ and $\overline{\Gamma}$-$\overline{K}$ directions, one has to consider two possible orientations of the BZ due to crystal symmetry. To choose the correct orientation, the geometry of the experiment is considered and the information about k_z (see details in Sec. 4.4) is used. In the ARPES measurement with a photon energy of $h\nu = 142$ eV (see Fig. 4.9 (a)) a local maximum appears at 0.87 $Å^{-1}$ in the second BZ. This observation is only consistent with the chosen orientation of the BZ (see Fig. 4.2). Thus, the various directions within the SBZ are indisputably determined.

Several bands are found within 1.5 eV below the Fermi level. However, unlike the result for $h\nu = 21$ eV shown in figure 4.7, not all bands can be distinguished. The calculated *GdW* band structure $E(\mathbf{k}_{\parallel}, k_z)$, with the respective k_z determined for the used photon energy (see Eickholt *et al.* (2018a)) is superimposed as red lines. The experiment is in a good agreement with the calculated bands. Two bands are clearly identified, the HVB at -0.4 eV and a band at -1.4 eV (at $\overline{\Gamma}$), which appears as an intense spectral feature. Spectral intensity between -0.8 eV and -1.4 eV is attributed to three additional bands, predicted from theory.

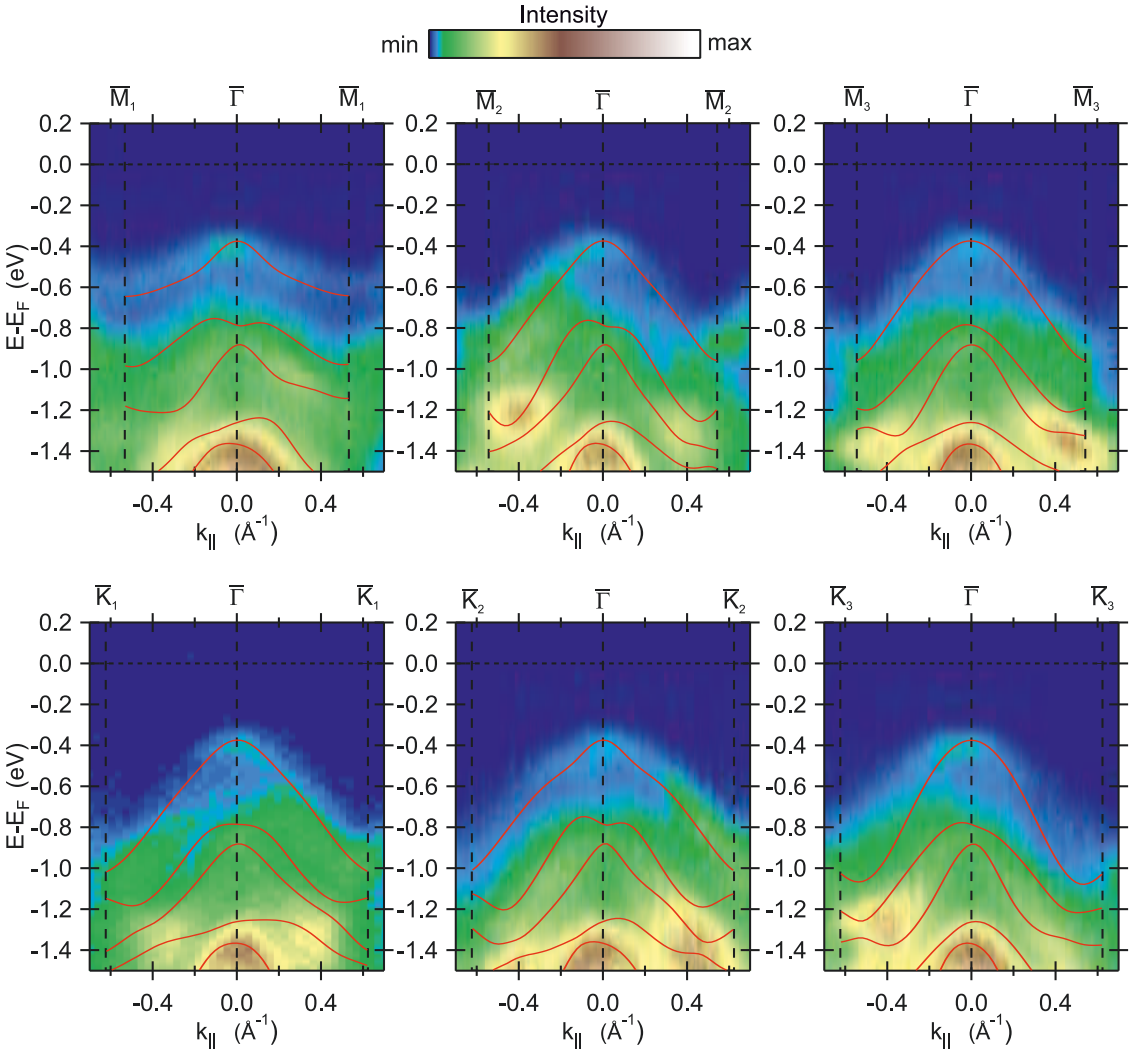

Figure 4.14: ARPES measurements (hν=63 eV) along high-symmetry directions of the SBZ shown in Fig. 4.1. The calculated *GdW* band structure $E(\mathbf{k}_{||}, k_z)$, with the respective k_z determined for the used photon energy, as described in Eickholt *et al.* (2018a), is superimposed in red.

In the ARPES measurements, a broadening of the bands is observed which is larger than the experimental energy resolution of about 60 meV. This may be due to the fact that the synchrotron light spot is larger than the average crystallite size of the sample. As a consequence, the ARPES measurements average over more than one crystallite with possible slight misalignment of the contributing crystallites. Even a misalignment of one degree leads to significant broadening (see Sec. 4.2). A further reason for broadening might be electron-defect as well as

electron-electron interaction. For increasing binding energies the latter results in decreasing lifetimes of the states. Consequently, an increased lifetime broadening occurs for high binding energies.

The maximum of the highest band appears at $E - E_F = -0.4\,eV$ consistent with the results in section 4.4. With the band gap taken into account that was discussed in the previous section, this means the sample is slightly p-doped. In a recent study, samples from another company showed considerable n-doping with the highest band appearing at $E - E_F = -1.4\,eV$ (Hart *et al.*, 2017).

Most important for the optoelectronic properties of $ReSe_2$ is the anisotropic HVB. The ARPES measurements show, in excellent agreement with the *GdW* calculation, that the $\overline{\Gamma}$-$\overline{M}_1$ direction is a distinctive direction within the SBZ, which shows significantly flatter band dispersion than any other direction. Concerning the other five directions, there are only small differences. The *GdW* calculation reveals a slightly steeper dispersion along $\overline{\Gamma}$-$\overline{K}_3$ which is not observed in the experiment due to the broadening of the bands. Note that ARPES data of the sister material ReS_2 (see Fig. A.2) also show a distinctive direction within the SBZ which exhibit a flat band dispersion of the HVB.

The distinct role of $\overline{\Gamma}$-$\overline{M}_1$ and $\overline{\Gamma}$-$\overline{K}_3$ directions can be understood on the basis of the "diamond chains" formed by parallelogram-shaped clusters of Re atoms along the $a-$axis of $ReSe_2$. The shortest distance between two Re atoms of adjacent clusters is 2.95 Å along the chain while it amounts to 3.95 Å perpendicular to the chain. In a simple picture, the stronger Re-Re interaction along the chain gives rise to a larger dispersion and a concomitantly larger band width in $\overline{\Gamma}$-$\overline{K}_3$ direction (parallel to the chains) with respect to the $\overline{\Gamma}$-$\overline{M}_1$ direction (perpendicular to the chains).

4.7 Conclusion

The electronic structure of anisotropic bulk $ReSe_2$ was studied with (S)ARPES and (SR)IPE. SARPES measurements showed a remarkably high spin polarization of photoelectrons of up to 50% without background subtraction. Due to the low symmetry of $ReSe_2$, spin polarization is observed along x,y and z directions. ARPES and SARPES measurements along $\overline{\Gamma}$-$\overline{M}_1$, consistently with a DFT calculation, indicate the existence of a spin-polarized surface band. However, the majority of the observed spin-polarization effects are caused by the photoemission process.

Photon-energy-dependent measurements reveal a k_z-dependent band dispersion in agreement with the *GdW* calculation, reflecting the interlayer coupling. Two valence-band maxima with indistinguishable energy are experimentally identified. One of them is located at the Z point, where the *GdW* calculation predicts the direct band gap. The other VBM appears at a non high-symmetry point in **k**-space along $\overline{\Gamma}$-$\overline{M}_1$. The IPE study provides first **k**-resolved experimental information on the in-plane anisotropic CBs. The band gap at $\overline{\Gamma}$ is determined to $E_{Gap,\overline{\Gamma}} = 1.33$ eV. A comparison between the calculated DOS and angle-integrated experimental data indicates the fundamental band gap size to be lower than $E_{Gap,\overline{\Gamma}}$.

An anisotropic E vs $\mathbf{k}_{\parallel}$ dispersion of the VBs is observed, with the direction perpendicular to the "diamond chains", i.e. $\overline{\Gamma}$-$\overline{M}_1$, being a distinct direction in **k**-space with the smallest band width of the HVB.

5

Electronic and Spin Structure of WS_2*

W- and Mo-based TMDCs are known for their indirect-to-direct band-gap transition upon reducing the thickness to a single layer (SL) (Mak *et al.*, 2010; Cheiwchanchamnangij and Lambrecht, 2012; Jin *et al.*, 2013; Cappelluti *et al.*, 2013; Zhang *et al.*, 2014a; Yeh *et al.*, 2015). Since the SL material has no inversion symmetry, the Kramers degeneracy is lifted which causes spin-dependent band splittings due to spin-orbit interaction. The spin texture with alternating spin orientations at the $\overline{\mathrm{K}}$ and $\overline{\mathrm{K}}'$ high-symmetry points leads to coupled spin and valley physics and possible applications (Xiao *et al.*, 2012).

The VBs of SL W- and Mo-based TMDCs have been studied in detail with photoemission techniques (Klein *et al.*, 2001; Zhang *et al.*, 2014b; Dendzik *et al.*, 2015; Miwa *et al.*, 2015; Grubisic Cabo *et al.*, 2015; Le *et al.*, 2015; Zhang *et al.*, 2016; Bruix *et al.*, 2016; Ulstrup *et al.*, 2016a; Mo *et al.*, 2016). The detection of two different excitons A and B in optical experiments (Mak *et al.*, 2010) is explained by the spin-dependent energy splitting of the VB. So far, experimental information about the unoccupied CBs is limited to scanning tunneling spectroscopy (Zhang *et al.*, 2015; Bruix *et al.*, 2016) and time-resolved photoemission data (Grubisic Cabo *et al.*, 2015; Ulstrup *et al.*, 2016b, 2017) yet without spin resolution. Since the CBs are also predicted to have a spin-dependent energy splitting (Zhu *et al.*, 2011;

* Figures and text excerpts of this chapter have been published in (Eickholt *et al.*, 2018b). Reprinted with permission from (Eickholt *et al.*, 2018b). Copyright (2018) by the American Physical Society.

Kosmider *et al.*, 2013; Liu *et al.*, 2013; Kormányos *et al.*, 2015), spin-allowed and spin-forbidden (”dark”) transitions are expected. This leads to so-called dark excitons which possibly influence the efficiency of SL TMDC devices (Ye *et al.*, 2015; Echeverry *et al.*, 2016).

In this chapter, a combined (S)ARPES and (SR)IPE setup is used to investigate the spin-dependent occupied and unoccupied electronic structure of SL WS_2. In section 5.1 requirements of the sample, necessary for spin-dependent measurements, are discussed. Section 5.1.1 shows how SL WS_2 is grown on Au(111) and characterized. Bulk samples used for comparison are characterized in section 5.1.2. Subsequently, the main results about the spin-dependent electronic structure are shown in section 5.2. The spin-dependent unoccupied electronic structure of SL WS_2 on Au(111) measured with SRIPE is presented and discussed along with band structure calculations in section 5.2.1. In section 5.2.2, comparative measurements of bulk and SL WS_2 indicate the influence of the Au(111) substrate on the SL WS_2 electronic structure. The influence turns out to be negligible for the lowest CB at K. Finally the spin structure of the K valleys is revealed by the combined use of SRIPE and SARPES in section 5.2.3.

5.1 Samples: Requirements and Characterization

Surface science relies on samples with a defined surface that is as close as possible to the ”ideal” surface used for models and calculations. This means the samples must have a periodic crystal structure with as few as possible structural and chemical defects such as vacancies and impurities. To achieve such an ”ideal” sample it has to be produced or cleaned *in situ* in UHV.

Moreover, **k**-resolving methods such as (S)ARPES and (SR)IPE require single crystals, a single orientation of crystallites or at least only equivalent orientations of crystallites within a sample. While for some methods such as STM small sample sizes within tens of nm are sufficient, conventional[1] (S)ARPES and (SR)IPE require sample sizes up to the mm range. Since charged particles are involved, it is important to prevent sample charging during measurements, which becomes

[1] Recently ”nano-ARPES” experiments with a spatial resolution up to several μm (Katoch *et al.*, 2018; Cattelan and Fox, 2018) have been developed.

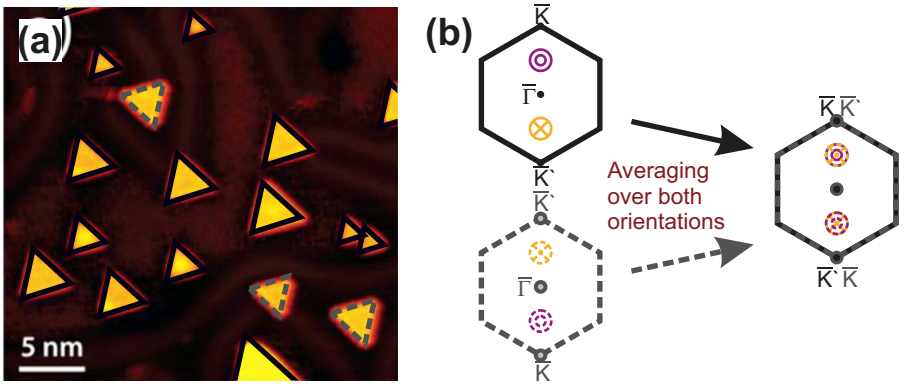

Figure 5.1: (a) STM image showing the typical growth of mirror domain SL TMDCs on Au(111) on the example of MoS_2/Au(111). Adapted from Bruix *et al.* (2015). (b) Experiments averaging over both orientations lead to a mixing of $\overline{\mathrm{K}}$ and $\overline{\mathrm{K}}'$ points and, as a result, measure reduced out-of-plane spin polarization.

important for non-metallic samples. Suitable samples for the SARPES and SRIPE experiment in this thesis therefore need to fulfill three requirements:

(a) Single orientation of periodically structured crystallites,

(b) sample sizes larger than a mm,

(c) sufficient conductivity to prevent charging during experiments.

In the following it will be described how samples fulfilling (a), (b) and (c) are prepared. In addition, characterization measurements testing the desired properties will be shown. Section 5.1.1 focuses on SL WS_2 samples that are grown on a Au(111) substrate. Bulk WS_2 is characterized in section 5.1.2.

5.1.1 Growth Process and Characterization of SL WS_2 on Au(111)

While much of the hype about TMDCs is a result of the easy production of a SL by micromechanical exfoliation, this method is not suitable for conventional (S)ARPES and (SR)IPE because it creates much smaller SL flakes than the area probed by these techniques. These small flakes are not all aligned in a precisely single orientation and, as a result, impede **k**-resolved measurements. In addition, a significant amount of bi- and multilayers can occur. Alternative ways to

produce SL TMDCs are chemical vapor deposition or physical vapor deposition. The latter allows to precisely grow ultra thin films epitaxially, e.g. by molecular beam epitaxy. It was used by Grønborg *et al.* (2015) to synthesize large areas of SL MoS_2 on Au(111) that could be studied with ARPES. As a side note, the metallic substrate has the advantage to eliminate any possible charging effect in ARPES.

The synthesis method can also be used to grow other SL TMDCs on the (111) surface of noble metals such as Au and Ag. An ARPES study of SL WS_2 grown on Au(111) has been performed (Dendzik *et al.*, 2015). However, it turns out that the films created by this method consist of mirror domains (MDs), i.e. the domains grow in two orientations which are rotated by 180° with respect to each other (see Fig. 5.1). Since WS_2 exhibits a threefold symmetry (compare Fig. 2.2), these two orientations lead to a mixing of $\overline{\text{K}}$ and $\overline{\text{K}}'$ (i.e. -$\overline{\text{K}}$) points in k-space, as sketched in figure 5.1. Time-reversal symmetry requires the band energies to be the same for plus and minus **k**. Therefore the E vs **k** dispersion is identical along $\overline{\Gamma}$-$\overline{\text{K}}$ and $\overline{\Gamma}$-$\overline{\text{K}}'$. However, the out-of-plane spin polarization is reversed along $\overline{\Gamma}$-$\overline{\text{K}}$ and $\overline{\Gamma}$-$\overline{\text{K}}'$. As a result, the MDs impede measurements with spin resolution. The measured out-of-plane spin polarization along $\overline{\Gamma}$-$\overline{\text{K}}$ and $\overline{\Gamma}$-$\overline{\text{K}}'$ would be reduced or even canceled by mixed contributions from $\overline{\text{K}}$ and $\overline{\text{K}}'$. Therefore, spin-resolved measurements require more sophisticated growth approaches that suppress the formation of MDs.

Two groups were able to largely suppress the growth of MDs in the case of MoS_2 on Au(111) with a domain ratio of 90/10 (Ewert, 2019) and better than 94/6 (Bana *et al.*, 2018). Both use very low evaporation rates in the range between 0.1 and 0.3 SL per hour. Bana *et al.* (2018) in addition use *in situ* X-ray photoemission spectroscopy (XPS) to analyze the Mo 3*d* and S 2*p* core levels and accordingly optimize the growth conditions *in situ*. The same group also synthesized single-oriented SL WS_2 used in this work.

Ewert (2019) explains the preferential growth orientation with slight miss cuts of the Au(111) substrate that result in a preferred orientation of the step edges. While in principle both MDs are equally produced at low evaporation rates, only one domain orientation can ”push” the Au step edges and grow further. This then results in an unequal ratio between the orientations. Bana *et al.* (2018)

further argue that, considering the two topmost layers, the Au(111) substrate has a threefold symmetry that alone would allow growth of a single orientation. In addition, the herringbone surface reconstruction of Au(111) may also play a role according to this group.

In summary, (almost) single-oriented SL of WS_2 can be grown on Au(111) while the exact process behind the underlying suppression of mirror domains is still subject of discussion.

Two SL WS_2 samples have been studied in the present work. Firstly, a full coverage SL WS_2/Au(111) sample grown at the SGM3 endstation at the ASTRID2 synchrotron radiation facility, as described in Dendzik *et al.* (2015). It contains up to 20% bilayer (BiL) by area (Sanders, 2016) and more importantly, has an estimated equal domain ratio of the mirror domains. This sample is used for comparative measurements only and is characterized in appendix A.3. It is called MD SL WS_2/Au(111) from now on.

The main results of the present work have been obtained from a SL WS_2 sample with single orientation and a coverage of about 45% on a Au(111) substrate. This SL WS_2 was grown at the SuperESCA beamline of the Elettra synchrotron-radiation facility in Trieste by evaporating tungsten at a partial pressure of H_2S onto the Au(111) substrate. The single orientation was verified by X-ray photoelectron diffraction (XPD) (Bignardi *et al.*, 2019). The sample was transported under vacuum conditions to Münster and, after a short exposition to atmosphere[2], transferred into the UHV system. Subsequently, the sample was annealed to T $\approx$ 350 °C in UHV to remove contaminants. AES, LEED and TCS were used to check the sample quality.

The chemical composition of the surface was analyzed with AES. Figure 5.2 (e) shows the spectrum (AES excitation energy of 3 keV) with the characteristic structures of tungsten, sulfur and gold according to reference spectra in Davis *et al.* (1976). With the annealing temperature of T $\approx$ 350 °C structural damage of the SL WS_2, possibly occurring at higher annealing temperatures, is excluded. As a result of the relatively low annealing temperature, residual carbon contamination,

[2]Less than 15 minutes to avoid chemical processes.

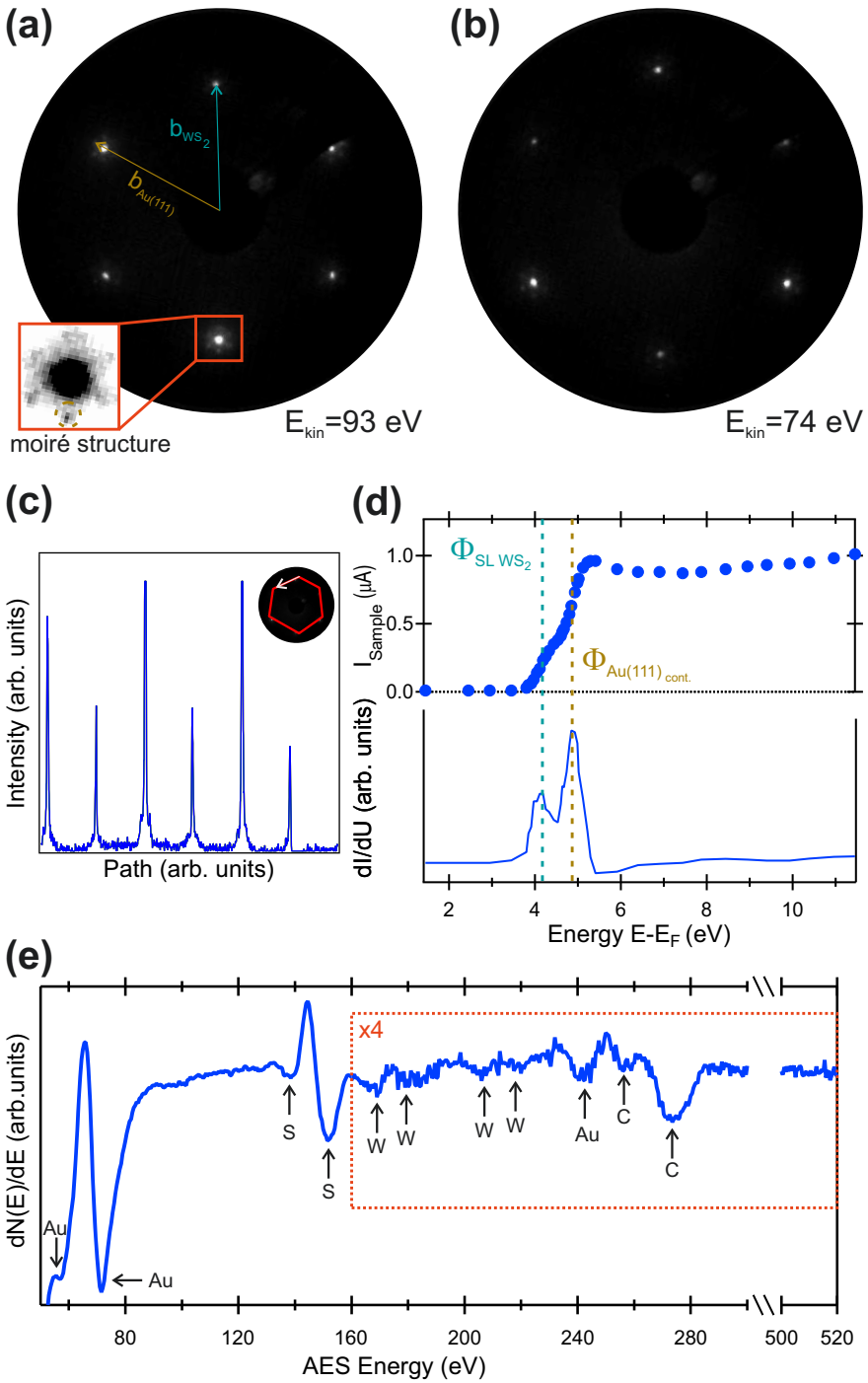

Figure 5.2: (a),(b) LEED pattern at $E = 93\,\text{eV}$ and $E = 74\,\text{eV}$ show the hexagonal structure of the main Au(111) and WS_2 spots. The inset is an inverted LEED image and shows the surrounding of the main WS_2 spot along with the moiré structure and the main Au(111) spot (golden dashed circle). (c) Intensity profile of the 74 eV LEED image along the depicted path clearly indicates the three-fold symmetry. (d) TCS spectra to determine the work function. (e) AES spectrum taken after SRIPE measurements (excitation energy of 3 keV).

seen in figure 5.2 (e), could not be removed. The single-oriented sample consists of areas with WS_2 and areas of the bare Au(111) surface in almost equal parts. The C contaminant covers WS_2, Au(111) or both. C on top of WS_2 is expected to reduce the signal-to-background ratio for WS_2 related features in an IPE spectrum. However, the effect of higher annealing temperatures was tested with the MD SL WS_2/Au(111) sample. Higher temperatures than T $\approx$ 350 °C did not improve the signal-to-background ratio in the IPE spectra. An annealing temperature of about 350° C is not expected to remove C contaminants from Au(111), as usual preparation of the Au(111) surface requires ion sputtering and subsequent annealing to temperatures above 500° C (Hoesch *et al.*, 2004). Furthermore, the work function (see discussion below) and the missing observation of the undisturbed Au(111) surface state (see Sec. 5.2.1) indicates contamination of the bare Au(111) surface that possibly gives rise to the C signal in the AES spectrum.

The LEED images in figure 5.2 were taken after annealing in Münster and show the expected moiré structure due to the lattice mismatch between WS_2 and Au(111). In addition, they have the same three-fold rotational symmetry as measured just after sample preparation in Trieste. Note that for the MD SL WS_2/Au(111) sample, studied with STM and LEED, no indication of three-fold rotational symmetry was found in the LEED pattern (see Appendix A.3). This already indicates the suppression of MD. However, LEED alone can not prove the single orientation of SL WS_2, since the underlying Au(111) substrate also has a threefold symmetry as mentioned above.

The work function Φ_{WS_2} is determined from the onset of the TCS spectrum in figure 5.2 (d). In the case of the SL WS_2/Au(111) sample, one has to consider the presence of two different surfaces, namely Au(111) and SL WS_2, giving rise to two different work functions. As a consequence, two steps are present in the sample current, at 4.19 eV and at 4.87 eV. To determine Φ_{WS_2} it is necessary to relate the steps to the respective materials, i.e. Au(111) and SL WS_2. For this purpose the observed steps are discussed along with various work functions obtained from the literature that are shown in table 5.1.

Table 5.1: Experimental determined work functions of materials discussed in the text.

Φ of different WS_2 samples		
bulk WS_2	4.95 eV	present work
bulk WS_2	4.90 eV	(van Le *et al.*, 2014)
WS_2/SL graphene/SiC(0001)	4.50 eV	(Forti *et al.*, 2017)
MD SL WS_2/Au(111)	4.43 eV	present work
Steps in TCS spectra of 45% coverage SL WS_2/Au(111)		
step one	4.19 eV	
step two	4.87 eV	
Φ of different Au samples		
air exposed polycrystalline Au	4.70 eV	(Wan *et al.*, 2005)
clean polycrystalline Au	5.40 eV	(Forti *et al.*, 2017)
clean Au(111)	5.31 eV	(Michaelson, 2008)

The clean Au(111) surface has a work function of $\Phi_{\mathrm{Au(111)_{clean}}} = 5.31$ eV (Michaelson, 2008). However, the SL WS_2/Au(111) had been in atmosphere for a short time and the resulting contamination, especially C, was probably not fully removed. A reduction of the work function from 5.4 to 4.7 eV is reported after exposing polycrystalline Au to atmosphere and bringing it back to UHV (Wan *et al.*, 2005). The reduction is less strong in the present work since some contamination, especially H and O, are likely to be removed at the annealing temperature. This is supported by comparing the AES spectrum in figure 5.2.1 to the one of Wan *et al.* (2005). In the latter also oxygen contamination is present (structure at 511 eV), while the former only shows C contamination and no signal for O occurs in figure 5.2.1. Given the discussion above, the second step in figure 5.2.1 (d) is attributed to the work function $\Phi_{\mathrm{Au(111)_{cont.}}} = 4.87 \pm 0.08$ eV of the C contaminated Au(111) surface.

Consequently the first step must belong to the work function of SL WS_2. The work function of SL WS_2/MLG/SiC(0001) was determined to be 4.5 eV (Forti *et al.*, 2017). This is consistent with the value of $\Phi_{\mathrm{MDSLWS_2}} = 4.43 \pm 0.08$ eV obtained for the MD SL WS_2/Au(111) sample in appendix A.3. This value is much closer to the first step at 4.19 eV than to the second step observed in the case of single-oriented

SL WS_2. However, an energy difference of 0.24 eV between Φ_{MDSLWS_2} and the first step in figure 5.2.1 (d) remains. Two reasons are likely to contribute to this difference.

(i) While the single-oriented low-coverage sample is only SL, the MD SL WS_2/Au(111) sample with full coverage also contains a significant amount of BiLs (up to 20 %). Since the work function of bulk WS_2 is at about 4.9 eV, much higher than the reported SL work function, one can assume the BiL to have a higher work function than the SL. Considering the SL/BiL ratio of the MD SL WS_2/Au(111) sample of about 0.8/0.2 and assuming work functions of 4.19 eV and 4.9 eV for SL and BiL, respectively, one would expect an average work function of 4.33 eV. However, major contributions of areas with significantly higher work functions would create a second step in the TCS spectrum of MD SL WS_2/Au(111). Such a second step can not be observed (see Fig. A.4) and hence the effect of the Bil contribution in the MD SL WS_2/Au(111) sample must be small.

(ii) Since the single-orientation SL WS_2 has a coverage of only 45 %, it consists of many separated islands as can be seen in figure 4 of Bignardi *et al.* (2019). In other words, significantly parts of the area are edges of the islands. Such edges can have a lower local work function, as shown in the case of noble metals (Jia *et al.*, 1998). As a result, the average work function of the whole sample area, as measured by TCS, is also lower than for a surface without edges.

Due to (i) an (ii) it is expected that the work function of the low-coverage single-oriented SL WS_2 Φ_{SLWS_2} is lower than Φ_{MDSLWS_2}. Therefore, the first step in the TCS spectrum is attributed to $\Phi_{SLWS_2} = 4.19 \pm 0.08$ eV.

In summary, the AES data shows slight C contamination of the SL WS_2/Au(111) sample, possibly due to C contamination of the Au(111) areas, which are not covered by WS_2. The expected moiré structure is seen in STM and LEED. The sharp LEED pattern indicates a well ordered surface of SL WS_2/Au(111). The observed three-fold symmetry in LEED further indicates non equal distribution of the mirror domains. The latter result is proved by spin-resolved measurements in section 5.2.3.

5.1.2 p-type 2H WS_2 Samples *

The bulk 2H WS_2 sample was grown by the 2DSemiconductor company using a flux growth method. Information about typical WS_2 samples are available online[3]. To increase the electrical conductivity of the bulk samples and prevent charging during SRIPE measurements, the sample is p-doped with Nb atoms. The doping level is within a range between $1 \cdot 10^{17}\ cm^{-3}$ and $5 \cdot 10^{18}\ cm^{-3}$. This exceptionally high doping level is likely to prevent significant charging of the sample.

The sample was mounted using an Ag-containing electrically and thermally conducting glue on a titanium sample holder as seen in figure 5.3 (a). Notably the sample is rather small with approximately 3 times 5 mm^2 and has a macroscopically rough surface with several facets. The sample was prepared by *in situ* mechanical exfoliation in the load lock at a pressure of about 10^{-8} mbar using adhesive tape. Numerous attempts of exfoliation have been performed. The sample surface used for IPE measurements is shown in figure 5.3 (b) inside the UHV setup. Most of the glue beneath the sample had been removed by the exfoliation attempts. The sample is significantly thinner than before, but still consists of several facets. The lower part of the sample is very rough. Therefore, measurements were only conducted at the upper part within the red box in figure 5.3 (b).

To check the surface quality, AES, LEED and TCS was used. In addition, the direct comparison of IPE spectra of bulk and SL material (see Sec. 5.2.2) indicates a similar surface quality as SL WS_2/Au(111). The main problem is apparently the macroscopically rough surface, i.e. the different facets of the bulk WS_2 sample as discussed in the following.

The AES spectrum (excitation energy of 3 keV) in figure 5.3 is similar to the one of SL WS_2/Au(111) in figure 5.2 with a few differences to be discussed. Obviously the Au related structures are not present in the case of the pure bulk

* Parts of the results in this section have been gained in collaboration with Lukas Musiol during his bachelor thesis (Musiol, 2018).

[3] https://www.2dsemiconductors.com/p-type-ws-crystals/

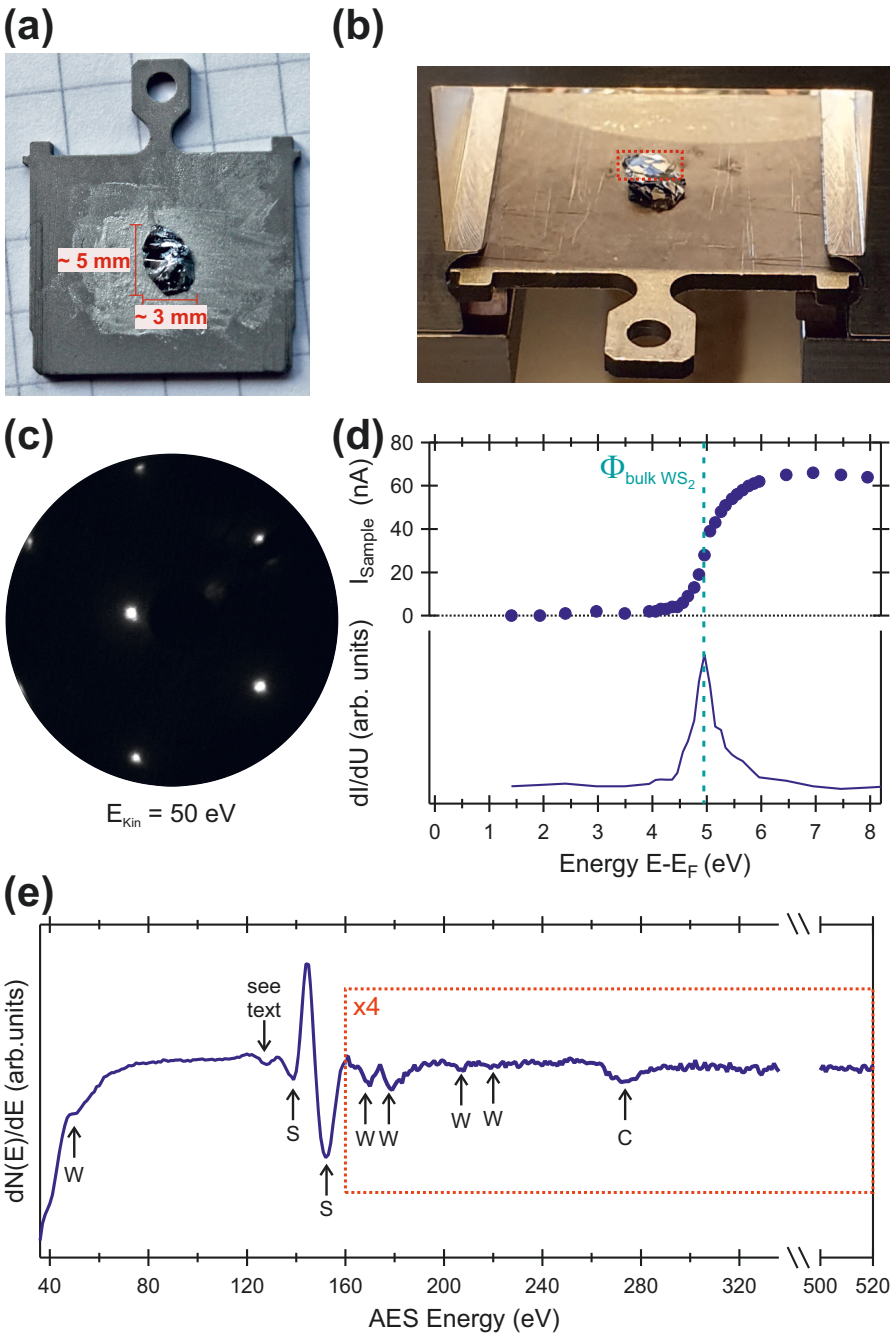

Figure 5.3: Characterization of the p-type 2H WS_2 sample. (a) Photo of the sample glued on the titanium target holder. The silvery areas around the sample are silver-containing conducting glue. (b) Photo of the same sample after several micromechanical exfoliation attempts. The IPE measurements have been conducted on the upper area of the sample that is marked by a red dashed line. (c) The LEED pattern at $E = 50\,\text{eV}$ shows a hexagonal structure. (d) TCS spectra for determining the work function. (e) AES spectrum taken after SRIPE measurements (excitation energy of 3 keV).

material. Furthermore the C-related signal at 272 eV is about four times lower. However, residual carbon atoms are on top of WS_2 in the case of the bulk material. Micromechanical exfoliation on a macroscopically rough surface is likely to miss some areas. These areas are responsible for the contamination.

This interpretation is consistent with the observation of a pronounced feature at about 127 eV that is, within the experimental accuracy, not or just slightly visible in case of SL WS_2/Au(111). No reasonably expected element (W,C,Ti,Ag,Nb) besides S can explain this structure. In general, the exact shape and energy in AES also depends on the chemical environment. Indeed, strong differences in AES spectra can be seen for various S containing materials, including MoS_2 (Vaughan and Tossell, 1986). For MoS_2 a, compared with figure 5.3, less pronounced structure at about 127 eV is visible. Another explanation can be SO_4^{2-} species with its main feature occurring at about 125 eV (Bernett *et al.*, 1977). Therefore the pronounced structure at 127 eV is attributed to sulfur containing contamination of various kind, located in the minor areas missed by the mechanical exfoliation process.

The LEED image in figure 5.3 shows a hexagonal symmetry. This indicates that the facets are not randomly in-plane oriented but are grown in preferred directions. Consequently, **k**-resolved information can be obtained with the sample. In addition, three observations in LEED are made. These observations and the implied consequences for the subsequent IPE study are:

(i) The main spots appear larger for bulk WS_2 than for SL WS_2/Au(111), despite no satellite spots due to the moiré structure are present. As can be seen in the photo of the sample, the facets are slightly tilted to each other, resulting in a non-flat surface. This tilt leads in the LEED image to the observation of large spots. In IPE, the faceting of the sample is expected to worsen the **k** resolution and hence broaden the spectra.

(ii) Moreover the surface is inclined by 4° and 1.5° in the horizontal and vertical axes[4], respectively. The IPE setup allows to compensate inclination in only one axis. As a consequence, the uncompensated vertical inclination of 1.5° leads to an offset in **k**-space that is perpendicular to the measurement

[4]The latter is compensated in the LEED image.

direction. According to equation 3.3, this offset can be estimated to approximately[5] 0.03 Å^{-1}. The offset is comparable to the momentum resolution (see Sec. 3.2.1) and should not lead to significant changes of the measured electronic structure.

(iii) The LEED image could only be observed in a small area of the sample. It undergoes significant changes when moving the sample 0.3 mm or more in any direction. The LEED spots become broader and blurry. Additionally, the orientation of the pattern is slightly changed. Probing an area larger than the LEED beam size plus 0.3 mm diameter strongly perturbs **k**-resolved experiments. Since the LEED and IPE electron beam size is similar, IPE measurements in a sufficiently flat area of the sample surface can be conducted. Nonetheless, minor parts of areas outside the suitable sample area are also probed in IPE, especially with increasing angle of electron incidence. These are likely to contribute to broadening of the spectra. For higher angles of electron incidence, the electron beam size on the sample becomes larger and hence the broadening is expected to be more pronounced.

A work function of $\Phi_{BulkWS_2} = 4.95 \pm 0.08\,\text{eV}$ is determined by TCS (Fig. 5.3 (d)). Φ_{BulkWS_2} is consistent with a value found in the literature (van Le *et al.*, 2014). Clearly only one step occurs, indicating no major areas with other materials that have different work functions. An extensive discussion about WS_2 work functions is found in the previous section.

In summary, a strongly p-doped bulk WS_2 sample has been prepared *in situ* by micromechanical exfoliation. While the surface quality is not perfect, especially the macroscopically corrugation of the sample, LEED, AES and TCS indicate the necessary requirements for IPE measurements are met. The bulk sample was used to study the influence of the Au(111) substrate on SL WS_2 by directly comparing spin-integrated IPE spectra of SL and bulk samples in section 5.2.2.

[5] Considering an electronic state one eV above the Fermi level.

5.2 SL-WS_2 on Au(111)

5.2.1 Conduction-Band Dispersion along $\overline{\Gamma} - \overline{\mathrm{K}}$

To get information about the size of the energy gap and the spin dependence of the confining bands, SRIPE measurements of the CBs are necessary. Furthermore, the E vs $\mathbf{k}_{\parallel}$ band dispersions, in particular of the LCB along $\overline{\Gamma}$-$\overline{\mathrm{K}}$, are important for possible transitions between VB and CB and hence possible applications.

Figure 5.4 presents SRIPE spectra for various angles of electron incidence θ along $\overline{\Gamma}$-$\overline{\mathrm{K}}$. As mentioned before, in the present setup, out-of-plane sensitivity is only available for $\theta \neq 0°$ with increasing sensitivity for larger θ. Therefore, spin-integrated data are shown as black dots for $\theta \leq 15°$. For $\theta \geq 20°$, spin-resolved data for out-of-plane spin sensitivity are presented as purple (yellow) dots for spin polarization parallel (antiparallel) to the surface normal. Clear out-of-plane spin asymmetries in the CBs are detected. Estimated peak positions using fits and, if the statistics is sufficient, preferably the second derivative, are marked by small vertical lines.

The Fermi edge is visible in all ARPES (Fig. 5.11) as well as SRIPE spectra (Fig. 5.4). While WS_2 sustains its semiconducting properties when deposited on Au(111) (Dendzik *et al.*, 2017), the approximately 55% uncovered metallic Au(111) areas cause the Fermi level onset in the spectra.

The experimental results for the CBs are summarized in a $E(\mathbf{k}_{\parallel})$ plot in figure 5.5: Black, yellow, and purple squares denote peak positions in the spectra of figure 5.4 for spin-integrated, out-of-plane spin-down, and spin-up polarized data, respectively. The experimental data are presented along with DFT calculations performed by Albert Bruix: (i) the projected bulk band structure of Au(111) [grey shaded area], (ii) a freestanding SL WS_2 [grey lines], and (iii) a SL WS_2 on top of a six layer slab Au(111) [blue dots]. The size of the blue dots are obtained from the supercell calculation and indicate the spectral weight of the effective band structure at each corresponding $\mathbf{k}$-point and energy interval resulting from the band unfolding method (for details see Dendzik *et al.* (2017)). The absolute energies in the DFT calculation do not fit the experimentally data because of the

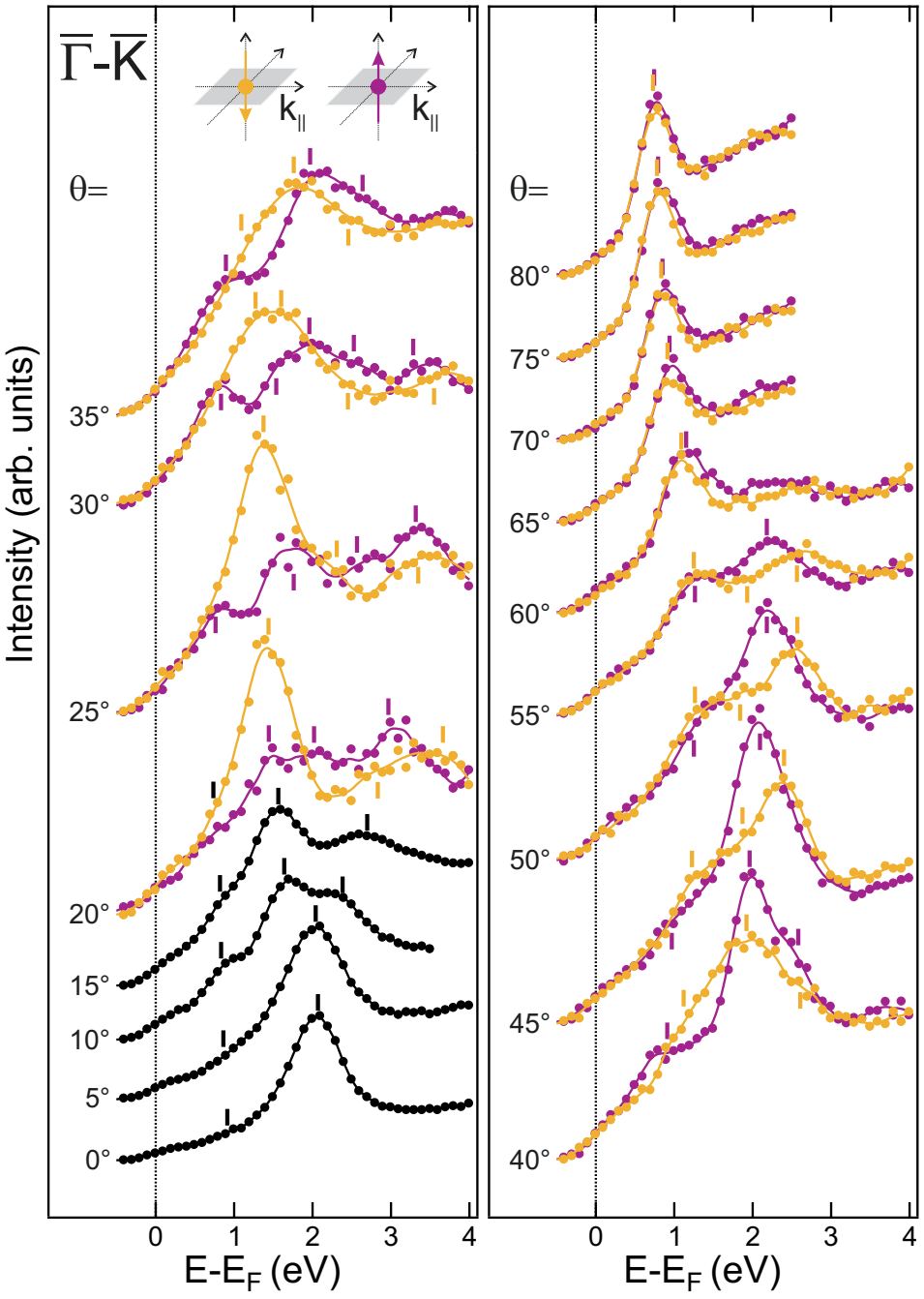

Figure 5.4: Angle-resolved inverse-photoemission spectra of single-layer WS_2 on Au(111) along $\overline{\Gamma}$-$\overline{K}$. For $\theta \leq 15°$, spin-integrated data are shown as black dots. For $\theta \geq 20°$, spin-resolved data for out-of-plane spin sensitivity are presented as purple (yellow) dots for spin polarization parallel (antiparallel) to the surface normal. Vertical lines mark peak positions in the spectra.

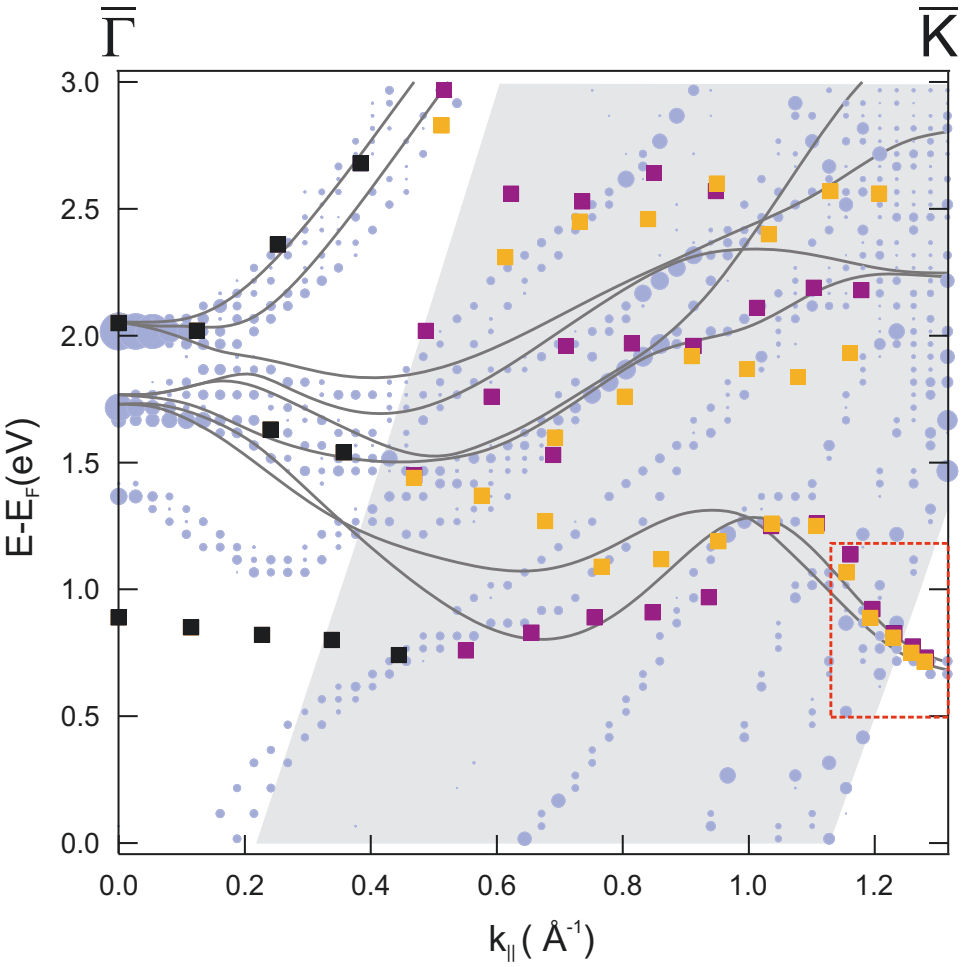

Figure 5.5: E vs $\mathbf{k}_{||}$ band dispersions along $\overline{\Gamma}$-$\overline{K}$. Peak positions derived from the spectra in figure 5.4 are included as black, yellow, and purple squares for spin-integrated, out-of-plane spin-down and spin-up intensities, respectively. The grey-shaded area indicates bulk bands of Au, projected onto the (111) surface. Solid lines show results of a DFT calculation for a freestanding single layer of WS_2. Blue dots represent the band structure of WS_2 on Au(111) based on a DFT calculation. The region of the CBs near $\overline{K}$ is highlighted with a red box. The calculations have been performed by A. Bruix.

well known underestimation of the band gap in DFT calculations. In addition, the band gap renormalization due to the heavy screening of the Au(111) substrate is not included in the calculation. The theoretical results for the CBs have been rigidly shifted in energy to match the experimental results of the LCB at $\overline{K}$. Notably, with this calibration, the bands at $\overline{\Gamma}$ between 1.5 and 2.0 eV fit as well.

Bands in regions where Au(111) has no states, e.g. close to $\overline{\Gamma}$ and below 1 eV close to $\overline{K}$, are expected to have almost pure WS_2 character. Within the grey-shaded region, Au bands exist which might hybridize with WS_2 bands. To study the influence of the Au(111) substrate, comparative measurements are performed on bulk 2H WS_2. The results shown in Figs. 5.7, 5.8 and A.7 are extensively discussed in section 5.2.2.

The experimental energy dispersions of SL WS_2 in figure 5.5 predominantly follow the band dispersions of the freestanding layer with some deviations where bands of Au and WS_2 hybridize. The largest deviation between experiment and theory is observed for the LCB in the vicinity of $\overline{\Gamma}$, which appears in the experimental data with relatively low intensity. Remarkably, bands split off to lower energy around $\overline{\Gamma}$ are also theoretically expected for the adsorbed layer compared with the freestanding layer (see Fig. 5.5), albeit not as much as experimentally observed. Note that the observed feature could also be due to indirect transitions occurring at the energy where the density of states (DOS) of SL WS_2 begins, i.e. around 0.7 eV. Similar features are observed in case of bulk WS_2 (see Fig. 5.7), yet less intense than in case of the SL (e.g. $\theta = 10^\circ$ in figure 5.7). Consequently the features in SL WS_2 can not be explained with indirect transitions alone. Since the features are not perfectly reproduced in the calculation in figure 5.5, it is worth to consider alternative origins for them.

The origin of the observed features of the LCB in the vicinity of $\overline{\Gamma}$ is unlikely to be hybridization with projected bulk Au bands, which do not occur in this region of **k**-space. The Au(111) Shockley surface state (SS) is expected to be at significantly lower energies around $\overline{\Gamma}$ (Wissing *et al.*, 2013) and has a parabolic dispersion. Unsurprisingly, given the C contamination on Au(111), no feature can be attributed to the Au(111) SS, while it is clearly visible in ARPES measurements where the sample did not leave the UHV (Dendzik *et al.*, 2015). The missing observation of the undisturbed SS is further supported by the observation of the same features at the full coverage SL WS_2 sample (see Fig. A.6). However, Au(111) areas below the SL WS_2 are expected to be clean. It was shown that the Au(111) SS is still present but modified when covered with various adsorbates (Forster *et al.*, 2003; Andreev *et al.*, 2004; Forster *et al.*, 2007; Kanai *et al.*, 2009). Therefore, a

possible explanation of the experimental observation is a modified Au(111) SS. To investigate this, additional SRIPE measurements of the features, sensitive to the in-plane perpendicular (i.e. Rashba) spin polarization may be conducted. This would allow to determine the spin structure and may provide further indication toward or against an modified SS by comparing the experimentally observed and calculated spin polarization. In addition, determining the exact distance between WS_2 and the Au(111) substrate would provide an important parameter needed for calculations.

An important question about SL WS_2 and SL TMDCs in general is the position of the CBM. Most studies indicate the CBM to be at the $\overline{\text{K}}$ point (Klein *et al.*, 2001; Mak *et al.*, 2010; Splendiani *et al.*, 2010; Kumar and Ahluwalia, 2012; Zhao *et al.*, 2013; Shi *et al.*, 2013; Roldán *et al.*, 2014; Sun *et al.*, 2016). However, it is predicted that the energy at $\overline{\text{K}}$ is only few meV lower than at the so-called Q point about halfway between $\overline{\Gamma}$ and $\overline{\text{K}}$. There are even indications of the CBM being at the Q point (Hsu *et al.*, 2017). Experimentally, spectral features around Q are found, but are possibly influenced by Au states (see. Sec. 5.2.2), with similar energies as the lowest spectral features at $\overline{\text{K}}$. Therefore, the experiment cannot resolve whether the CBM position is at $\overline{\text{K}}$ or at Q.

In contrast to the Q point, the LCB in proximity to $\overline{\text{K}}$ is found in a projected band gap of Au(111), thus no or little influence of the Au(111) states is expected. This will be put to test in the following section by comparing results of SL WS_2/Au(111) with respective measurements at bulk WS_2. Due to the photon energy of 9.9 eV in our experiment, the accessible $\mathbf{k}_{\parallel}$ range is limited. Nevertheless, the data for $\theta = 80°$ come very close to $\overline{\text{K}}$ at the final-state energy of the LCB (97% of $\overline{\Gamma}$-$\overline{\text{K}}$, see Fig. 5.5). The energy of the LCB in proximity to $\overline{\text{K}}$ is determined to 0.71 ± 0.03 eV, which can be extrapolated to 0.69 ± 0.03 eV at $\overline{\text{K}}$ by assuming a parabolic band behavior.

Using the SRIPE results together with SARPES measurements, the important parameters of the spin dependence of the band gap are experimentally determined in section 5.2.3. The subsequent section shows that these results reflect the properties of the non-influenced (or negligibly influenced) SL WS_2 by conducting a comparative study without the Au(111) substrate.

5.2.2 Comparative Study of Bulk 2H WS_2 with SL WS_2/Au(111): Influence of the Au(111) Substrate*

To experimentally study the influence of the Au(111) substrate on SL WS_2, comparative IPE measurements for WS_2 without the Au(111) substrate are required. SL WS_2 on an insulating substrate with a large band gap (e.g. SiO_2) which is expected to have no or little effect on SL WS_2, would be an option for this purpose. However, no sample meeting the requirements for IPE measurements described in Sec. 5.1 was available. Therefore, bulk 2H WS_2 was the best option.

As written in Sec. 2.2, bulk WS_2 has different properties than SL WS_2, namely: (i) a reduced size of the band gap with respect to the SL. (ii) An indirect band gap with the VBM at $\overline{\Gamma}$ and the CBM at the Q point (about halfway along $\overline{\Gamma}$-$\overline{K}$). (iii) A k_z-dependent electronic structure. (iv) Inversion symmetry that leads to spin-degenerate bands.

(i) leads to different energies of the CBs in SL relative to the CBs in bulk WS_2. In addition (ii), band energies at certain points in **k**-space change when altering the sample thickness. This is especially true for the lowest CB at the Q point that is calulated to be drastically lowered in energy in the bulk system (Cappelluti *et al.*, 2013). In contrast, the lowest CB at the $\overline{K}$ point is expected to have no large differences between bulk and SL. The *GdW*-calculated electronic structure of SL and bulk WS_2, performed by M. Drüppel (2017), is shown in figure 5.6, illustrating all effects discussed above.

The spin degeneracy of bulk WS_2 (iv) leads to large differences between bulk and SL material when measuring with spin resolution. This is circumvented by using spin-integrated data, i.e. the sum of the two spin channels ($n_{Int} = n_{\uparrow} + n_{\downarrow}$). Note that spin signals in principle can occur, due to spin-layer locking described in Sec. 2.2. Two spin-resolved IPE spectra corresponding to the region around the Q point are exemplary shown in figure A.8. With the present setup and the used photon detection energy no significant out-of-plane spin polarization was observed. As a result, and due to the comparative focus of the study, this section will focus on the spin-integrated data.

* Parts of the results in this section have been gained in collaboration with Lukas Musiol during his bachelor thesis (Musiol, 2018).

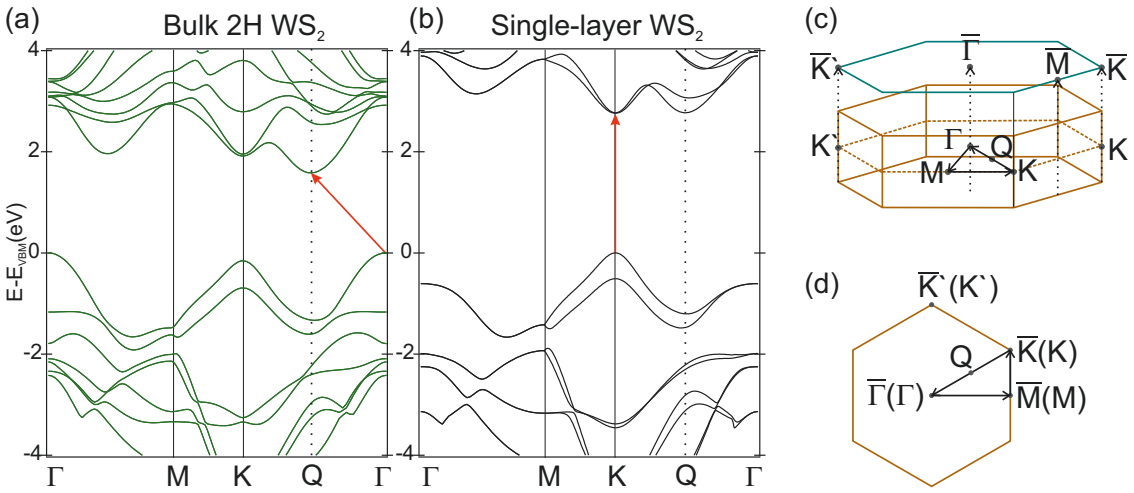

Figure 5.6: The electronic structure of bulk 2H WS_2 (a) and SL WS_2 (b) calculated within the *GdW* approximation by M. Drüppel (2017). (c) Hexagonal BZ of 2H bulk WS_2 along with the respective projected SBZ. Arrows show the path in **k**-space where the calculation is performed. (d) The two-dimensional BZ belonging to SL WS_2. Due to its two-dimensionality it is identical to its SBZ. Therefore, the use of bars to indicate symmetry points of the SBZ is optional.

Spin-integrated IPE spectra along $\overline{\Gamma}$-$\overline{K}$[6] for bulk WS_2 are shown in figure 5.7. All data in this chapter were measured with the photon counter C4 (compare Fig. 3.2) and hence the same experimental geometry. For the purpose of comparison, all spectra in figure 5.7 have been normalized to the absorbed charge[7] in the IPE experiment. Exceptions are spectra with negative angle of electron incidence which exhibit lower intensity in counter C4 since the sample is facing away from C4. These spectra are multiplied by factors mentioned in figure 5.7 to increase visibility. Note that the spectrum for $\theta = 10°$ is distinctly different in intensity and shape in comparison to the rest of the data set, potentially due to hitting another facet of the sample surface.

Strong energy dispersion is observed throughout the spectra series. The peak positions are analyzed by utilizing the second derivative. This is possible because the IPE spectra exhibit a linear background (compare e.g. $\theta = 5°$) and the scattering of the data points is very small. Fitting can determine peak positions more precisely than the second derivative when few parameters are involved (e.g. in

[6] Without spin resolution, $\overline{\Gamma}$-$\overline{K}$ and $\overline{\Gamma}$-$\overline{K}'$ cannot be distinguished. For this section the direction is defined as $\overline{\Gamma}$-$\overline{K}$. However, it is not necessarily the equivalent direction to $\overline{\Gamma}$-$\overline{K}$ of the SL sample.
[7] By measuring the sample current.

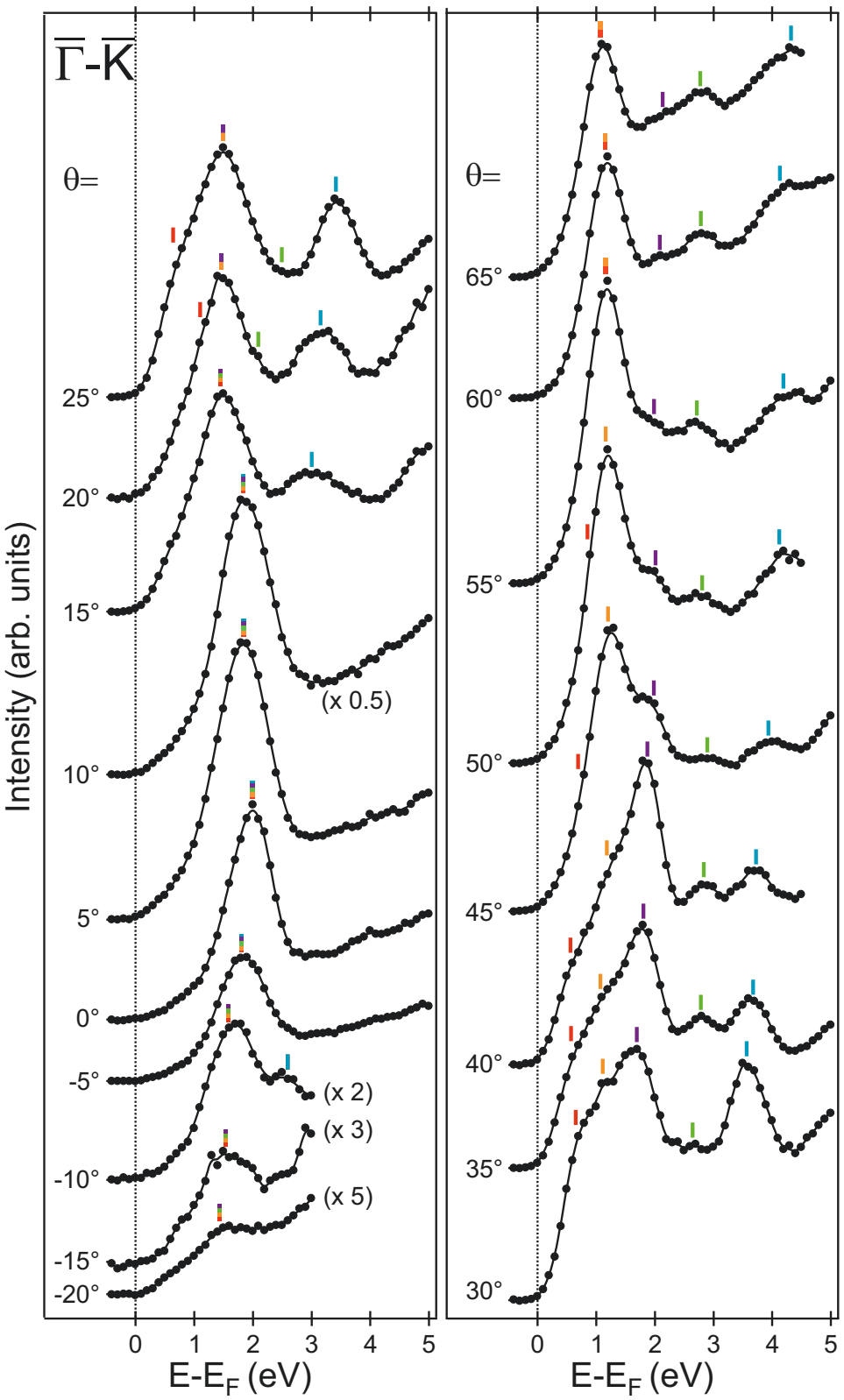

Figure 5.7: IPE spectra of bulk WS_2 along $\overline{\Gamma}$-$\overline{K}$. Vertical line markers indicate peak positions in the spectra. The colors refer the interpretation of the bands. Features that represent multiple bands are marked with multiple colored vertical lines.

Sec. 5.2.3). However, in the case of the up to five different, partly overlapping, features that are present in the spectra (see e.g. $\theta = 40°$), fitting would involve[8] up to seventeen independent parameters. These mostly unknown parameters have to be assumed and different assumptions lead to a wide range of different fitting results. In contrast, the analysis with the second derivative does not rely on an assumption of parameters. The estimated peak positions are indicated by colored vertical line markers in figure 5.7. The colors refer to the interpretation of the features as different bands.

The feature with the lowest energy, presumably the CBM, is found at 0.56 eV in the spectrum for $\theta = 40°$. At about the same energy, steps with small intensity appear for the spectra with $\theta \leq 10°$ (not marked). These steps with low intensity are interpreted as indirect transitions due to the increasing WS_2 density of state at the energy of the CBM. Note that the steps also occur for the SL $WS_2/Au(111)$ sample, yet being more pronounced in this case (see Fig. 5.4).

The features that are considered as direct transitions are translated into an $E(\mathbf{k}_\parallel)$ plot along $\overline{\Gamma}$-$\overline{K}$ in figure 5.8. In the experimental $E(\mathbf{k}_\parallel)$ dispersion, shown as colored squares, several bands are identified. At $\overline{\Gamma}$, the bands overlap in the experiment and lead to the feature with large width that is observed in the spectrum for $\theta = 0°$. With increasing $\mathbf{k}_\parallel$, more and more bands are identified separately. The lowest band energies are found about halfway along $\overline{\Gamma}$-$\overline{K}$, i.e. around Q.

The k_z value of the bands can not be determined, since no variation of the photon energy is possible with the present IPE setup. As a result, the experimental $E(\mathbf{k}_\parallel)$ dispersion can only be compared to the surface-projected bulk bandstructure. The grey areas represent the surface-projected bulk bandstructure along $\overline{\Gamma}$-$\overline{K}$ of 2H WS_2, as calculated by a DFT calculation that was performed by P. Krüger (2018). Similar to the previous section, the reference energy of the calculation has to be calibrated. Assuming equal spectral intensity for all bands at $\overline{\Gamma}$, the only observable feature of the spectrum for $\theta = 0°$ must be in the middle of the calculated bands at $\overline{\Gamma}$. The DFT calculation was shifted accordingly.

[8] Including the linear background.

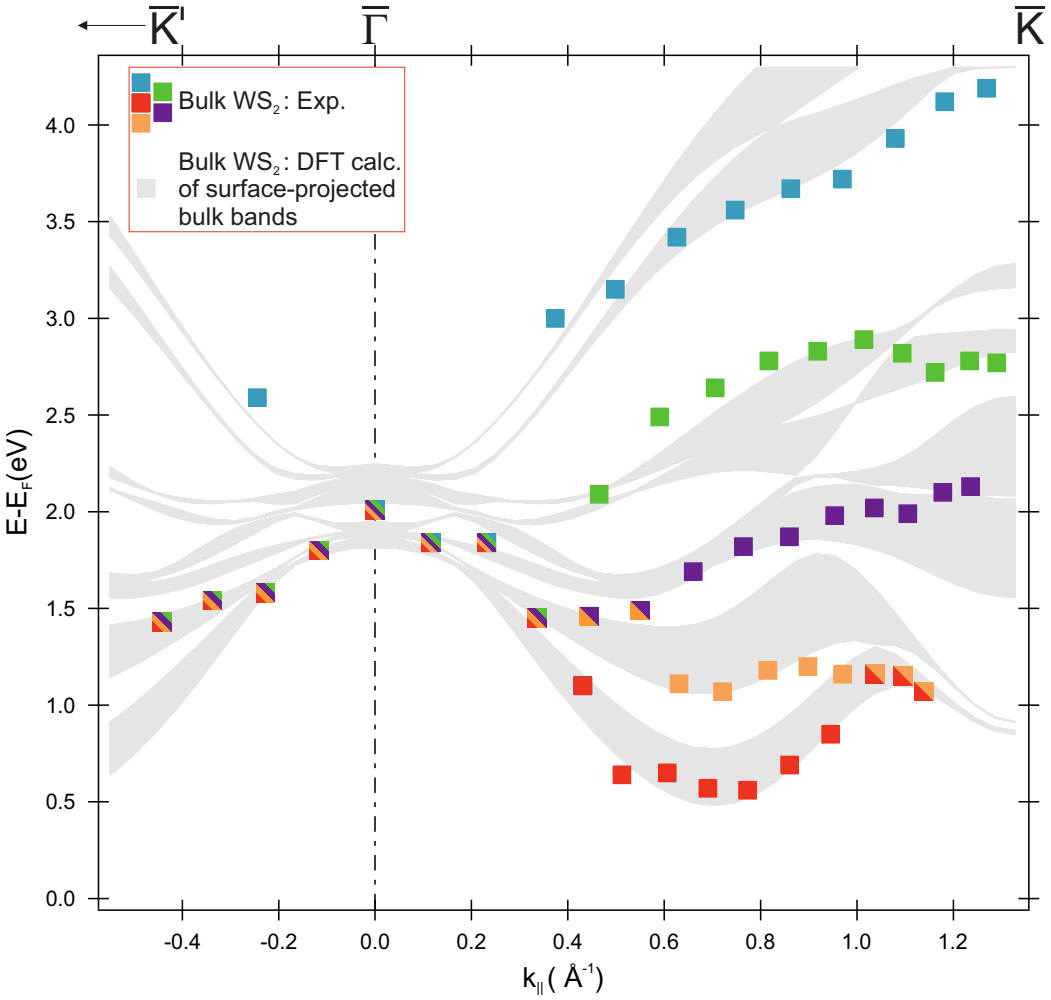

Figure 5.8: E($\mathbf{k}_{||}$) band dispersions along $\overline{\Gamma}$-$\overline{K}$. The peak positions of bulk WS_2, derived from the spectra in figure 5.7, are included as colored squares. The colors refer to the interpretation of bands. Features that represent multiple bands are shown with multiple colored squares. The grey-shaded areas indicate surface-projected bulk bands of WS_2 and are a result of a DFT calculation performed by P. Krüger (2018).

Remarkably, for all experimentally identified bands in figure 5.8, corresponding calculated bands are found. However, not all calculated bands are separately identified in the experiment. One example is the above mentioned feature in the $\theta = 0°$ spectrum corresponding to $\overline{\Gamma}$. Another example are the blue marked features that correspond to two bands in the calculation. These features become increasingly broader for $\theta \geq 40°$, reflecting the increased separation of involved bands. In contrast the features corresponding to the lowest CBs close to $\overline{K}$ ($\theta \geq 55°$) appear to be rather narrow, reflecting the small separation of the two lowest CB.

In Figs. 5.9 and 5.10 the spin-integrated spectra of SL WS_2/Au(111)[9] and 2H bulk WS_2 along $\overline{\Gamma}$-$\overline{K}$ are shown in two different ways.

(i) It is tried to compare the absolute intensities of the two data sets in figure 5.9. In addition to the experimental geometry, the absolute intensity is determined by the matrix element of the IPE transition (see Sec. 3.1). A change in intensity between bulk WS_2 and SL WS_2/Au(111) data reflects a change of the matrix element due to the changed involved electronic states. Therefore, the comparison of absolute intensities can indicate hybridization between the electronic states of WS_2 and Au(111). Comparing the absolute intensities of IPE spectra is challenging and usually impossible since the intensities are not only influenced by the matrix elements but also by the quality of the sample surface, the experimental geometry and other experimental parameters (compare Ch. 3). Furthermore, the gas detectors, used in IPE, may have different efficiencies depending on the quality of the entrance window as well as the type and pressure of the counter gas. Given the many parameters influencing the absolute intensity, a comparison of absolute intensities is, if at all, only meaningful when the measurements are conducted with the *identical* experimental setup. This is the case for the data discussed here. In addition to the influence of experimental parameters, the incomplete coverage of 45% for the SL WS_2 on Au(111) sample has to be taken into account. Accordingly, the 2H bulk WS_2 spectra are multiplied by a factor of 0.45.

[9] The respective spin-resolved spectra are shown in figure 5.4.

(ii) A way to compare different spectra is to find a meaningful way to normalize them. One way is to normalize to the maximum intensity. With this normalization, the energy positions and the peak-to-background ratio of features can be compared. For example, this approach works well for comparing the MD full coverage SL WS_2/Au(111) with the single-oriented 45% coverage SL WS_2/Au(111) sample, as shown[10] in figure A.6. The same depiction is done in figure 5.10 for the datasets of the 45% coverage SL WS_2/Au(111) sample (black dots) and the bulk 2H WS_2 sample (red dots). A comparison of all different studied WS_2 samples is found in figure A.9.

The energy of corresponding features are similar in many cases, as seen in figure 5.10 and in an E vs $\mathbf{k}_{||}$-plot in figure A.7. This result can be misleading for the following reasons. In contrast to the SL, bulk WS_2 has a k_z dependent electronic structure. The band energies vary by several 100 meV with different values of k_z, as can be seen in the calculation in figure 5.8. In addition, the energies are influenced by the size of the band gap and the doping level of the samples. Therefore the nearly matching energies in figures 5.10 and A.7 are just accidental. However, the shape and the peak-to-background ratio of corresponding features in the two data sets as well as the E vs $\mathbf{k}_{||}$-dispersion must be similar if no influence of the Au(111) substrate is present in the case of SL WS_2/Au(111).

Firstly, general differences between the spectra in figures 5.9 and 5.10 are discussed. In all spectra of the SL WS_2/Au(111) sample, an onset at the Fermi energy occurs due to the CBs of the underlying Au(111) substrate. This is not visible for the bulk WS_2 sample. Furthermore, the step occurring at energies of about 0.70 eV (0.56 eV) for SL WS_2/Au(111) (bulk WS_2) is far more pronounced in the case of SL WS_2 (best seen at $\theta = 10°$). The different intensities of the observed step give rise to the question about the origin of this feature. A possible origin is a modified Shockley-SS of the WS_2 covered Au(111) substrate (see discussion in Sec. 5.2.1).

[10] As expected these data sets are similar with a higher background in case of the 45% coverage sample due to the carbon-contaminated areas.

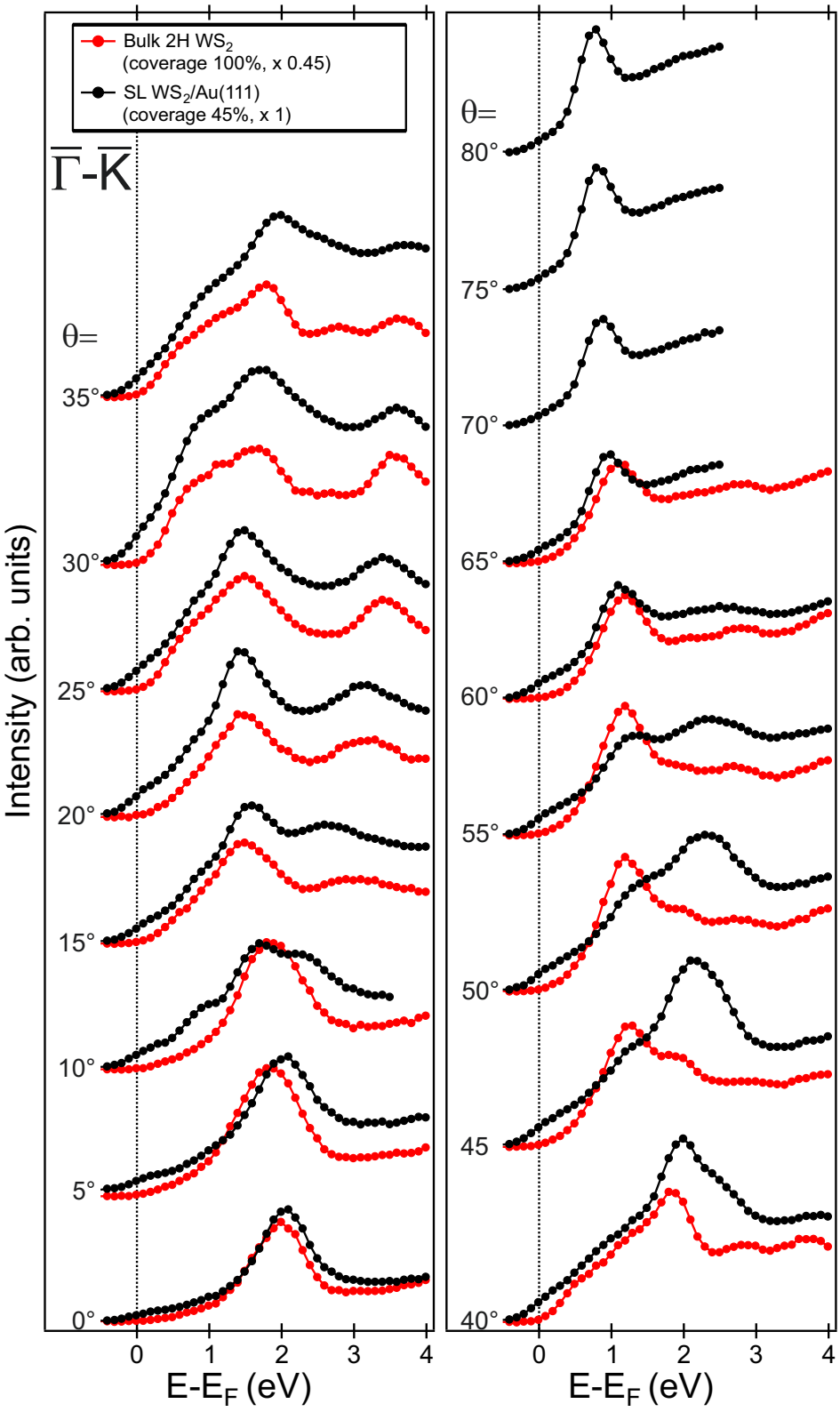

Figure 5.9: IPE spectra of bulk WS_2 and SL WS_2/Au(111) along $\overline{\Gamma}$-$\overline{K}$. Spin-integrated data are shown as black dots (red dots) for SL WS_2/Au(111) (bulk WS_2). Spectra are normalized to absorbed charge with consideration of the different WS_2 coverages.

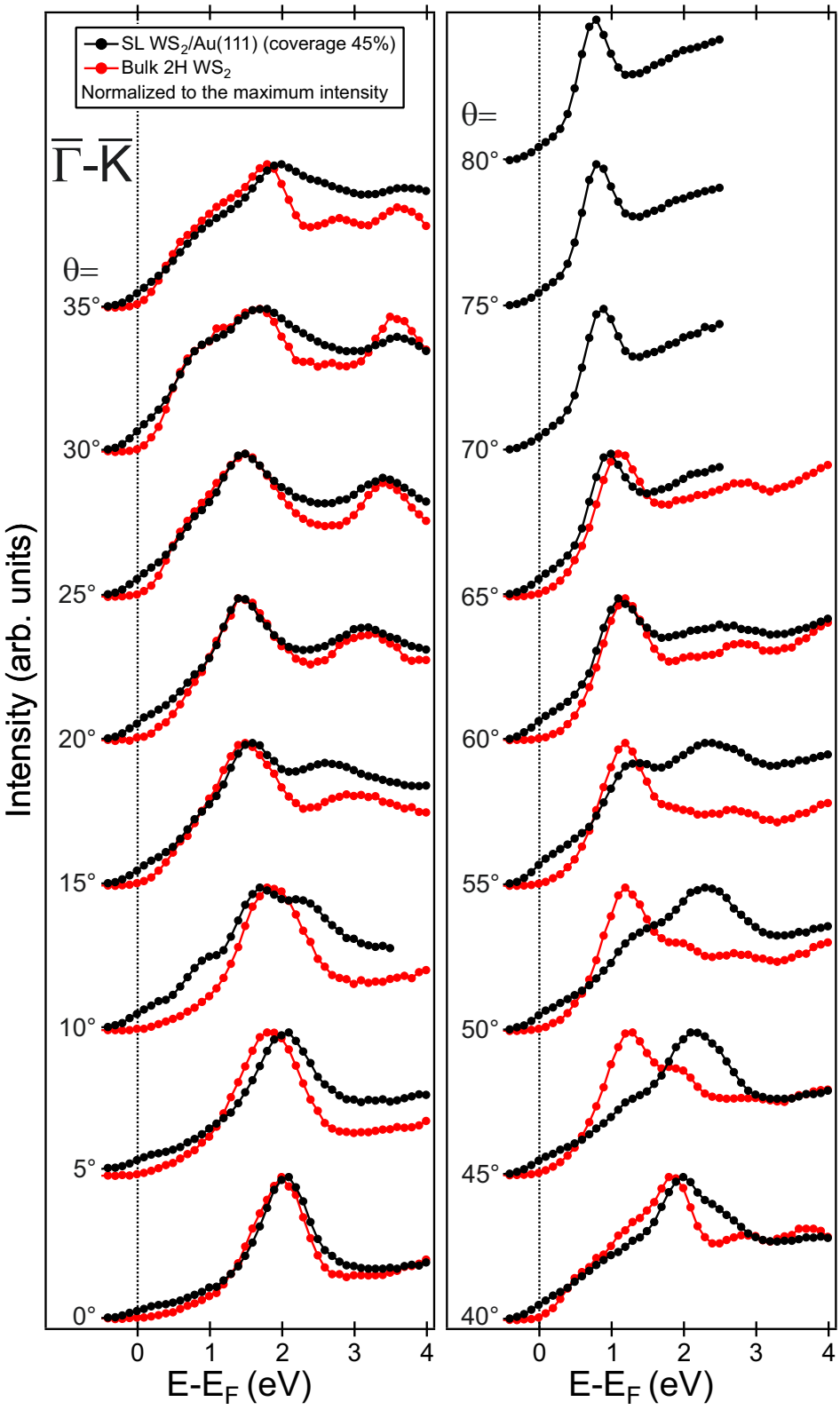

Figure 5.10: IPE spectra of bulk WS_2 and SL WS_2/Au(111) along $\overline{\Gamma}$-$\overline{K}$. Spin-integrated data are shown as black dots (red dots) for SL WS_2/Au(111) (bulk WS_2). The spectra are normalized to the maximum intensity.

Secondly, areas in **k**-space with and without pronounced hybridization of electronic states are identified. The spectra can be divided into several groups, according to different areas in **k**-space.

(a) For $\theta \leq 15^\circ$ (close to $\overline{\Gamma}$), no projected bulk bands of Au(111) are present. Hence, no influence on the band dispersion of WS_2 is expected. Indeed, the spectra for $\theta = 0^\circ$ are almost identical. With increasing angle of electron incidence, more and more differences between corresponding spectra occur. Most notably, the background in the case of SL WS_2/Au(111) is stronger and the relative energy between the features is slightly different. The bulk and SL data for $20^\circ \leq \theta \leq 30^\circ$ are still of a similar shape, despite probing in an area of **k**-space with surface-projected bulk bands of Au(111).

(b) Major differences between the bulk and the SL data for $35^\circ \leq \theta \leq 55^\circ$ are observed with respect to the intensity and the shape of the observed features. Here, the the SL spectra are strongly influenced by the Au(111) substrate. This is particularly the case for spectra corresponding to an area close to the Q point in **k**-space, i.e. $\theta = 45^\circ$ and $\theta = 50^\circ$.

(c) Remarkably, when approaching $\overline{\mathrm{K}}$ (for $\theta \geq 60^\circ$), the two data sets become once again similar in shape and absolute intensity, especially for the feature corresponding to the lowest CB. This is not necessarily expected, since $\theta \geq 60^\circ$ corresponds to $k_{||} \approx 1.1\text{Å}^{-1}$, i.e. an area in **k**-space with surface-projected bulk bands of Au(111). The SL WS_2 spectra show sharp features for $\theta \geq 60^\circ$, while hybridized electronic states are often blurred in energy and hence appear broader.

The experimental results indicate a comparable electronic structure of bulk 2H WS_2 and SL WS_2/Au(111) close to $\overline{\mathrm{K}}$, particularly for the lowest CB. Consequently, a negligible influence of the Au(111) substrate on the dispersion of the lowest CB of WS_2 around $\overline{\mathrm{K}}$ is expected. This also supported by calculations that indicate no influence of the Au(111) substrate on SL WS_2 band energies in the case of the lowest CB for $k_{||} \geq 1.2\text{Å}^{-1}$ (see Fig. 5.5). Therefore, the analysis of the electronic and spin structure around $\overline{\mathrm{K}}$ in the subsequent section, resembles the properties of freestanding SL WS_2.

5.2.3 Spin Structure of the K Valleys

Spin-resolved experimental data are so far only available for the VBs of single-oriented MoS_2 on Au(111) (Bana *et al.*, 2018). This spin-resolved ARPES study finds out-of-plane spin-polarized VBs with opposite sign at the $\overline{\mathrm{K}}$ and $\overline{\mathrm{K}}'$ points. An equivalent spin texture in the VB is expected for WS_2 (Zhu *et al.*, 2011; Xiao *et al.*, 2012; Li *et al.*, 2015; Tatsumi *et al.*, 2016).

Figure 5.11 shows spin-resolved ARPES measurements for SL WS_2/Au(111) at $\overline{\mathrm{K}}$ and $\overline{\mathrm{K}}'$. Purple and yellow dots denote data for electron spin polarization parallel and antiparallel to the surface normal, respectively. The VBM is found at $E-E_\mathrm{F} = -1.29 \pm 0.02\,\mathrm{eV}$ and $-1.71 \pm 0.01\,\mathrm{eV}$ for the two spin directions. The results reveal a spin-dependent energy splitting ΔE_VB of $417 \pm 19\,\mathrm{meV}$. This value is in good agreement with the value that is extracted from the calculation presented in figure 5.5 (431 meV) and other theoretical predictions (Zhu *et al.*, 2011; Ramasubramaniam, 2012; Kosmider *et al.*, 2013; Liu *et al.*, 2013; Ye *et al.*, 2014; Kormányos *et al.*, 2015). The same size of the splitting was obtained in spin-integrated measurements for SL WS_2 on different substrates (Dendzik *et al.*, 2015; Ulstrup *et al.*, 2016a; Dendzik *et al.*, 2017) as well as on bulk samples (Latzke *et al.*, 2015). Other references report slightly higher values (Yuan *et al.*, 2016; Forti *et al.*, 2017) for unknown reasons. The independence of the substrate is expected as the HVB of SL WS_2 lies well within a projected bulk band gap (Dendzik *et al.*, 2015).

Remarkably, the two oppositely spin-polarized VB features (in the data for both $\overline{\mathrm{K}}$ and $\overline{\mathrm{K}}'$) show almost 100% spin polarization above background. The observed spin polarization is caused by the spin-polarized bands and not by extrinsic spin polarization effects. The latter are generated by matrix-element effects based on orbital contributions as well as experimental parameters and geometry (Donath, 2018; Henk *et al.*, 2018). Extrinsic spin-polarization effects can be ruled out by the following experimental finding: in the same experimental geometry with only the sample rotated azimuthally by $\phi = 60^\circ$, completely spin-polarized features are obtained at $\overline{\mathrm{K}}$ and $\overline{\mathrm{K}}'$, yet with reversed sign. These observations are only possible, if two conditions are met. (i) the SL film has one single orientation, thus confirming the XPD results (Bignardi *et al.*, 2019), and (ii) the bands at the Brillouin-zone boundary are intrinsically spin polarized.

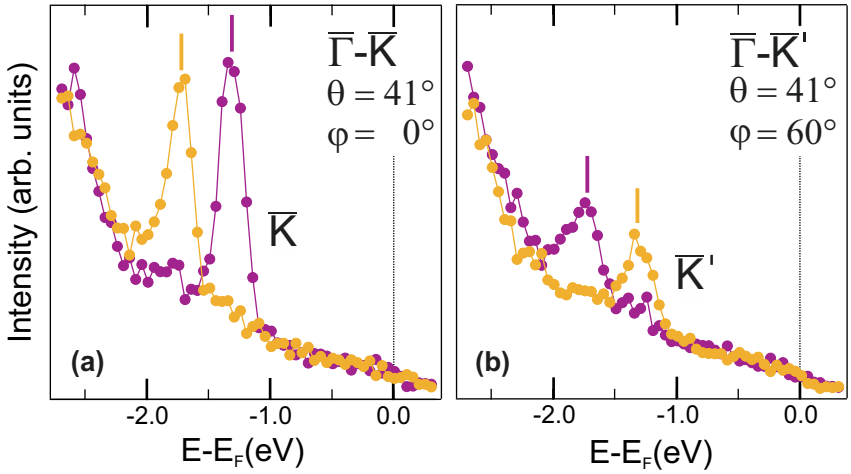

Figure 5.11: Spin-resolved ARPES spectra (out-of-plane spin sensitivity) of the uppermost VBs at the $\overline{K}$ (a) and $\overline{K}'$ (b) points. The spin splitting of the HVB ΔE_{VB} is determined to 417 ± 19 meV.

The key question with respect to the $\overline{K}/\overline{K}'$ valleys is the size of the energy gap and its spin structure. Using the SARPES results of this section together with SRIPE results shown in section 5.2.1, the size of the energy gap is determined to 1.98 ± 0.04 eV. Quasiparticle calculations predict the band gap of freestanding SL WS_2 in the range between 2.7 eV and 2.88 eV (Ding *et al.*, 2011; Ramasubramaniam, 2012; Liang *et al.*, 2013; Shi *et al.*, 2013; Kormányos *et al.*, 2015). The determined band gap for $WS_2/Au(111)$ is significantly lower due to the enhanced screening of the Au substrate, as reported also for $MoS_2/Au(111)$ (Bruix *et al.*, 2016). Interestingly, a band gap of similar size (2.0 eV) was found for $WS_2/Ag(111)$ by time-resolved ARPES (Ulstrup *et al.*, 2017).

To extract the spin structure of the unoccupied $\overline{K}/\overline{K}'$ valleys, the figures 5.12 and 5.13 show close-ups of SRIPE data in figure 5.4 for $\theta = 75°$ and $\theta = 80°$ along $\overline{\Gamma}$-$\overline{K}$ as well as data close to $\overline{K}'$ ($\theta = 70°$) to check the sign reversal of the spin signal.

The peak positions for spin-up and spin-down differ only slightly. Since the two partial spin spectra are measured separately, spin splittings can be resolved that are much smaller than the energy resolution or the intrinsic line width of the spectral features. In the case of completely spin-polarized states, the spin splitting can be determined quantitatively even in the case of energetically overlapping

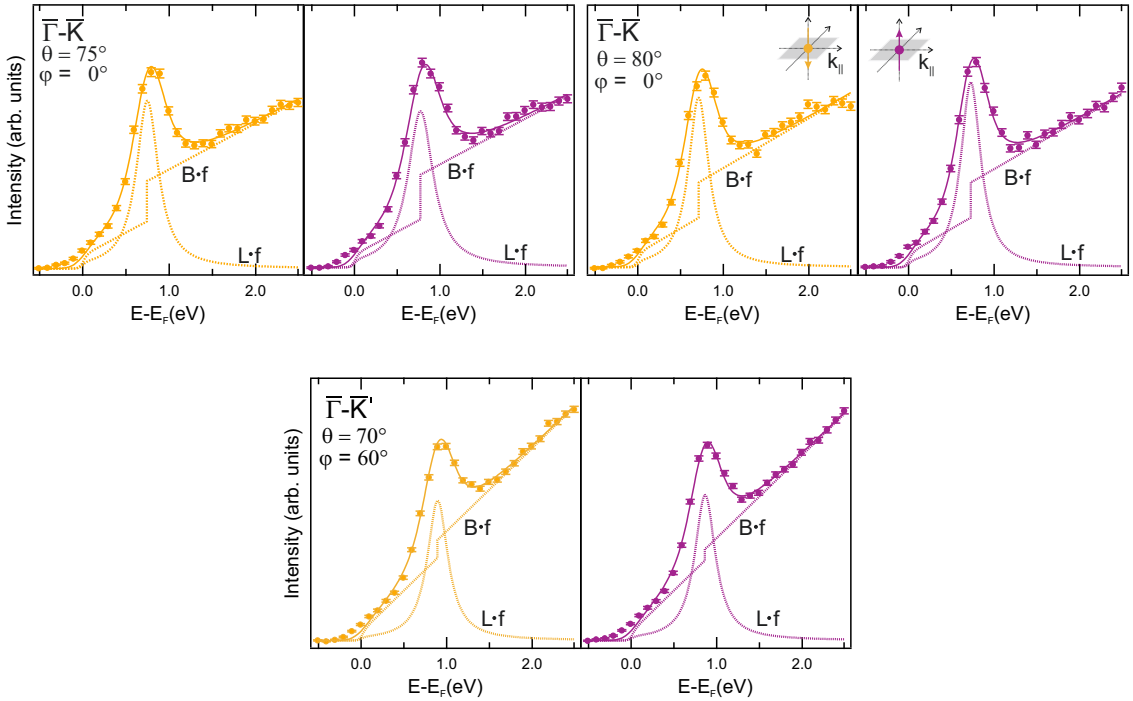

Figure 5.12: SRIPE spectra for out-of-plane spin sensitivity in the vicinity of the $\overline{\mathrm{K}}$ and $\overline{\mathrm{K}}'$ points together with the fit components: $B \cdot f$ ($L \cdot f$) denotes the background (Lorentzian function) multiplied by the Fermi distribution. The background consists of a linear function with a step function at the position of L (see text for details).

states. Otherwise, the obtained value is at least a lower limit. Based on the results for the VBs, it is reasonably assumed that the CBs are completely spin polarized as well. Nevertheless, the effect of an incomplete spin polarization can be estimated and will be treated later in this section. For the same reasons as discussed for the SARPES results, extrinsic spin polarization effects are excluded for the SRIPE results.

To extract the spin-dependent peak positions and the resulting spin splittings, the individual spin spectra are fitted separately. The spectra for $\theta \geq 65°$ in figure 5.4 show one dominant spectral feature on an almost linearly increasing background. Therefore, the fit functions F consist of a Lorentzian function L on a background B, multiplied by the Fermi distribution f at room temperature for unoccupied states. The result is then convoluted with the apparatus function A, which is approximated by a Gaussian function with FWHM of 350 meV.

Table 5.2: Test of stability and reliability of the fitting routine. Spin-dependent energy positions of L and spin splittings for models A, B, C, and D for the three different data sets of figure 5.13.

Fit model	$E_\uparrow$ (meV)	$E_\downarrow$ (meV)	$\Delta E_{\uparrow\downarrow}$ (meV)
75° $\overline{\Gamma}$-$\overline{K}$			
Model A	773.4	747.5	25.9
Model B	779.6	753.3	26.3
Model C	773.4	747.5	25.9
Model D	793.5	770.6	22.8
80° $\overline{\Gamma}$-$\overline{K}$			
Model A	727.5	711.5	16.0
Model B	732.3	716.9	15.4
Model C	727.5	711.5	16.0
Model D	749.3	738.0	11.3
70° $\overline{\Gamma}$-$\overline{K'}$			
Model A	864.5	895.3	-30.8
Model B	865.3	896.2	-30.9
Model C	864.5	896.2	-31.7
Model D	870.6	902.7	-32.1

The background B consists of a spin-independent constant part due to dark counts of the photon detectors plus an energy- and spin-dependent part due to secondary processes, mainly caused by electron scattering creating an electron-hole-pair preceding the optical transition. The exact shape of the latter part of the background intensity is difficult to model. A simple approach assumes random **k** approximation and constant transition probabilities in the case of angle-integrated measurements, which leads to model calculations based on the denstiy of states (Dose and Reusing, 1980) (see also model calculations in Passek *et al.* (1995)). In the case of **k**-resolved measurements, however, the random **k** approximation has to be questioned. Obviously, the linear background above the peak energy is higher than the extrapolation of the linear background below the peak energy. This reflects the increase of the density of states at the CBM of WS_2. Therefore, this background increase is modeled by a step function. Four different models have been tested to model the background B:

- Model A: Lorentzian function L, linear background (spin-independent slope) with a spin-dependent step-like increase at the position of L.
- Model B: One might argue that the step-like background increase due to the onset of the density of states at the CBM is better described by an integral over the peak L. Therefore, a broadened step function is tried to account for that.
- Model C: Same as Model A but with a spin-independent position of the step-like background increase.
- Model D: In addition, the influence of the energy position of the step function is tested. The step function is shifted to 0.2 eV higher energy for both individual spin spectra.

It is reasonable to assume the energy position of the step function to be spin dependent because the CBM is spin dependent. Therefore, the results discussed in the text and in figure 5.13 are based on an analysis utilizing model A. While the different models result in different absolute peak positions (see Tab. 5.2 and Fig. A.10), the spin splittings are reliable within the uncertainty intervals of model A (see Fig. 5.13).

The individual components for the fitting procedure (model A) to extract the peak positions are presented in figure 5.12. The fits show good agreement with the data except for a systematic deviation in the energy region around the Fermi energy. Here, the spectra are influenced by the density of states of the Au substrate. Note that the inverse-photoemission data of bulk WS_2 samples (see Fig. 5.7 in Sec. 5.2.2) do not exhibit this intensity at the Fermi level. Additional functions (and fitting parameters) in the fitting procedure, necessary to model this substrate-induced intensity, does not make the fitting more conclusive because the peak position of L is energetically well separated from the energy region around E_F.

To ensure the reliability of the analysis not only the fit procedure has to be tested. Two additional factors are important for the quantitative analysis.

(i) The spin-polarization uncertainty of the the spin-polarized electron beam in SRIPE is evaluated. The analysis (see appendix A.8) has been done for an assumed electron-beam spin polarization P of 26, 29, and 32% to consider the uncertainty of the electron source used in this thesis with $P = 29 \pm 3\%$.

The spin splitting for $\theta = 80°$ along $\overline{\Gamma} - \overline{K}$ changes by ± 2 meV, while for $\theta = 70°$ along $\overline{\Gamma} - \overline{K'}$ the change is ± 3 meV. The above determined uncertainties of the spin splittings have a negligible effect on the uncertainty margins of ± 7 meV and ± 6 meV for $\theta = 80°$ along $\overline{\Gamma}$-$\overline{K}$ and $\theta = 70°$ along $\overline{\Gamma}$-$\overline{K}'$, respectively.

(ii) The influence of possibly not completely spin polarized states, i.e., each individual spin spectrum contains a two-peak structure with different intensities for the two peaks, is tested.

Consistent with the observed fully spin-polarized VBs, a first principle calculation (Krüger, 2018) results in a spin polarization of 99.9% (98.7 %) for the highest (second highest) VB. The spin polarization of the CBs is calculated to be 88.7% (97.5%) for the lowest (second lowest) CB. The influence of possibly incompletely spin-polarized CBs is examined by assuming an even lower value than calculated for the CBs. For an assumed spin polarization as low as 80% instead of 100%, the two peaks would have an intensity ratio of 9:1.

While it is not possible to use the peak splitting as a free parameter in the fit routine due to the overlapping states, one can estimate the outcome. Fitting the peak with two Lorentzians, e.g., a dominant part at lower energy and a minor part at higher energy, shifts the peak energy of the dominant part to lower energies compared with the fit with only one Lorentzian. Vice versa, in the other individual spin spectrum, the peak energy of the dominant part is shifted to higher energy. As a consequence, the derived spin splitting will be larger if the spin polarization of the CB is not 100%. This was tested with a fit to the data with a given but variable peak splitting ΔE_{CB} for both individual spin spectra. The result is consistent with the expectation: The energy difference between the dominating peaks in the two individual spin spectra was slightly larger (≈ 3 meV, data for $\theta = 80°$) than the spin splittings obtained from a fit with one Lorentzian function. As a result, the spin splittings derived from a fit with one Lorentzian is a lower limit as mentioned before. However, any reasonable assumption of the conduction-band spin polarization will only slightly enhance the spin splitting.

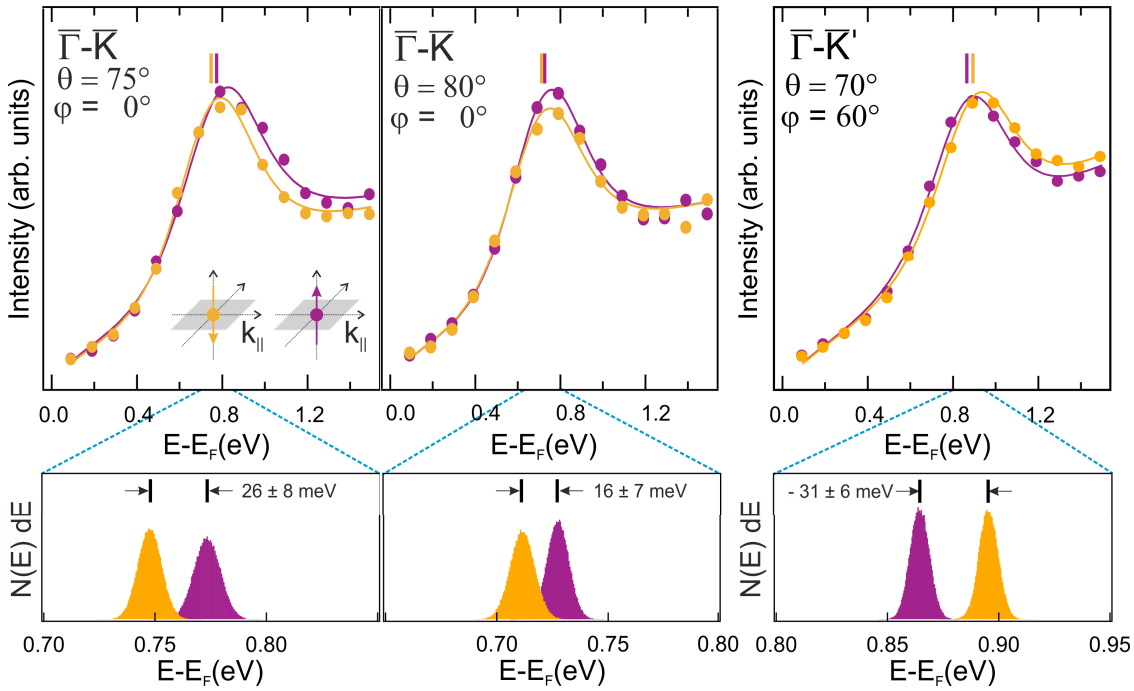

Figure 5.13: Spin- and angle-resolved inverse-photoemission spectra for out-of-plane spin sensitivity in the vicinity of the $\overline{\mathrm{K}}$ and $\overline{\mathrm{K}}'$ points. Vertical lines mark the spin-dependent peak positions of the lowest CB. The lower panels show peak position distributions $N(E)dE$ of the CB emissions, obtained from least-squares fitting procedures (see text for details). Solid lines indicate the fit functions.

To quantify spin splittings and illustrate the statistical uncertainties, an approach is used that was reported earlier in the literature (Passek and Donath, 1992; Donath and Ertl, 1992; Passek *et al.*, 1995). For each spectrum, a series of 100,000 pseudo-experimental spectra is generated by varying each measured data point according to its statistical uncertainty. All these pseudospectra are fitted with the described fitting functions and the obtained peak positions are collected in a histogram. The histogram showing the peak position distribution $N(E)dE$ is a direct measure of the most probable peak position and its uncertainty. These distributions are displayed in the lower panels of figure 5.13 and figure A.11. For $\theta \geq 60°$, all spectra along $\overline{\Gamma}$-$\overline{\mathrm{K}}$ exhibit a spin splitting with the same sign (see Fig. 5.4). An important test is the measurement on the azimuthally by 60° rotated sample: The data for $\theta = 70°$ along $\overline{\mathrm{K}}'$ show also a clear spin splitting, yet with reversed sign (see right panel of Fig. 5.13)

The extracted spin splitting values are a few tens of meV, decreasing from 31±6, 26±8 to 16±7 meV upon approaching the zone boundary for electron incidence angles of 70, 75, and 80°, respectively. The experimental value of $\Delta E_{\mathrm{CB}} = 16\pm7$ meV is slightly lower than calculated CB splitting. The calculation shown in figure 5.5 obtained 29 meV in good agreement with other calculations (26 meV to 32 meV (Zhu *et al.*, 2011; Kosmider *et al.*, 2013; Liu *et al.*, 2013; Kormányos *et al.*, 2015)).

An essential information is the spin sequence of the valence and CBs. The SARPES and SRIPE data for WS_2 show that they are spin split in the same way. In other words, the HVB is oppositely out-of-plane spin-polarized with respect to the lowest CB as sketched in figure 5.14 (a). Thus, the first spin allowed (bright) transition is 16 meV higher in energy than the first dark transition.

The experimental value for ΔE_{CB} and the respective spin sequence is important for theoretical studies, trying to determine the energy difference $\Delta E_{\mathrm{Bright\text{-}Dark}}$ between dark and bright excitons (Echeverry *et al.*, 2016). In theoretical models $\Delta E_{\mathrm{Bright\text{-}Dark}}$ is influenced most prominently by ΔE_{CB} and in addition by the electron-hole interaction within the exciton. A few studies report on "brightening" the spin-forbidden dark excitons in WSe_2 (Zhou *et al.*, 2017; Zhang *et al.*, 2017) and $MoSe_2$ (Quereda *et al.*, 2018) by various methods. For SL WS_2, a splitting between dark and bright exciton $\Delta E_{\mathrm{Bright\text{-}Dark}} = 47$ meV was reported from a photoluminescence experiment under the influence of an in-plane magnetic field (Molas *et al.*, 2017). While the lower energy of the dark exciton is consistent with the results of this thesis, $\Delta E_{\mathrm{Bright\text{-}Dark}}$ is much larger than ΔE_{CB}. For SL WS_2, the contribution of the electron-hole interaction is calculated to be in the order of 20 meV (Echeverry *et al.*, 2016) partially explaining the difference between ΔE_{CB} and $\Delta E_{\mathrm{Bright\text{-}Dark}}$.

5.3 Conclusion

In conclusion, the occupied and unoccupied electronic structure of SL WS_2 on Au(111) was studied experimentally by spin-resolved direct and inverse photoemission and theoretically by calculations for the freestanding SL and a SL adsorbed on Au(111). The total energy gap amounts to 1.98 ± 0.04 eV, influenced by the screening of the Au substrate.

A schematic band structure at the $\overline{K}$ and $\overline{K}'$ points, summarizing the results about the spin-dependent energy gap, is sketched in figure 5.14. The VBM is found to be spin split by 417 ± 23 meV, the CBM by 16 ± 7 meV. The sequence of the spin-split bands is the same below and above the Fermi level, i.e. the VBM is oppositely out-of-plane spin-polarized than the CBM. As a consequence, the lowest transition is spin forbidden, i.e., optically dark. The first bright transition, involving the second CB, is 16 meV higher in energy than the band gap.

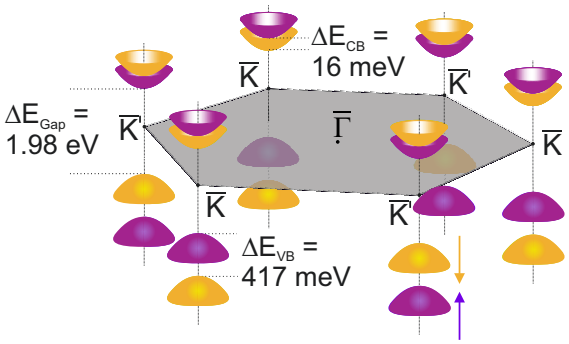

Figure 5.14: Sketch of the spin-dependent valley structure of the bands in single-layer WS_2, giving a summary of the obtained results.

The Au(111) substrate has little or no influence on the spin structure and dispersion of the LCB close to $\overline{K}$ as indicated by calculations and comparative measurements of bulk WS_2. As a consequence, the energy-dependent spin structure of the VBM and the CBM at the $\overline{K}/\overline{K}'$ valleys, studied in the present work, reflects the properties of undisturbed SL WS_2. Therefore, the results clarify important questions regarding band dispersion and spin structure of SL WS_2 with its promising valleytronic properties for future optoelectronic applications.

6

Summary

$ReSe_2$ and SL WS_2 are considered as highly promising candidates for future electronic devices due to their unique respective optoelectronic properties that are based on the underlying electronic structure. $ReSe_2$ is a low-symmetric material with anisotropic properties. The non-centrosymmetric SL WS_2 stands out with its spin-dependent VBM and CBM that provide a way for the spin and valley degrees of freedom to be utilized in future devices. The present thesis examines the anisotropic electronic structure of bulk $ReSe_2$ and quantifies the spin-dependent properties of the VBM and CBM in SL WS_2.

Anisotropic electronic structure of bulk $ReSe_2$

- SARPES measurements showed a remarkably high spin polarization of photoelectrons of up to 50% without background subtraction. DFT calculations indicate together with ARPES and SARPES measurements along $\overline{\Gamma}$-$\overline{M}_1$ the existence of a spin-polarized SS. However, the majority of the observed spin-polarization effects is caused by the photoemission process. Due the low symmetry of $ReSe_2$, spin polarization is observed for all possible directions of the spin-polarization vector.

- Photon-energy-dependent ARPES reveal two VBM with indistinguishable energy by studying the k_z-dependent band dispersion. One of them is located at the Z point, where the *GdW* calculation predicts the direct band gap. The other VBM appears at a non high-symmetry point in **k**-space along $\overline{\Gamma}$-$\overline{M}_1$.

- An IPE study provides **k**-resolved experimental data about the CBs. Consistently with band structure calculations, the band gaps in **k**-space are identified. The lowest observable CB is found at and energy of 0.93 eV at $\overline{\Gamma}$, i.e. the projection of the Γ - Z line. Considering the VBM at Z, the resulting band gap at $\overline{\Gamma}$ is 1.33 eV. A comparison of angle-integrated experimental data with the calculated DOS indicates the fundamental band gap energy to be lower than the determined band gap at $\overline{\Gamma}$. Therefore, the controversial (Marzik *et al.*, 1984; Ho *et al.*, 2001; Ho and Huang, 2004; Arora *et al.*, 2017) question about type and size of the band gap could not be fully clarified.

- An anisotropic E vs $\mathbf{k}_{\parallel}$ dispersion of the VBs is observed, with the direction perpendicular to the "diamond chains", i.e. $\overline{\Gamma}$-$\overline{M}_1$, being a distinct direction in **k**-space. The HVB dispersion in this direction has band width much smaller than in any other direction.

Spin-dependent electronic structure of SL WS_2

- The occupied and unoccupied electronic structure of SL WS_2/Au(111) is studied experimentally by SARPES and SRIPE. The total energy gap amounts to 1.98 ± 0.04 eV, influenced by the screening of the Au substrate.

- In areas of surface-projected Au bands, the experimentally determined CB dispersion of SL WS_2/Au(111) deviates from the calculated dispersion of a freestanding SL WS_2. Unexpectedly, a feature within the first eV above E_F is observed around $\overline{\Gamma}$. The feature is located well below the predicted bands of freestanding SL WS_2 and is in an area where no bulk Au bands exist. One possible explanation is the Shockley-SS of the Au(111) surface that is potentially modified by the WS_2 adsorbate. Therefore, the results of the present thesis motivate future studies with different adsorbates on Au(111) in order to systematically study the interaction with the Shockley-SS. Importantly, the Au(111) substrate has little or no influence on the spin structure and dispersion of the LCB close to $\overline{K}$, as indicated by calculations and comparative measurements of bulk WS_2.

- The VBM is fully out-of-plane spin-polarized at $\overline{K}$. Consistently with the surface symmetry the SARPES data show a reversed fully out-of-plane spin

polarization of the VBM at $\overline{K}'$. A valley-dependent spin polarization is also observed for the LCB in the SRIPE experiment.

- The spin-dependent properties of the VBM and CBM are quantified with SARPES and SRIPE. The VBM is found to be spin split by 417 ± 23 meV, the CBM by 16 ± 7 meV. The sequence of the spin-split bands is the same below and above the Fermi level, i.e. the VBM is oppositely out-of-plane spin-polarized than the CBM. As a consequence, the lowest transition is spin forbidden, i.e., optically dark. The first bright transition, involving the second CB, is 16 meV higher in energy than the band gap.

The presented work revealed the highly promising electronic structure of two semiconducting TMDCs: bulk $ReSe_2$ and SL WS_2. The distinct properties of the electronic structure, particularly the anisotropy and the spin-dependence, makes these material appealing for future electronic and optoelectronic devices. Moreover, potential spintronic and valleytronic devices can utilize the spin and valley degrees of freedom of SL WS_2. Layered semiconducting TMDCs such as $ReSe_2$ and WS_2 are important materials for building new small-scale devices with high performance that pave the way for our future within the information age.

Zusammenfassung

$ReSe_2$ und SL WS_2 sind vielversprechende Kandidaten für zukünftige elektronische Bauelemente, weil sie einzigartige optoelektronische Eigenschaften besitzen. Diese basieren auf ihrer zugrunde liegenden elektronischen Struktur. $ReSe_2$ ist ein Material mit geringer Symmetrie und anisotropen Eigenschaften. Das nicht zentrosymmetrische, einlagige (SL) WS_2 zeichnet sich durch die Spinabhängigkeit des Valenzbandmaximums (VBM) und Leitungsbandminimum (CBM) aus. Diese Abhängigkeit ermöglicht die Ausnutzung des Spin- und „Valley"-Freiheitsgrades in zukünftigen Bauelementen. Die vorliegende Arbeit untersucht die anisotrope elektronische Struktur von volumenartigem $ReSe_2$ und quantifiziert die spinabhängigen Eigenschaften von VBM und CBM in SL WS_2.

Anisotrope elektronische Struktur von volumenartigem $ReSe_2$

- Spin- und winkelaufgelöste Photoemissions (SARPES) messungen zeigen eine bemerkenswert hohe Spinpolarisation der Photoelektronen von bis zu 50% ohne Abzug des Untergrundes. Bandstrukturrechnungen weisen zusammen mit ARPES- und SARPES-Messungen entlang $\overline{\Gamma}$-$\overline{M}_1$ auf die Existenz eines spinpolarisierten Oberflächenzustandes hin. Der Großteil der beobachteten Spinpolarisation ist jedoch durch den Photoemissionsprozess verursacht. Aufgrund der geringen Symmetrie von $ReSe_2$ wird Spinpolarisation entlang aller möglichen Richtungen des Spinpolarisationsvektor beobachtet.

- Die k_z-abhängige Band Dispersion wurde mit photonenenergieabhängigem ARPES untersucht. Es gibt zwei VBM mit ununterscheidbarer Energie. Eines liegt, wie von der *GdW* Rechnung als Teil der direkten Bandlücke vorhergesagt, am Z Punkt, während das andere sich an einem nicht hochsymmetrischen Punkt entlang $\overline{\Gamma}$-$\overline{M}_1$ befindet.

- Die Studie mit Inverser Photoemission (IPE) liefert **k**-aufgelöste experimentelle Daten über die Leitungsbänder (CB). In Übereinstimmung mit Bandstrukturrechnungen werden Bandlücken im **k**-Raum identifiziert. Das niedrigste beobachtbare CB ist bei einer Energie von 0.93 eV an $\overline{\Gamma}$ zu finden. $\overline{\Gamma}$ ist die Oberflächenprojektion der Γ - Z Linie. Berücksichtigt man das VBM an Z, folgt eine Bandlücke von 1.33 eV bei $\overline{\Gamma}$. Ein Vergleich winkelintegrierter experimenteller Daten mit der berechneten Zustandsdichte deutet auf eine geringere Energie der fundamentalen Bandlücke als 1.33 eV hin. Daher kann die kontroverse Frage über Größe und Art der Bandlücke (Marzik *et al.*, 1984; Ho *et al.*, 2001; Ho and Huang, 2004; Arora *et al.*, 2017) von $ReSe_2$ auf Grundlage der gewonnenen Daten nicht abschließend geklärt werden.

- Die $E(\mathbf{k}_{\parallel})$ Dispersion der Valenzbänder (VB) ist vollständig anisotrop. Die Richtung senkrecht zu den Zick-Zack-Ketten aus Re Atomen („diamond chains“) entspricht im **k**-Raum $\overline{\Gamma}$-$\overline{M}_1$ und ist eine besonders ausgezeichnete Richtung. Die Breite des energetisch höchstens VB ist in dieser Richtung deutlich schmaler als in allen anderen Richtungen.

Spinabhängige elektronische Struktur von SL WS_2

- Die besetzte und unbesetzte elektronische Struktur von SL WS_2/Au(111) wurde mit SARPES und SRIPE untersucht. Die fundamentale Energielücke beträgt (1.98 ± 0.04) eV und wird von der dielektrischen Abschirmung des Au-Substrates beeinflusst.

- In Bereichen mit oberflächenprojizierten Au Bändern weicht die experimentell bestimmte CB-Dispersion von SL WS_2/Au(111) von der berechneten Dispersion für eine freistehende Lage SL WS_2 ab. Unerwarteterweise wird in den Spektren eine Struktur innerhalb von einem eV oberhalb der Fermi-Energie um $\overline{\Gamma}$ herum beobachtet. Diese Struktur ist eindeutig von den vorhergesagten Bändern einer freistehenden SL WS_2 getrennt und befindet sich zudem in einem Bereich, in dem keine Au Zustände existieren. Eine mögliche Erklärung könnte der durch das WS_2 Adsorbat modifizierte Shockley-Oberflächenzustand (SS) der Au(111) Oberfläche sein. Die Ergebnisse dieser Arbeit motivieren daher weitere Studien mit unterschiedlichen

Adsorbaten auf der Au(111) Oberfläche um systematisch die Wechselwirkung zwischen Adsorbaten und dem Shockley-SS zu testen. Ein besonders wichtiges Ergebnis betrifft die Spinstruktur und Dispersion des niedrigsten CB nahe an $\overline{\mathrm{K}}$. Das Au(111) Substrat hat auf diese Eigenschaften nahe $\overline{\mathrm{K}}$ keinen signifikanten Einfluss, wie Rechnungen und Vergleichsmessungen mit volumenartigem WS_2 zeigen.

- Das VBM ist an $\overline{\mathrm{K}}$ vollständig senkrecht zur Probenoberfläche spinpolarisiert. SARPES Daten zeigen eine vollständige Spinpolarisation des VBM an $\overline{\mathrm{K}}'$ mit entgegengesetzter Richtung im Vergleich zu $\overline{\mathrm{K}}$. Dies deckt sich mit den Erwartungen aufgrund der Oberflächensymmetrie der Probe. Die „Valley"-abhängige Spinpolarisation ist mittels SRIPE ebenfalls für das niedrigste CB beobachtet worden.

- Die spinabhängigen Eigenschaften von VBM und CBM wurden mit SARPES und SRIPE quantifiziert. Das VBM ist spinaufgespalten mit einem Energieunterschied von (417 ± 23) meV, die Spinaufspaltung des CBM beträgt (16 ± 7) meV. Die Abfolge der spinaufgespaltenen Bänder ist unterhalb und oberhalb der Fermienergie identisch. Das bedeutet, das VBM ist entgegengesetzt spinpolarisiert zu dem CBM. Als Konsequenz ist der energetisch kleinste optische Übergang spinverboten und somit optisch dunkel. Der erste optisch helle Übergang ist mit dem zweiten CB möglich und benötigt somit eine um 16 meV höhere Energie als die fundamentale Bandlücke.

In der vorliegenden Arbeit wird die elektronische Struktur von volumenartigem $ReSe_2$ und SL WS_2, zweier halbleitender Übergangsmetall-Dichalcogenide, untersucht. Die spezifischen Eigenschaften ihrer elektronischen Struktur, insbeondere die Anisotropie und die Spinabhängigkeit, machen $ReSe_2$ und SL WS_2 zu vielversprechenden Materialien für zukünftige elektronische und optoelektronische Bauelemente. Zudem lassen sich Spin- und Valley-Freiheitsgrad für mögliche spintronische und valleytronische Bauelemente nutzen. Lagenartige, halbleitende Übergangsmetall-Dichalcogenide wie $ReSe_2$ und SL WS_2 sind wichtige Materialien, um neuartige, kleinformatige Bauelemente mit großer Leistungsstärke zu bauen. Diese sind wegbereitend für unsere Zukunft im Informationszeitalter.

Appendix

A.1 Experimentally Determined Occupied Electronic Structure of ReS_2

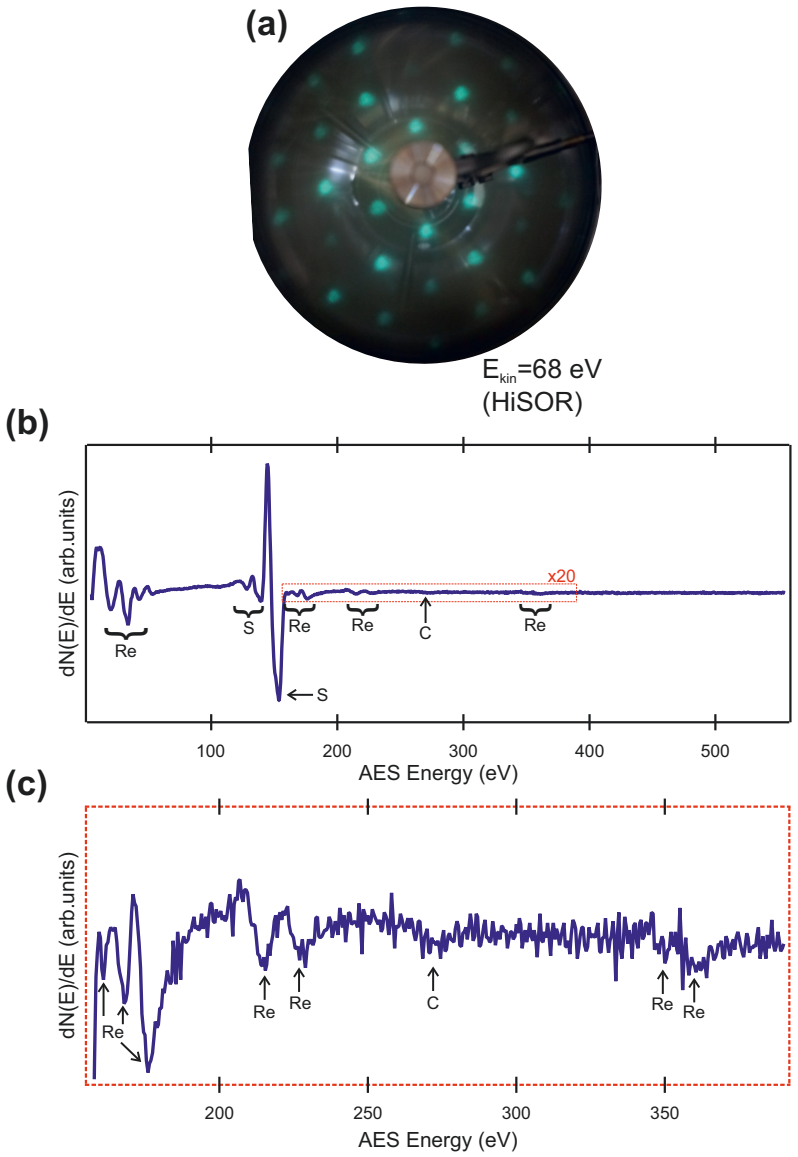

Figure A.1: (a) LEED pattern with $E = 68\,\text{eV}$, taken at BL-9B of HiSOR after (S)ARPES measurements. The screen was recorded manually with a camera. The foto is containing light reflections from outside the screen. (b) AES spectrum of ReS_2 taken after (S)ARPES measurements (excitation energy of 3 keV). The dashed box indicates the area that is presented in (c). Features are assigned according to (Davis *et al.*, 1976).

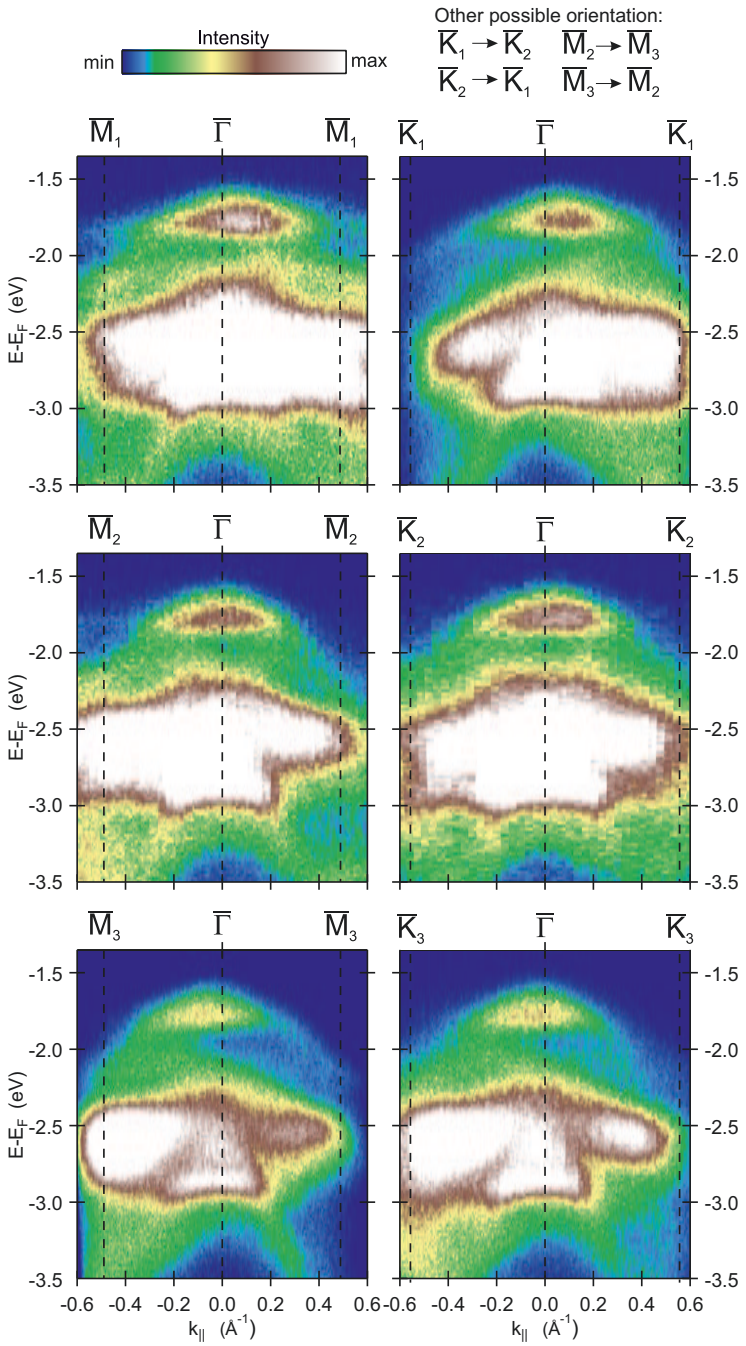

Figure A.2: ARPES measurements (hν=21 eV, p-pol. light) along high-symmetry directions of the SBZ shown in figure 4.1. In the case of ReS_2, the orientation of the BZ can, without further experimental information, not indisputably be determined (see discussion for $ReSe_2$). Therefore, both possible orientations are given in the figure.

A.2 SRIPE Spectra of $ReSe_2$ along $\overline{\Gamma}$-$\overline{M}_1$

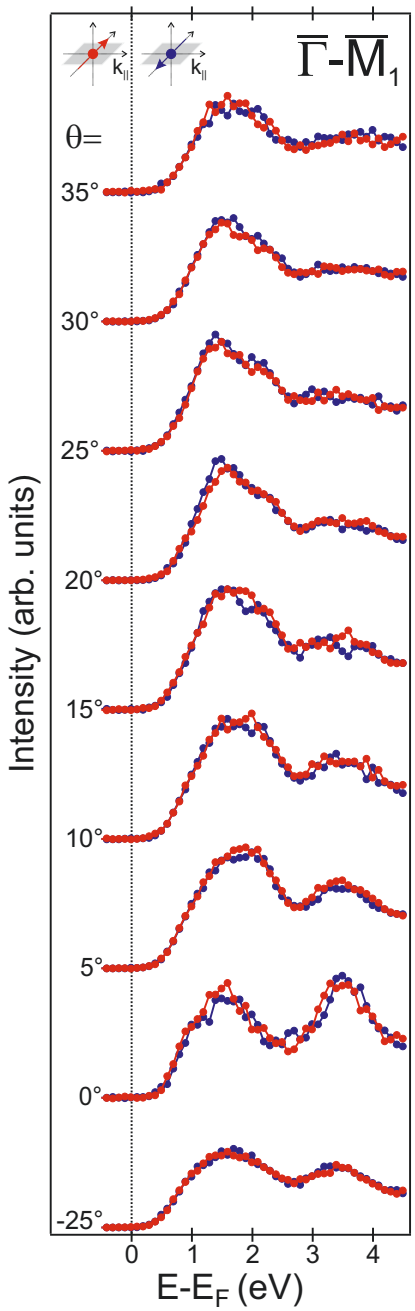

Figure A.3: SRIPE spectra of $ReSe_2$ along $\overline{\Gamma}$-$\overline{M}_1$. Spin-resolved data for $\mathbf{P}_y$ (Rashba) spin sensitivity are presented as blue and red dots with the respective orientation defined in the legend.

A.3 Comparison of MD and Single-Oriented SL WS_2/Au(111)

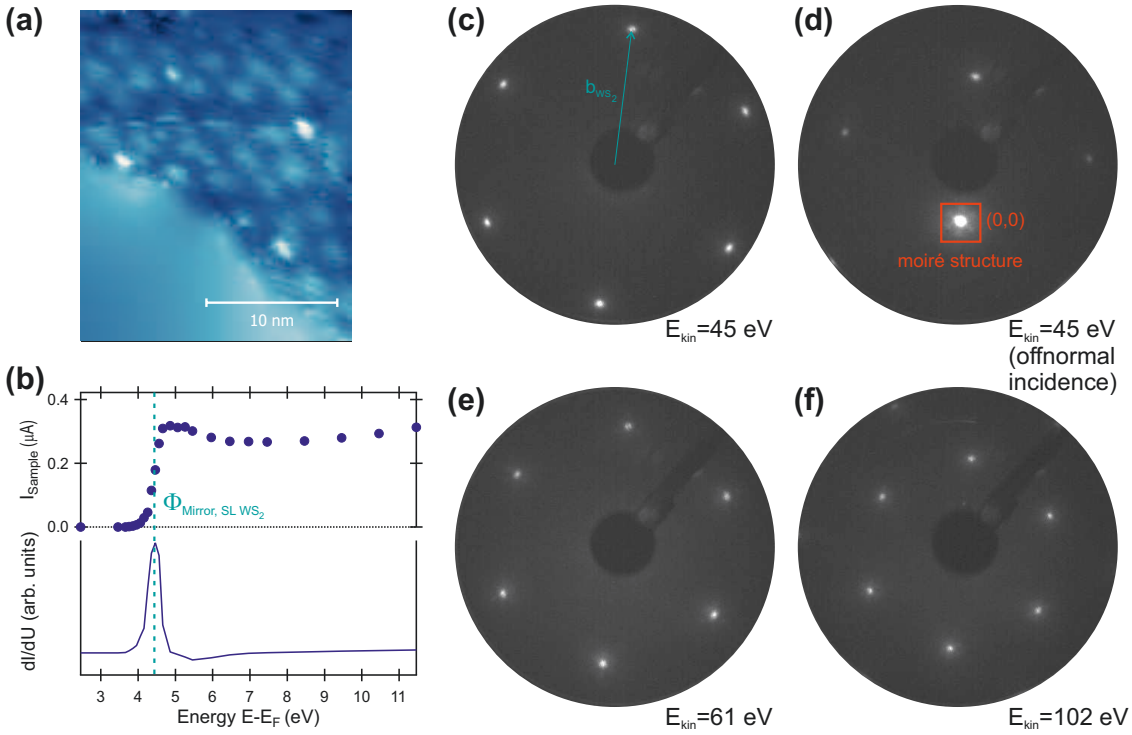

Figure A.4: (a) STM picture of the mirror-domain (MD) SL WS_2/Au(111) sample. (b) TCS spectra to determine the work function. (c) and (d) LEED pattern at $E = 45$ eV with normal and off-normal incidence geometry, respectively. The moiré structure is identified at the primary spot in (d) and is weaker than in the case of the single-oriented sample in figure 5.2. This is probably due to the occurrence of bilayers within the MD sample. (e),(f) LEED pattern with $E = 61$ eV and $E = 102$ eV. No threefold symmetry is observed at these energies. The results of MD SL WS_2/Au(111) in this figure have been gained in collaboration with Marcel Holtmann during his bachelor thesis (Holtmann, 2016).

The structure in real space is examined with STM. The STM study was performed in collaboration with M. Holtmann during his bachelor thesis (Holtmann, 2016) at a sample with a coverage of about a full SL that contains mirror domains with an almost equal ratio. The sample has roughly 20% of the area covered with bilayers (Sanders, 2016). In principle, spin-integrated IPE spectra of the two different samples must be comparable, yet with minor differences due to the different WS_2 coverage (and uncovered Au(111) areas) as well as the occurrence of bilayers that

have a slightly modified electronic structure. Indeed, spin-integrated IPE measurements indicate comparable surface quality (see Fig. A.6) and show just minor deviations, mostly in the background at higher energies. The incommensurability of the Au lattice (lattice constant of 2.88 Å) and WS_2 lattice (3.15 Å) leads to a modulation of the local density of states (Dendzik *et al.*, 2015). This results in the observed moiré pattern in the STM image in figure A.4 (a) with a periodicity of 32.0 ± 4.6 Å, consistent to values found in the literature (Dendzik *et al.*, 2015). The moiré structure is also identified in LEED in figure A.4 (d).

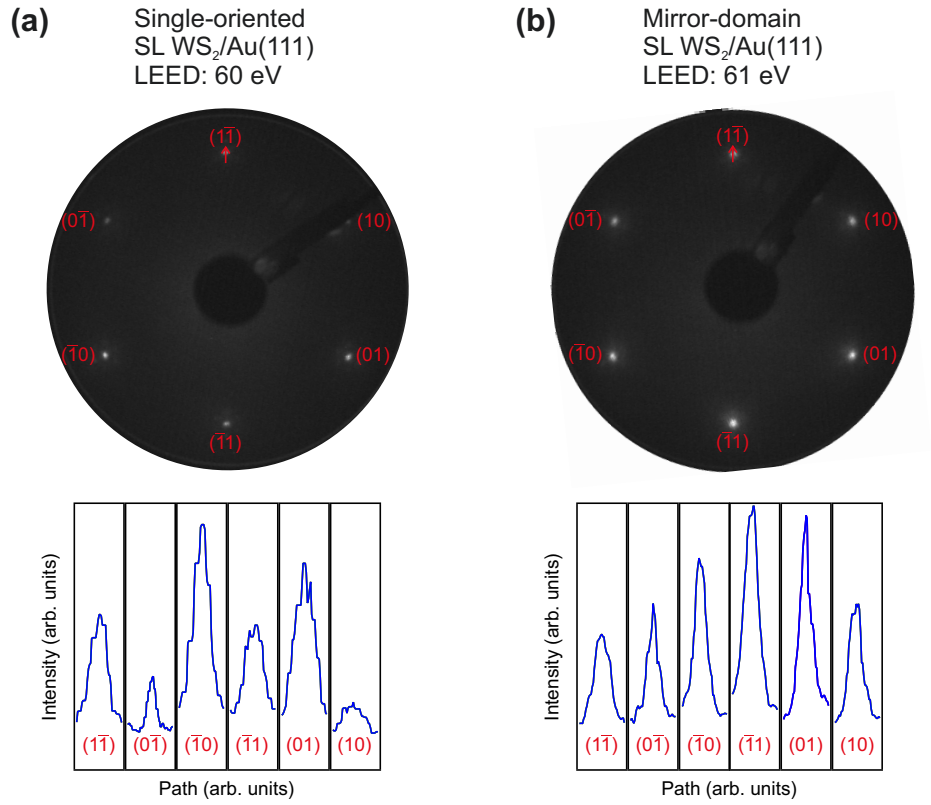

Figure A.5: Comparison of LEED images of single-oriented (a) and mirror domain (b) SL $WS_2/Au(111)$. The intensity profiles of the LEED spots are depicted in the lower panels. The pathes of the intensity profiles are oriented along the connection between the center of the LEED image and the respective spot. This is exemplarily shown for the $(1\bar{1})$ spot by the red arrow. The single-oriented SL $WS_2/Au(111)$ sample has a threefold symmetry, whereas this is not the case for the mirror domain sample. Note that misalignment of the LEED optics results in the three upper spots having low intensity in (b).

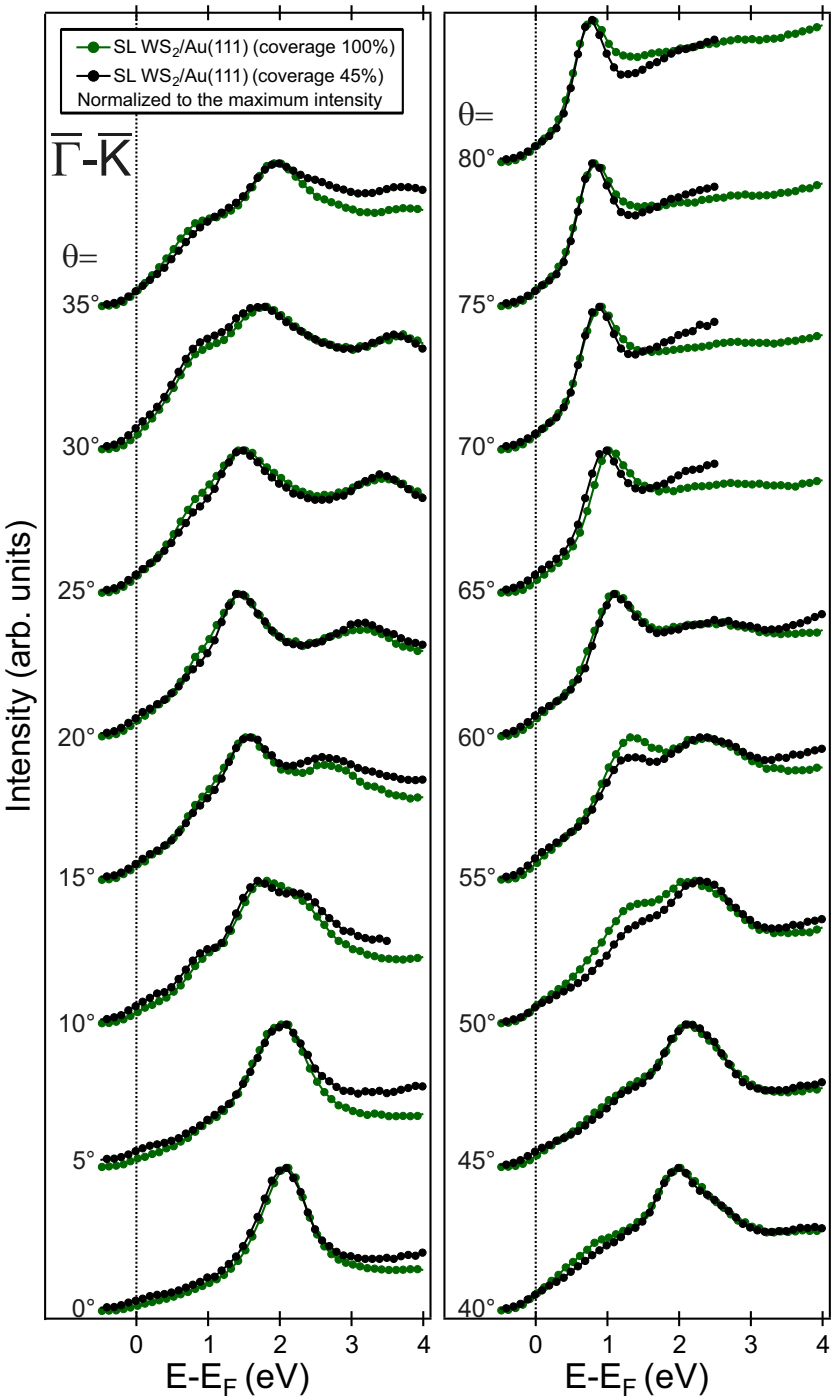

Figure A.6: IPE spectra of of SL WS_2/Au(111) (coverage 100%, mirror domains) and single-oriented SL WS_2/Au(111) (coverage 45%) along $\overline{\Gamma}$-$\overline{K}$. Spin-integrated data are shown as green and black dots. The spectra are normalized to the maximum intensity. The spectra with $\theta = 0°$, $\theta = 30°$ and $\theta = 55°$ of MD SL WS_2/Au(111) have been gained in collaboration with Marcel Holtmann during his bachelor thesis (Holtmann, 2016).

A.4 Comparison of SL WS_2/Au(111) with Bulk WS_2

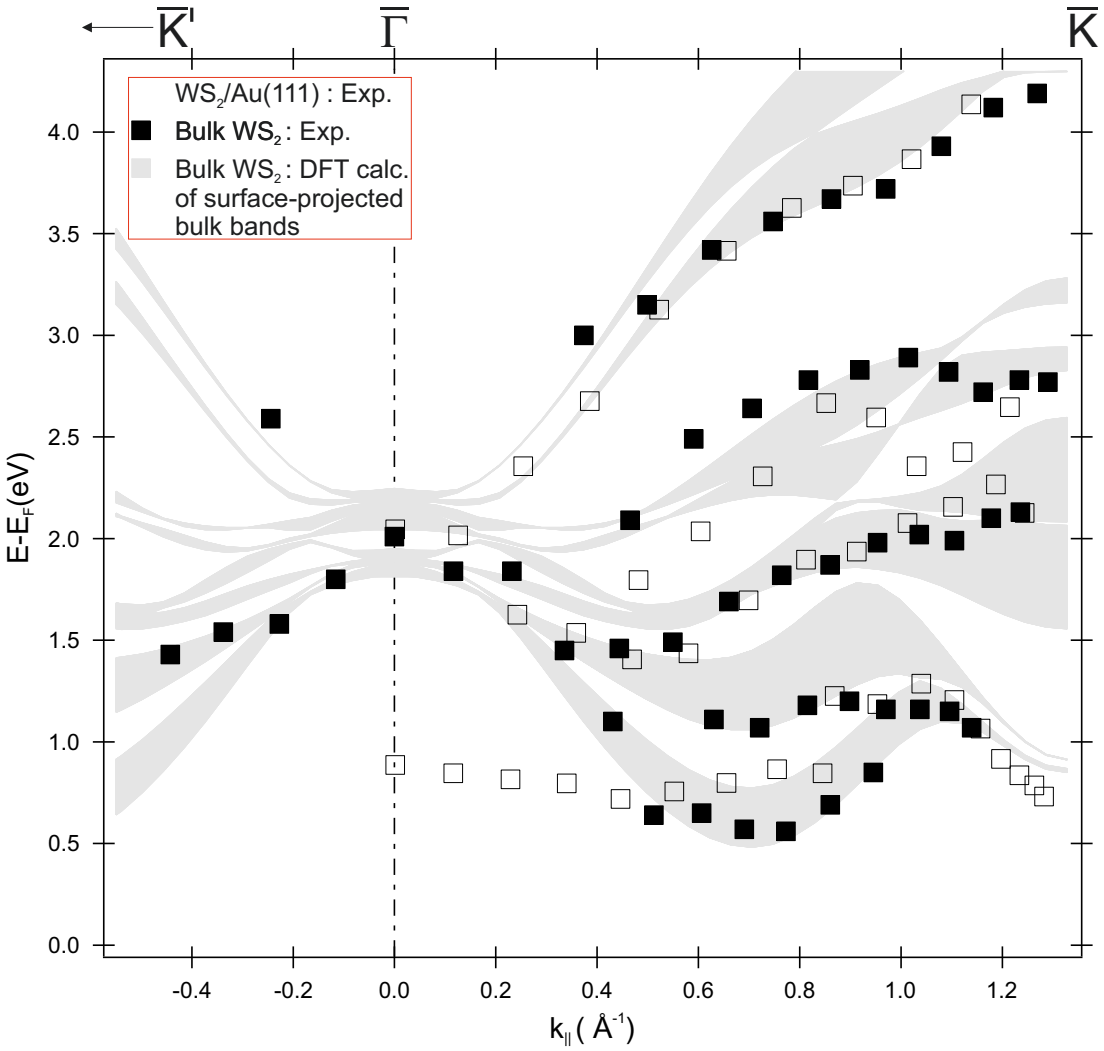

Figure A.7: Experimental E vs $\mathbf{k}_{\parallel}$ band dispersions along $\overline{\Gamma}$-$\overline{K}$. The experimental data of bulk WS_2 and SL WS_2/Au(111) are derived from the spectra in figure 5.7 and spin-integrated spectra belonging to figure 5.4, respectively. The positions are included as filled and open black squares for the bulk and SL material, respectively. The grey-shaded area is a result of a DFT calculation by Krüger (2018) and indicates surface-projected bulk bands of bulk 2H WS_2. The energy scale of the calculation is set accordingly to section 5.2.2. When comparing the respective energies of the SL and bulk material the following has to be considered. The respective energies are influenced by the size of the band gap and the doping level of the samples (compare Sec. 2.3).

A.5 Spin-Resolved IPE Spectra of Bulk WS_2

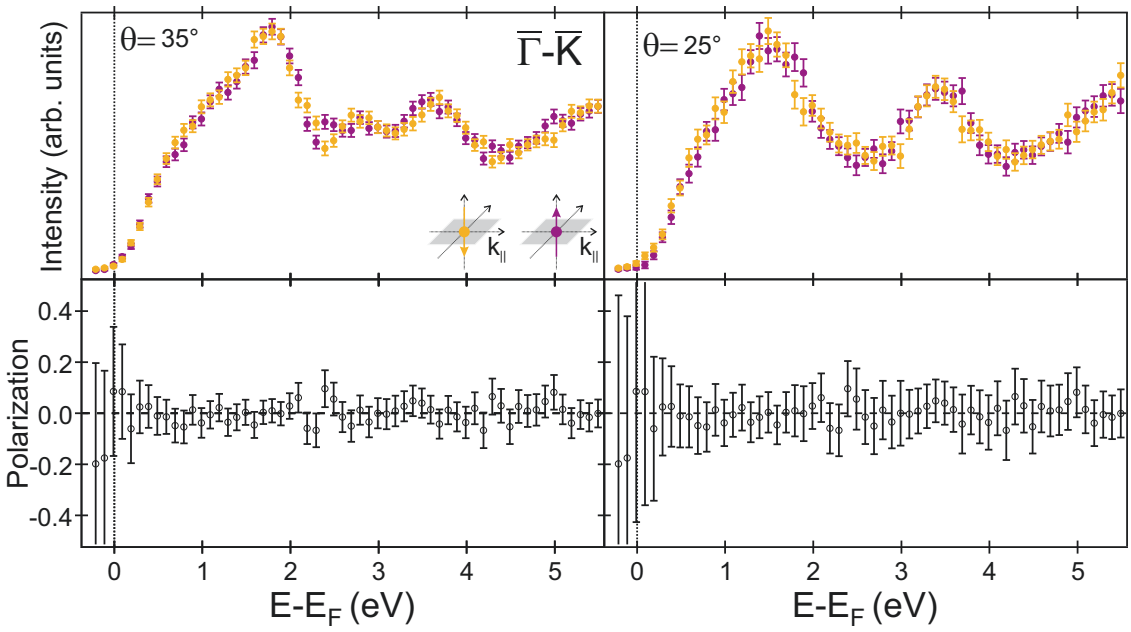

Figure A.8: SRIPE spectra of bulk WS_2, sensitive to the out-of-plane spin direction. The spectra correspond to the region around Q (halfway $\bar{\Gamma}$-$\bar{K}$). The lower panel shows the respective spin polarization P, as defined in section 3.1.2.

A.6 Comparison of Normalized IPE Spectra of All Different WS_2 Samples.

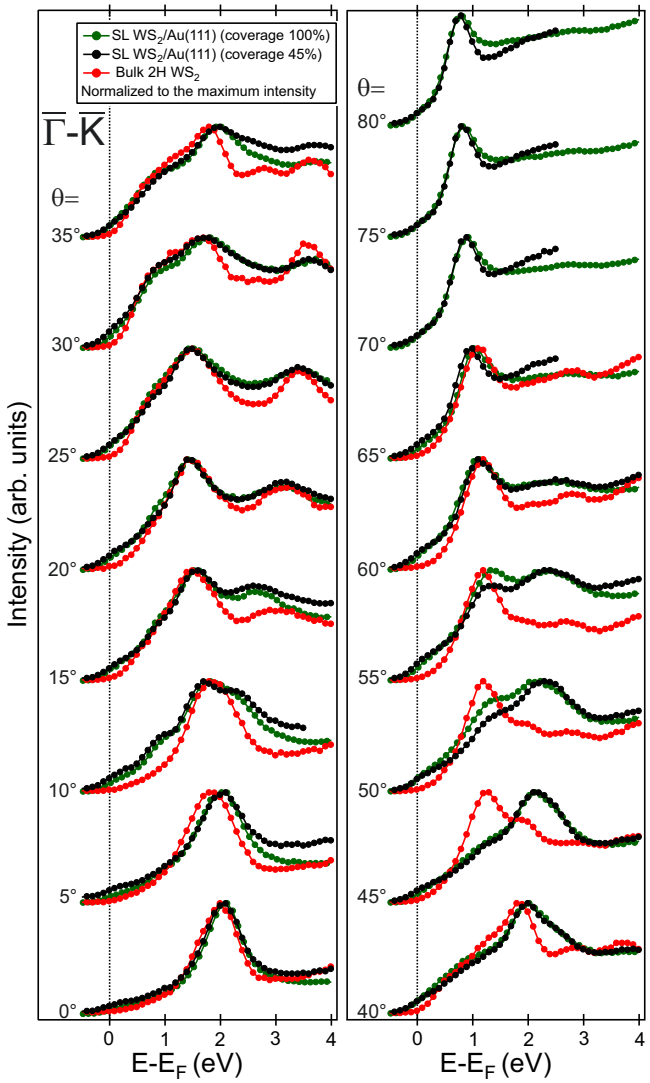

Figure A.9: IPE spectra of SL WS_2/Au(111) (coverage 100%, mirror domains), single-oriented SL WS_2/Au(111) (coverage 45%) and bulk WS_2 along $\overline{\Gamma}$-$\overline{K}$. Spin-integrated data are shown as black, green and red dots for single-oriented SL WS_2/Au(111), MD SL WS_2/Au(111) and bulk WS_2. The spectra are normalized to the maximum intensity. The spectra of bulk WS_2 and some spectra ($\theta = 0°$,$\theta = 30°$ and $\theta = 55°$) of 100% coverage MD SL WS_2/Au(111) have been gained in collaboration with Lukas Musiol and Marcel Holtmann, respectively, during their bachelor theses (Holtmann, 2016; Musiol, 2018).

A.7 Different Models Applied to the Fitting Procedure Used in Section 5.2.3 for Single-Oriented SL WS_2

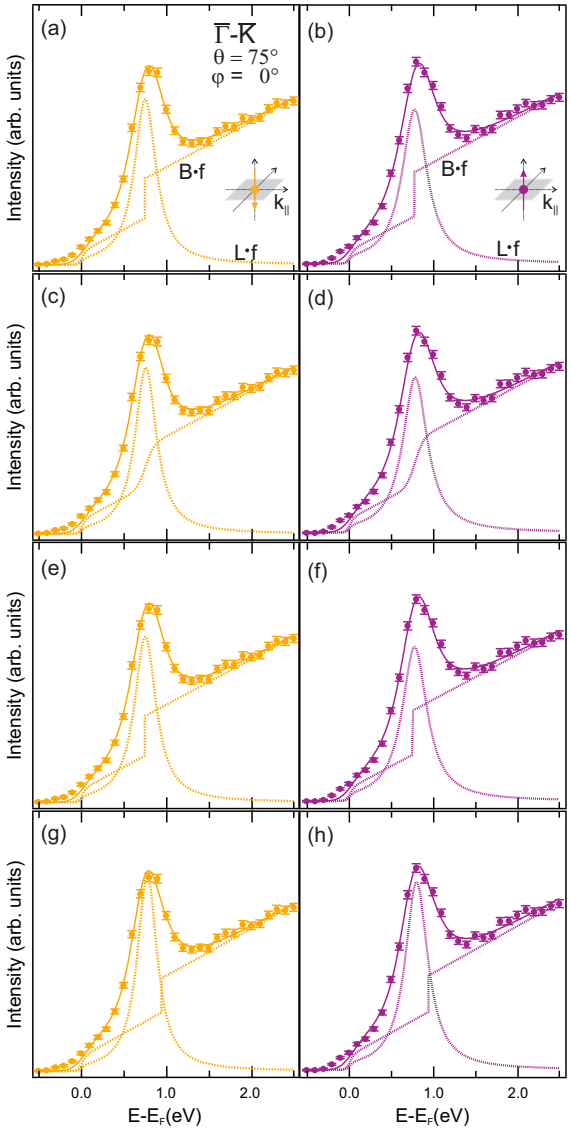

Figure A.10: Test of reliability and stability of the fitting routine for the spectra of $\theta = 75°$ along $\overline{\Gamma}$-$\overline{K}$: (a,b) model A as used in figure 5.12, (c,d) model B [broadened step function], (e,f) model C [spin-independent step energy], and (g,f) model D [spin-independent step energy, shifted by 0.2 eV to higher energy with respect to *L*]. Figure published in the supplement of Eickholt *et al.* (2018b). Reprinted with permission from Eickholt *et al.* (2018b). Copyright (2018) by the American Physical Society.

A.8 Influence of the Electron-Beam Spin-Polarization Uncertainty in SRIPE on the Determined Spin Splittings in Section 5.2.3

An important input to determine the individual spin spectra measured with nonideal spin polarization detectors and electron sources is the exact knowledge of S and P, respectively. Any uncertainty in S and P influences the outcome of the "normalization" procedure. In the present work, the spin polarization of the electron source is $P = 29 \pm 3\%$ (see Budke *et al.* (2007a)).

In figure A.11 it is demonstrated, how this uncertainty in P influences the determination of the CB spin splitting at the $\overline{K}$ valley of WS_2. In the left-hand panel, the spin-resolved raw inverse-photoemission data is presented. The additional three panels show the individual spin spectra, derived with equation 3.9 for assumed electron-beam spin polarization values of 26, 29, and 32%. All results are shown in table A1. The spin splitting for $\theta = 80°$ along $\overline{\Gamma}$-$\overline{K}$ changes with the assumed spin polarization values by ± 2 meV, and for $\theta = 70°$ along $\overline{\Gamma}$-$\overline{K}'$ by ± 3 meV. The above determined uncertainties of the spin splittings have a negligible effect on the uncertainty margins of ± 7 meV and ± 6 meV for $\theta = 80°$ along $\overline{\Gamma}$-$\overline{K}$ and $\theta = 70°$ along $\overline{\Gamma}$-$\overline{K}'$, respectively.

Table A1: Influence of the assumed spin polarization P of the incoming electrons in IPE.

	$E_\uparrow$ (meV)	$E_\downarrow$ (meV)	$\Delta E_{\uparrow\downarrow}$ (meV)
$\theta = 80°$ $\overline{\Gamma}$-$\overline{K}$			
Raw data	722.3 ± 1.9	717.8 ± 2.0	4.5 ± 2.8
Data for $P = 32\%$	726.9 ± 4.5	712.4 ± 5.0	14.5 ± 6.8
Data for $P = 29\%$	727.5 ± 4.9	711.5 ± 5.4	16.0 ± 7.4
Data for $P = 26\%$	728.4 ± 5.4	710.5 ± 6.1	17.9 ± 8.2
$\theta = 70°$ $\overline{\Gamma}$-$\overline{K'}$			
Raw data	875.1 ± 1.7	884.3 ± 1.8	-9.2 ± 2.4
Data for $P = 32\%$	865.8 ± 3.9	893.8 ± 3.9	-28.0 ± 5.5
Data for $P = 29\%$	864.5 ± 4.3	895.3 ± 4.3	-30.8 ± 6.1
Data for $P = 26\%$	862.9 ± 4.7	897.1 ± 4.8	-34.3 ± 6.7

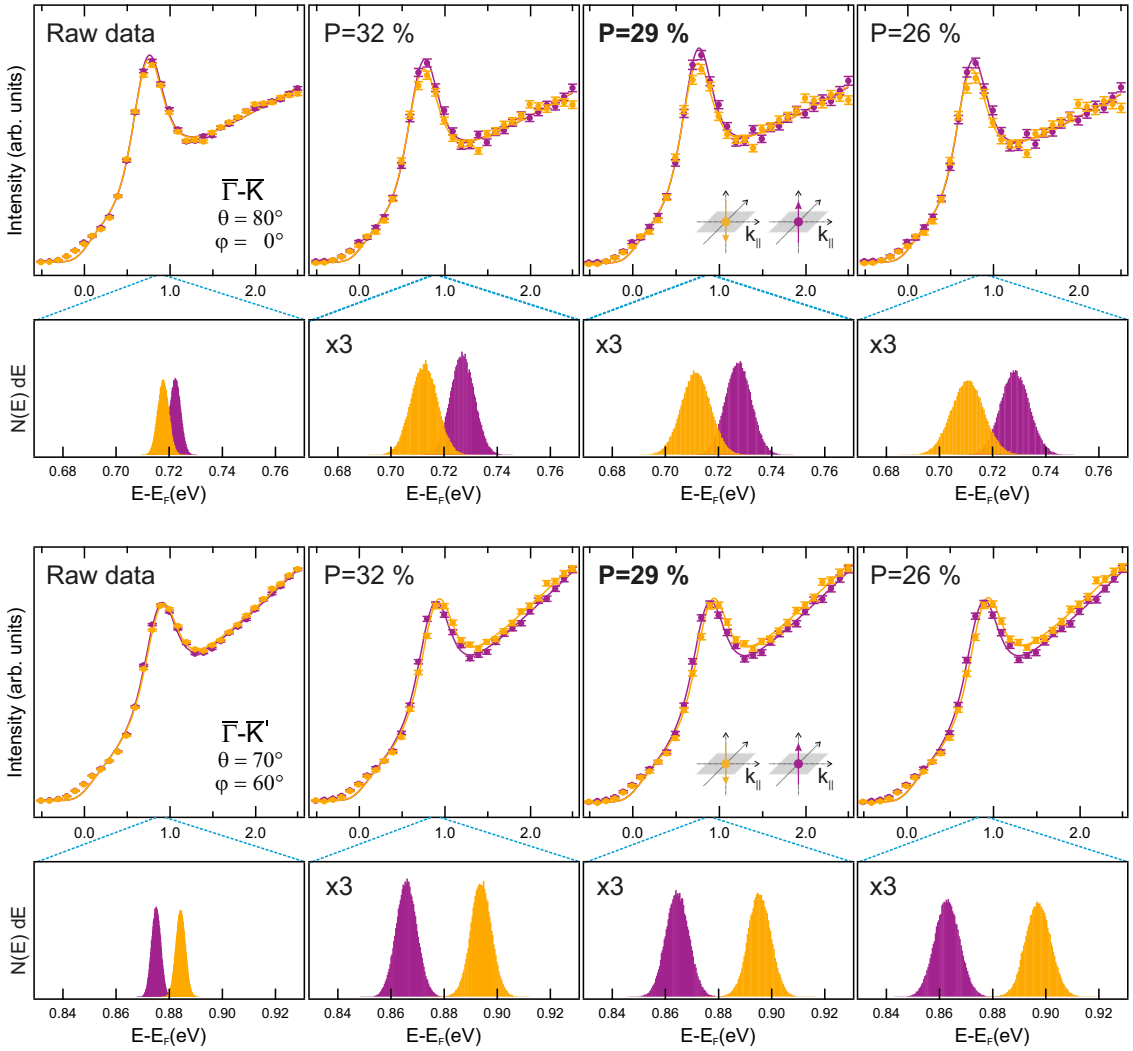

Figure A.11: IPE spectra for $\theta = 80°$ along $\overline{\Gamma}$-$\overline{\mathrm{K}}$ (upper panel) and for $\theta = 70°$ along $\overline{\Gamma}$-$\overline{\mathrm{K}}'$ (lower panel). From left to right: Raw data, spin-resolved data normalized to 26, 29, and 32% of spin polarization P of the electron beam together with corresponding peak-position distributions $N(E)dE$.

Bibliography

Andreev, T., Barke, I., Hövel, H. (2004), 'Adsorbed rare-gas layers on Au(111): Shift of the Shockley surface state studied with ultraviolet photoelectron spectroscopy and scanning tunneling spectroscopy', *Phys. Rev. B* **70**, 205426.

Arora, A., Noky, J., Drüppel, M., Jariwala, B., Deilmann, T., Schneider, R., Schmidt, R., Del Pozo-Zamudio, O., Stiehm, T., Bhattacharya, A., Krüger, P., Michaelis de Vasconcellos, S., Rohlfing, M., Bratschitsch, R. (2017), 'Highly Anisotropic in-Plane Excitons in Atomically Thin and Bulklike 1T′-$ReSe_2$', *Nano Lett.* **17**, 3202.

Bai, C. (2000), 'Scanning Tunneling Microscopy and Its Application', in G. Ertl, H. Lüth, R. Car, M.A. Rocca, H.J. Freund (eds.) 'Springer Series in Surface Sciences', volume 32, Springer, Berlin, 370.

Bana, H., Travaglia, E., Bignardi, L., Lacovig, P., Sanders, C.E., Dendzik, M., Michiardi, M., Bianchi, M., Lizzit, D., Presel, F., Angelis, D.D., Apostol, N., Das, P.K., Fujii, J., Vobornik, I., Larciprete, R., Baraldi, A., Hofmann, P., Lizzit, S. (2018), 'Epitaxial growth of single-orientation high-quality Mos 2 monolayers', *2D Mater.* **5**, 035012.

Bernadi, M., Ataca, C., Palummo, M., Grossman, J.C. (2017), 'Optical and electronic properties of two-dimensional layered materials', *Nanophotonics* **6**, 479.

Bernett, M.K., Murday, J.S., Turner, N.H. (1977), 'An interpretation of the auger LVV transitions from oxides of third-row elements', *J. Electron. Spectrosc. Relat. Phenom.* **12**, 375.

Bignardi, L., Lizzit, D., Bana, H., Travaglia, E., Lacovig, P., Sanders, C.E., Dendzik, M., Michiardi, M., Bianchi, M., Ewert, M., Bu, L., Falta, J., Flege, J.I., Baraldi, A., Larciprete, R., Hofmann, P., Lizzit, S. (2019), 'Growth and Structure of Singly-Oriented Single-Layer Tungsten Disulfide on Au(111)', *Phys. Rev. Mater.* **3**, 014003.

Binnig, G., Rohrer, H. (1983), 'Scanning tunneling microscopy', *Surf. Sci.* **126**, 236.

Biswas, D., Ganose, A.M., Yano, R., Riley, J.M., Bawden, L., Clark, O.J., Feng, J., Collins-Mcintyre, L., Sajjad, M.T., Meevasana, W., Kim, T.K., Hoesch, M., Rault, J.E., Sasagawa, T., Scanlon, D.O., King, P.D.C. (2017), 'Narrow-band anisotropic electronic structure of ReS_2', *Phys. Rev. B* **96**, 085205.

Bruix, A., Füchtbauer, H.G., Tuxen, A.K., Walton, A.S., Andersen, M., Porsgaard, S., Besenbacher, F., Hammer, B., Lauritsen, J.V. (2015), 'In Situ Detection of Active Edge Sites in Single-Layer MoS_2 catalysts', *ACS Nano* **9**, 9322.

Bruix, A., Miwa, J.A., Hauptmann, N., Wegner, D., Ulstrup, S., Grønborg, S.S., Sanders, C.E., Dendzik, M., Grubisic Cabo, A., Bianchi, M., Lauritsen, J.V., Khajetoorians, A.A., Hammer, B., Hofmann, P. (2016), 'Single-layer MoS_2 on Au(111): Band gap renormalization and substrate interaction', *Phys. Rev. B* **93**, 165422.

Budke, M., Allmers, T., Donath, M., Rangelov, G. (2007a), 'Combined experimental setup for spin- and angle-resolved direct and inverse photoemission', *Rev. Sci. Instrum.* **78**, 113909.

Budke, M., Renken, V., Liebl, H., Rangelov, G., Donath, M. (2007b), 'Inverse photoemission with energy resolution better than 200 mev', *Rev. Sci. Instrum.* **78**, 83903.

Bychkov, Y.A., Rashba, E.I. (1984), 'Properties of a 2D electron gas with lifted spctral degeneracy', *JETP Lett.* **39**, 78.

Cappelluti, E., Roldán, R., Silva-Guillén, J.A., Ordejón, P., Guinea, F. (2013), 'Tight-binding model and direct-gap/indirect-gap transition in single-layer and multilayer MoS_2', *Phys. Rev. B* **88**.

Cattelan, M., Fox, N.A. (2018), 'A Perspective on the Application of Spatially Resolved Arpes for 2D Materials', *Nanomaterials* **8**, 284.

Cheiwchanchamnangij, T., Lambrecht, W.R.L. (2012), 'Quasiparticle band structure calculation of monolayer, bilayer, and bulk MoS_2', *Phys. Rev. B* **85**, 205302.

Chenet, D.A., Aslan, O.B., Huang, P.Y., Fan, C., van der Zande, Arend M., Heinz, T.F., Hone, J.C. (2015), 'In-Plane Anisotropy in Mono- and Few-layer ReS_2 Probed by Raman Spectroscopy and Scanning Transmission Electron Microscopy', *Nano Lett.* **15**, 5667.

Chernikov, A., Berkelbach, T.C., Hill, H.M., Rigosi, A., Li, Y., Aslan, O.B., Reichman, D.R., Hybertsen, M.S., Heinz, T.F. (2014), 'Exciton Binding Energy and Nonhydrogenic Rydberg Series in Monolayer WS_2', *Phys. Rev. Lett.* **113**, 076802.

Chiang, T.C. (2000), 'Photoemission studies of quantum well states in thin films', *Surf. Sci. Rep.* **39**, 181.

Cui, Q., He, J., Bellus, M.Z., Mirzokarimov, M., Hofmann, T., Chiu, H.Y., Antonik, M., He, D., Wang, Y., Zhao, H. (2015), 'Transient Absorption Measurements on Anisotropic Monolayer ReS_2', *Small* **11**, 5565.

Damascelli, A. (2004), 'Probing the Electronic Structure of Complex Systems by ARPES', *Phys. Scr.* **2004**, 61.

Datta, S., Das, B. (1990), 'Electronic analog of the electro-optic modulator', *Appl. Phys. Lett.* **56**, 665.

Davis, L., Mac Donald, N., Palmberg, P.W., Riach, G.E., Weber, R. (1976), *Handbook of Auger Electron Spectroscopy: A Reference Book of Standard Data for Identification and Interpretation of Auger Electron Spectroscopy Data*, Physical Electronics Industries, Inc., Minnesota, 2nd edition.

Dendzik, M., Bruix, A., Michiardi, M., Ngankeu, A.S., Bianchi, M., Miwa, J.A., Hammer, B., Hofmann, P., Sanders, C.E. (2017), 'Substrate-induced semiconductor-to-metal transition in monolayer WS_2', *Phys. Rev. B* **96**, 235440.

Dendzik, M., Michiardi, M., Sanders, C., Bianchi, M., Miwa, J.A., Grnborg, S.S., Lauritsen, J.V., Bruix, A., Hammer, B., Hofmann, P. (2015), 'Growth and electronic structure of epitaxial single-layer WS_2 on Au(111)', *Phys. Rev. B* **92**, 245442.

Ding, Y., Wang, Y., Ni, J., Shi, L., Shi, S., Tang, W. (2011), 'First principles study of structural, vibrational and electronic properties of graphene-like MX_2 (M=Mo, Nb, W, Ta; X=S, Se, Te) monolayers', *Physica B* **406**, 2254.

Donath, M. (1994), 'Spin-dependent electronic structure at magnetic surfaces: the low-miller-index surfaces of nickel', *Surf. Sci. Rep.* **20**, 251.

Donath, M. (2018), 'In or Out of Control? Electron Spin Polarization in Spin-Orbit-Influenced Systems', in K. Wandelt (ed.) 'Encyclopedia of Interfacial Chemistry', volume 2, Elsevier, Oxford, 131.

Donath, M., Ertl, K. (1992), 'Adsorbate-induced enhancement of image-potential surface states on Ni(110)', *Surf. Sci.* **262**, L49 .

Dose, V. (1985), 'Momentum-Resolved Inverse Photoemission', *Surf. Sci. Rep.* **5**, 337.

Dose, V., Reusing, G. (1980), 'Electron-Hole Pair Production and the Structure of Ultraviolet Isochromats', *Appl. Phys.* **23**, 131.

Dresselhaus, G. (1955), 'Spin-Orbit Coupling Effects in Zinc Blende Structures', *Phys. Rev.* **100**, 580.

Drüppel, M. (2017), private communication.

Eberhardt, W., Himpsel, F.J. (1980), 'Dipole selection rules for optical transitions in the fcc and bcc lattices', *Phys. Rev. B* **21**, 5572.

Echeverry, J.P., Urbaszek, B., Amand, T., Marie, X., Gerber, I.C. (2016), 'Splitting between bright and dark excitons in transition metal dichalcogenide monolayers', *Phys. Rev. B* **93**, 121107.

Eickholt, P., Krüger, P., Stolwijk, S.D., Schmidt, A.B., Donath, M. (2016), 'Effects of orbital composition in a pair of spin-orbit-split surface bands at Tl/Ge(111)', *Phys. Rev. B* **93**, 085412.

Eickholt, P., Noky, J., Schwier, E.F., Shimada, K., Miyamoto, K., Okuda, T., Datzer, C., Drüppel, M., Krüger, P., Rohlfing, M., Donath, M. (2018a), 'Location of the valence band maximum in the band structure of anisotropic 1T′-$ReSe_2$', *Phys. Rev. B* **97**, 165130.

Eickholt, P., Sanders, C., Dendzik, M., Bignardi, L., Lizzit, D., Lizzit, S., Bruix, A., Hofmann, P., Donath, M. (2018b), 'Spin Structure of K Valleys in Single-Layer WS_2 on Au(111)', *Phys. Rev. Lett.* **121**, 136402.

Einstein, A. (1905), 'Über einen die Erzeugung und Verwandlung des Lichtes betreffenden heuristischen Gesichtspunkt', *Ann. Phys.* **322**, 132.

Ertl, G., Küppers, J. (1985), *Low Energy Electrons and Surface Chemistry*, VCH, Weinheim, 2. edition.

Ewert, M. (2019), *In-situ-Studien zu Wachstum und Struktur von Übergangsmetall-Dichalcogeniden*, Phd thesis, University of Bremen, Bremen.

Feder, R., Kirschner, J. (1981), 'Spin polarized low energy electron diffraction: theory, experiments and analysis of results from W(001)(1x1)', *Surf. Sci.* **103**, 75.

Forster, F., Bendounan, A., Reinert, F., Grigoryan, V.G., Springborg, M. (2007), 'The Shockley-type surface state on Ar covered Au(111): High resolution photoemission results and the description by slab-layer DFT calculations', *Surf. Sci.* **601**, 5595.

Forster, F., Nicolay, G., Reinert, F., Ehm, D., Schmidt, S., Hüfner, S. (2003), 'Surface and interface states on adsorbate covered noble metal surfaces', *Surf. Sci.* **532-535**, 160.

Forti, S., Rossi, A., Büch, H., Cavallucci, T., Bisio, F., Sala, A., Menteş, T.O., Locatelli, A., Magnozzi, M., Canepa, M., Müller, K., Link, S., Starke, U., Tozzini, V., Coletti, C. (2017), 'Electronic properties of single-layer tungsten disulfide on epitaxial graphene on silicon carbide', *Nanoscale* **9**, 16412.

Grønborg, S.S., Søren Ulstrup, Marco Bianchi, Maciej Dendzik, Charlotte E. Sanders, Jeppe V. Lauritsen, Philip Hofmann, Jill A. Miwa (2015), 'Synthesis of Epitaxial Single-Layer MoS_2 on Au(111)', *Langmuir* **31**, 9700.

Grubisic Cabo, A., Miwa, J.A., Grønborg, S.S., M. Riley, J., Johannsen, J.C., Cacho, C., Alexander, O., Chapman, R.T., Springate, E., Grioni, M., Lauritsen, J.V., King, P.D.C., Hofmann, P., Ulstrup, S. (2015), 'Observation of Ultrafast Free Carrier Dynamics in Single Layer MoS_2', *Nano Lett.* **15**, 5883.

Haken, H., Wolf, H.C. (2002), *Atom- und Quantenphysik: Einführung in die experimentellen und theoretischen Grundlagen*, Springer-Lehrbuch, Springer, Berlin, 7. edition.

Han, G.H., Duong, D.L., Keum, D.H., Yun, S.J., Lee, Y.H. (2018), 'van der Waals Metallic Transition Metal Dichalcogenides', *Chem. Rev.* **118**, 6297.

Hart, L.S., Webb, J.L., Dale, S., Bending, S.J., Mucha-Kruczynski, M., Wolverson, D., Chen, C., Avila, J., Asensio, M.C. (2017), 'Electronic bandstructure and van der Waals coupling of $ReSe_2$ revealed by high-resolution angle-resolved photoemission spectroscopy', *Sci. Rep.* **7**, 5145.

He, K., Kumar, N., Zhao, L., Wang, Z., Mak, K.F., Zhao, H., Shan, J. (2014), 'Tightly bound excitons in monolayer WSe_2', *Phys. Rev. Lett.* **113**, 026803.

Henk, J. (2001), 'Theory of Low-energy Electron Diffraction and Photoelectron Spectroscopy from Ultra-thin films', in H.S. Nalwa (ed.) 'Handbook of Thin Film Materials Volume 2: Characterization and Spectroscopy', volume 2, chapter 10, Stanford Scientific Corp., Los Angeles, 479.

Henk, J., Miyamoto, K., Donath, M. (2018), 'Retrieving the initial-state spin polarization from spin-resolved photoemission: Proposal for a case study on W(110)', *Phys. Rev. B* **98**, 045124.

Henk, J., Scheunemann, T., Halilov, S.V., Feder, R. (1996), 'Magnetic dichroism and electron spin polarization in photoemission: analytical results', *J. Phys.: Condens. Matter* **8**, 47.

Hertz, H. (1887), 'Ueber einen Einfluss des ultravioletten Lichtes auf die electrische Entladung', *Ann. Phys.* **267**, 983.

Himpsel, F.J. (1980), 'Experimental determination of bulk energy band dispersions', *Appl. Opt.* **19**, 3964.

Himpsel, F.J. (1990), 'Inverse photoemission from semiconductors', *Surf. Sci. Rep.* **12**, 3.

Ho, C.H., Huang, C.E. (2004), 'Optical property of the near band-edge transitions in rhenium disulfide and diselenide', *J. Alloys Compd.* **383**, 74.

Ho, C.H., Huang, Y.S., Tiong, K.K. (2001), 'In-plane anisotropy of the optical and electrical properties of ReS_2 and $ReSe_2$ layered crystals', *J. Alloys Compd.* **317–318**, 222.

Hoesch, M., Muntwiler, M., Petrov, V.N., Hengsberger, M., Patthey, L., Shi, M., Falub, M., Greber, T., Osterwalder, J. (2004), 'Spin structure of the Shockley surface state on Au(111)', *Phys. Rev. B* **69**.

Holtmann, M. (2016), *Präparation und Charakterisierung einer WS_2-Lage auf Au(111)*, Bachelor thesis, Westfälische Wilhelms-Universität, Münster.

Hsu, W.T., Lu, L.S., Wang, D., Huang, J.K., Li, M.Y., Chang, T.R., Chou, Y.C., Juang, Z.Y., Jeng, H.T., Li, L.J., Chang, W.H. (2017), 'Evidence of indirect gap in monolayer WSe_2', *Nat. Commun.* **8**, 929.

Huang, Y.S., Ho, C.H., Liao, P.C., Tiong, K.K. (1997), 'Temperature dependent study of the band edge excitons of ReS_2 and $ReSe_2$', *J. Alloys Compd.* **262–263**, 92.

Hüfner, S. (2003), *Photoelectron Spectroscopy: Principles and Applications*, Advanced Texts in Physics, Springer, Berlin and Heidelberg, third revised and enlarged edition.

Jia, J.F., Inoue, K., Hasegawa, Y., Yang, W.S., Sakurai, T. (1998), 'Variation of the local work function at steps on metal surfaces studied with STM', *Phys. Rev. B* **58**, 1193.

Jin, W., Yeh, P.C., Zaki, N., Zhang, D., Sadowski, J.T., Al-Mahboob, A., van der Zande, Arend M., Chenet, D.A., Dadap, J.I., Herman, I.P., Sutter, P., Hone, J., Osgood, R.M. (2013), 'Direct Measurement of the Thickness-Dependent Electronic Band Structure of MoS_2 Using Angle-Resolved Photoemission Spectroscopy', *Phys. Rev. Lett.* **111**, 106801.

Johnson, P.D. (1997), 'Spin-polarized photoemission', *Rep. Prog. Phys.* **60**, 1217.

Jozwiak, C., Chen, Y.L., Fedorov, A.V., Analytis, J.G., Rotundu, C.R., Schmid, A.K., Denlinger, J.D., Chuang, Y.D., Lee, D.H., Fisher, I.R., Birgeneau, R.J., Shen, Z.X., Hussain, Z., Lanzara, A. (2011), 'Widespread spin polarization effects in photoemission from topological insulators', *Phys. Rev. B* **84**.

Kanai, K., Ouchi, Y., Seki, K. (2009), 'Modification of Shockley surface state by long-chain n-alkane: Photoemission study on tetratetracontane/Au(111) interface', *Thin Solid Films* **517**, 3276.

Kane, E.O. (1964), 'Implications of crystal momentum conservation in photoelectric emission for band-structure measurements', *Phys. Rev. Lett.* **12**, 97.

Katoch, J., Ulstrup, S., Koch, R.J., Moser, S., McCreary, K.M., Singh, S., Xu, J., Jonker, B.T., Kawakami, R.K., Bostwick, A., Rotenberg, E., Jozwiak, C. (2018), 'Giant spin-splitting and gap renormalization driven by trions in single-layer WS_2/h-BN heterostructures', *Nat. Phys.* **14**, 355.

Katzke, H., Tolédano, P., Depmeier, W. (2004), 'Phase transitions between polytypes and intralayer superstructures in transition metal dichalcogenides', *Phys. Rev. B* **69**, 134111.

Kessler, J. (1985), *Polarized Electrons*, volume 1 of *Springer Series on Atoms and Plasmas*, Springer, Berlin, Heidelberg, New York, Tokyo, 2nd edition.

Kisker, E. (1985), 'Spin- and angle-resolved photoemission from ferromagnets', in R. Feder (ed.) 'Polarized Electrons in Surface Physics', World Scientific, Singapore, Chap. 12, pp. 513–546.

Klein, A., Tiefenbacher, S., Eyert, V., Pettenkofer, C., Jaegermann, W. (2001), 'Electronic band structure of single-crystal and single-layer WS_2: Influence of interlayer van der Waals interactions', *Phys. Rev. B* **64**, 205416.

Kormányos, A., Burkard, G., Gmitra, M., Fabian, J., Zólyomi, V., Drummond, N.D., Fal'ko, V. (2015), 'k·p theory for two-dimensional transition metal dichalcogenide semiconductors', *2D Mater.* **2**, 022001.

Kosmider, K., Gonzalez, J.W., Fernandez-Rossier, J. (2013), 'Large spin splitting in the conduction band of transition metal dichalcogenide monolayers', *Phys. Rev. B* **88**, 245436.

Krasovskii, E.E. (2015), 'Spin-orbit coupling at surfaces and 2D materials', *J. Phys.: Condens. Matter* **27**, 493001.

Krasovskii, E.E., Chulkov, E.V. (2011), 'Rashba polarization of bulk continuum states', *Phys. Rev. B* **83**, 155401.

Krüger, P. (2016), private communication.

Krüger, P. (2018), private communication.

Kumar, A., Ahluwalia, P.K. (2012), 'Electronic structure of transition metal dichalcogenides monolayers 1H-MX_2 (M = Mo, W; X = S, Se, Te) from ab-initio theory: new direct band gap semiconductors', *Eur. Phys. J. B* **85**, 186.

Kuroda, K., Yaji, K., Nakayama, M., Harasawa, A., Ishida, Y., Watanabe, S., Chen, C.T., Kondo, T., Komori, F., Shin, S. (2016), 'Coherent control over three-dimensional spin polarization for the spin-orbit coupled surface state of Bi_2Se_3', *Phys. Rev. B* **94**, 165162.

Lamfers, H.J., Meetsma, A., Wiegers, G.A., de Boer, J.L. (1996), 'The crystal structure of some rhenium and technetium dichalcogenides', *J. Alloys Compd.* **241**, 34.

LaMountain, T., Lenferink, E.J., Chen, Y.J., Stanev, T.K., Stern, N.P. (2018), 'Environmental engineering of transition metal dichalcogenide optoelectronics', *Front. Phys.* **13**, 138114.

LaShell, S., McDougall, B.A., Jensen, E. (1996), 'Spin Splitting of an Au(111) Surface State Band Observed with Angle Resolved Photoelectron Spectroscopy', *Phys. Rev. Lett.* **77**, 3419.

Latzke, D.W., Zhang, W., Suslu, A., Chang, T.R., Lin, H., Jeng, H.T., Tongay, S., Wu, J., Bansil, A., Lanzara, A. (2015), 'Electronic structure, spin-orbit coupling, and interlayer interaction in bulk MoS_2 and WS_2', *Phys. Rev. B* **91**, 235202.

Le, D., Barinov, A., Preciado, E., Isarraraz, M., Tanabe, I., Komesu, T., Troha, C., Bartels, L., Rahman, T.S., Dowben, P.A. (2015), 'Spin-orbit coupling in the band structure of monolayer WSe_2', *J. Phys.: Condens. Matter* **27**, 182201.

Li, J., Zhong, Y.L., Zhang, D. (2015), 'Excitons in monolayer transition metal dichalcogenides', *J. Phys.: Condens. Matter* **27**, 315301.

Liang, Y., Huang, S., Soklaski, R., Yang, L. (2013), 'Quasiparticle band-edge energy and band offsets of monolayer of molybdenum and tungsten chalcogenides', *Appl. Phys. Lett.* **103**, 042106.

Lin, Y.C., Komsa, H.P., Yeh, C.H., Björkman, T., Liang, Z.Y., Ho, C.H., Huang, Y.S., Chiu, P.W., Krasheninnikov, A.V., Suenaga, K. (2015), 'Single-Layer ReS_2: Two-Dimensional Semiconductor with Tunable In-Plane Anisotropy', *ACS Nano* **9**, 11249.

Liu, G.B., Shan, W.Y., Yao, Y., Yao, W., Xiao, D. (2013), 'Three-band tight-binding model for monolayers of group-VIB transition metal dichalcogenides', *Phys. Rev. B* **88**, 085433.

Luo, J.W., Bester, G., Zunger, A. (2009), 'Full-Zone Spin Splitting for Electrons and Holes in Bulk GaAs and GaSb', *Phys. Rev. Lett.* **102**, 056405.

Mahan, G.D. (1970), 'Theory of Photoemission in Simple Metals', *Phys. Rev. B* **2**, 4334.

Mak, K.F., He, K., Shan, J., Heinz, T.F. (2012), 'Control of valley polarization in monolayer MoS_2 by optical helicity', *Nat. Nanotechnol.* **7**, 494.

Mak, K.F., Lee, C., Hone, J., Shan, J., Heinz, T.F. (2010), 'Atomically thin MoS_2: A new direct-gap semiconductor', *Phys. Rev. Lett.* **105**, 136805.

Marzik, J.V., Kershaw, R., Dwight, K., Wold, A. (1984), 'Photoelectronic properties of ReS_2 and $ReSe_2$ single crystals', *J. Solid State Chem.* **51**, 170.

Michaelson, H.B. (2008), 'The work function of the elements and its periodicity', *J. Appl. Phys.* **48**, 4729.

Miwa, J.A., Ulstrup, S., Sørensen, S.G., Dendzik, M., Čabo, A.G., Bianchi, M., Lauritsen, J.V., Hofmann, P. (2015), 'Electronic structure of epitaxial single-layer MoS_2', *Phys. Rev. Lett.* **114**, 046802.

Miyamoto, K. (2016), private communication.

Miyamoto, K., Wortelen, H., Okuda, T., Henk, J., Donath, M. (2018), 'Circular-polarized-light-induced spin polarization characterized for the Dirac-cone surface state at W(110) with C2v symmetry', *Sci. Rep.* **8**, 10440.

Mo, S.K., Hwang, C., Zhang, Y., Fanciulli, M., Muff, S., Dil, J.H., Shen, Z.X., Hussain, Z. (2016), 'Spin-resolved photoemission study of epitaxially grown $MoSe_2$ and WSe_2 thin films', *J. Phys.: Condens. Matter* **28**, 454001.

Molas, M.R., Faugeras, C., Slobodeniuk, A.O., Nogajewski, K., Bartos, M., Basko, D.M., Potemski, M. (2017), 'Brightening of dark excitons in monolayers of semiconducting transition metal dichalcogenides', *2D Mater.* **4**, 021003.

Murray, C., Jolie, W., Fischer, J.A., Hall, J., van Efferen, C., Ehlen, N., Grüneis, A., Busse, C., Michely, T. (2019), 'Comprehensive tunneling spectroscopy of quasifreestanding MoS_2 on graphene on Ir(111)', *Phys. Rev. B* **99**, 115434.

Musiol, L. (2018), *Die unbesetzte elektronische Struktur von 2H-Wolframdisulfid*, Bachelor thesis, Westfälische Wilhelms-Universität, Münster.

Nagler, P., Plechinger, G., Schüller, C., Korn, T. (2016), 'Observation of anisotropic interlayer raman modes in few-layer ReS_2', *Phys. Status Solidi RRL* **10**, 185.

Nam, S.B., Reynolds, D.C., Litton, C.W., Almassy, R.J., Collins, T.C., Wolfe, C.M. (1976), 'Free-exciton energy spectrum in GaAs', *Phys. Rev. B* **13**, 761.

Narumand, D.H., Childs, K.D. (1999), 'Auger spectrometers: A tutorial review', *Appl. Spectrosc. Rev.* **34**, 34.

Noky, J. (2017), *Ab initio Untersuchung der elektronischen und exzitonischen Anregungen in Monolayer- und Bulk-$ReSe_2$*, Master thesis, Westfälische Wilhelms-Universität, Münster.

Novoselov, K.S., Geim, A.K., Morozov, S.V., Jiang, D., Zhang, Y., Dubonos, S.V., Grigorieva, I.V., Firsov, A.A. (2004), 'Electric field effect in atomically thin carbon films', *Science* **306**, 666.

Novoselov, K.S., Jiang, D., Schedin, F., Booth, T.J., Khotkevich, V.V., Morozov, S.V., Geim, A.K. (2005), 'Two-dimensional atomic crystals', *PNAS* **102**, 10451.

Oguchi, T., Shishidou, T. (2009), 'The surface Rashba effect: a k·p perturbation approach', *J. Phys.: Condens. Matter* **21**, 92001.

Okuda, T., Miyamoto, K., Kimura, A., Namatame, H., Taniguchi, M. (2015), 'A double VLEED spin detector for high-resolution three dimensional spin vectorial analysis of anisotropic Rashba spin splitting', *J. Electron. Spectrosc. Relat. Phenom.* **201**, 23.

Okuda, T., Takeichi, Y., Maeda, Y., Harasawa, A., Matsuda, I., Kinoshita, T., Kakizaki, A. (2008), 'A new spin-polarized photoemission spectrometer with very high efficiency and energy resolution', *Rev. Sci. Instrum.* **79**, 123117.

Passek, F., Donath, M. (1992), 'Spin-split image-potential-induced surface state on Ni(111)', *Phys. Rev. Lett.* **69**, 1101.

Passek, F., Donath, M., Ertl, K., Dose, V. (1995), 'Longer Living Majority than Minority Image State at Fe(110)', *Phys. Rev. Lett.* **75**, 2746.

Pendry, J.B. (1981), 'Theory of inverse photoemission', *J. Phys. C: Solid State Phys.* **14**, 1381.

Pierce, D.T., Meier, F. (1976), 'Photoemission of spin-polarized electrons from gaas', *Phys. Rev. B* **13**, 5484.

Qiao, X.F., Wu, J.B., Zhou, L., Qiao, J., Shi, W., Chen, T., Zhang, X., Zhang, J., Ji, W., Tan, P.H. (2016), 'Polytypism and unexpected strong interlayer coupling in two-dimensional layered ReS_2', *Nanoscale* **8**, 8324.

Quereda, J., Ghiasi, T.S., van Zwol, F.A., van der Wal, C.H., van Wees, B.J. (2018), 'Observation of bright and dark exciton transitions in monolayer $MoSe_2$ by photocurrent spectroscopy', *2D Mater.* **5**, 015004.

Raja, A., Chaves, A., Yu, J., Arefe, G., Hill, H.M., Rigosi, A.F., Berkelbach, T.C., Nagler, P., Schüller, C., Korn, T., Nuckolls, C., Hone, J., Brus, L.E., Heinz, T.F., Reichman, D.R., Chernikov, A. (2017), 'Coulomb engineering of the bandgap and excitons in two-dimensional materials', *Nat. Commun.* **8**, 15251.

Ramasubramaniam, A. (2012), 'Large excitonic effects in monolayers of molybdenum and tungsten dichalcogenides', *Phys. Rev. B* **86**, 115409.

Ramasubramaniam, A., Naveh, D., Towe, E. (2011), 'Tunable band gaps in bilayer transition-metal dichalcogenides', *Phys. Rev. B* **84**, 205325.

Razzoli, E., Jaouen, T., Mottas, M.L., Hildebrand, B., Monney, G., Pisoni, A., Muff, S., Fanciulli, M., Plumb, N.C., Rogalev, V.A., Strocov, V.N., Mesot, J., Shi, M., Dil, J.H., Beck, H., Aebi, P. (2017), 'Selective Probing of Hidden Spin-Polarized States in Inversion-Symmetric Bulk MoS_2', *Phys. Rev. Lett.* **118**, 086402.

Rigosi, A.F., Hill, H.M., Rim, K.T., Flynn, G.W., Heinz, T.F. (2016), 'Electronic band gaps and exciton binding energies in monolayer $Mo_xW_{1-x}S_2$ transition metal dichalcogenide alloys probed by scanning tunneling and optical spectroscopy', *Phys. Rev. B* **94**, 075440.

Riley, J.M., Mazzola, F., Dendzik, M., Michiardi, M., Takayama, T., Bawden, L., GranerÃ¸d, C., Leandersson, M., Balasubramanian, T., Hoesch, M., Kim, T.K., Takagi, H., Meevasana, W., Hofmann, P., Bahramy, M.S., Wells, J.W., King, P.D.C. (2014), 'Direct observation of spin-polarized bulk bands in an inversion-symmetric semiconductor', *Nat. Phys.* **10**, 835.

Rivière, J.C. (1973), 'Auger electron spectroscopy', *Contemp. Phys.* **14**, 513.

Rohlfing, M. (2010), 'Electronic excitations from a perturbative LDA+GdW approach', *Phys. Rev. B* **82**, 205127.

Roldán, R., Guinea, F. (2017), 'Electronic properties and strain engineering in semiconducting transition metal dichalcogenides', in P. Avouris, T. Low, T.F. Heinz (eds.) '2D Materials: Properties and Devices', Cambridge University Press, Cambridge, 259.

Roldán, R., Silva-Guillén, J.A., López-Sancho, M.P., Guinea, F., Cappelluti, E., Ordejón, P. (2014), 'Electronic properties of single-layer and multilayer transition metal dichalcogenides MX_2 (M = Mo, W and X = S, Se)', *Ann. Phys.* **526**, 347.

Sanders, C.E. (2016), private communication.

Schwier, E.F. (2016), private communication.

Shi, H., Pan, H., Zhang, Y.W., Yakobson, B.I. (2013), 'Quasiparticle band structures and optical properties of strained monolayer MoS_2 and WS_2', *Phys. Rev. B* **87**, 155304.

Smith, N.V. (1988), 'Inverse photoemission', *Rep. Prog. Phys.* **51**, 1227.

Splendiani, A., Sun, L., Zhang, Y., Li, T., Kim, J., Chim, C.Y., Galli, G., Wang, F. (2010), 'Emerging photoluminescence in monolayer MoS_2', *Nano Lett.* **10**, 1271.

Stolwijk, S.D., Wortelen, H., Schmidt, A.B., Donath, M. (2014), 'Rotatable spin-polarized electron source for inverse-photoemission experiments', *Rev. Sci. Instrum.* **85**, 013306.

Strocov, V.N., Claessen, R., Nicolay, G., Hüfner, S., Kimura, A., Harasawa, A., Shin, S., Kakizaki, A., Nilsson, P.O., Starnberg, H.I., Blaha, P. (1998), 'Absolute Band Mapping by Combined Angle-Dependent Very-Low-Energy Electron Diffraction and Photoemission: Application to Cu', *Phys. Rev. Lett.* **81**, 4943.

Strocov, V.N., Claessen, R., Nicolay, G., Hüfner, S., Kimura, A., Harasawa, A., Shin, S., Kakizaki, A., Starnberg, H.I., Nilsson, P.O., Blaha, P. (2001), 'Three-dimensional band mapping by angle-dependent very-low-energy electron diffraction and photoemission: Methodology and application to Cu', *Phys. Rev. B* **63**, 205108.

Strocov, V.N., Starnberg, H.I., Nilsson, P.O., Brauer, H.E., Holleboom, L.J. (1997), 'New Method for Absolute Band Structure Determination by Combining Photoemission with Very-Low-Energy Electron Diffraction: Application to Layered VSe_2', *Phys. Rev. Lett.* **79**, 467.

Sun, Y., Wang, D., Shuai, Z. (2016), 'Indirect-to-direct band gap crossover in few-layer transition metal dichalcogenides: A theoretical prediction', *J. Phys. Chem. C* **120**, 21866.

Suzuki, R., Sakano, M., Zhang, Y.J., Akashi, R., Morikawa, D., Harasawa, A., Yaji, K., Kuroda, K., Miyamoto, K., Okuda, T., Ishizaka, K., Arita, R., Iwasa, Y. (2014), 'Valley-dependent spin polarization in bulk MoS_2 with broken inversion symmetry', *Nat. Nanotechnol.* **9**, 611.

Tatsumi, Y., Ghalamkari, K., Saito, R. (2016), 'Laser energy dependence of valley polarization in transition-metal dichalcogenides', *Phys. Rev. B* **94**, 235408.

Tersoff, J., Hamann, D.R. (1983), 'Theory and application for the scanning tunneling microscope', *Phys. Rev. Lett.* **50**, 1998.

Tersoff, J., Hamann, D.R. (1985), 'Theory of the scanning tunneling microscope', *Phys. Rev. B* **31**, 805.

Thiede, C., Niehues, I., Schmidt, A.B., Donath, M. (2018), 'The acetone band-pass detector for inverse photoemission: operation in proportional and Geiger-Müller modes', *Meas. Sci. Technol.* **29**, 065901.

Tiong, K.K., Ho, C.H., Huang, Y.S. (1999), 'The electrical transport properties of ReS_2 and $ReSe_2$ layered crystals', *Solid State Commun.* **111**, 635.

Tongay, S., Sahin, H., Ko, C., Luce, A., Fan, W., Liu, K., Zhou, J., Huang, Y.S., Ho, C.H., Yan, J., Ogletree, D.F., Aloni, S., Ji, J., Li, S., Li, J., Peeters, F.M., Wu, J. (2014), 'Monolayer behaviour in bulk ReS_2 due to electronic and vibrational decoupling', *Nat Commun* **5**, 3252.

Tusche, C., Krasyuk, A., Kirschner, J. (2015), 'Spin resolved bandstructure imaging with a high resolution momentum microscope', *Ultramicroscopy* **159**, 520 .

Ugeda, M.M., Bradley, A.J., Shi, S.F., Jornada, F.H.d., Zhang, Y., Qiu, D.Y., Ruan, W., Mo, S.K., Hussain, Z., Shen, Z.X., Wang, F., Louie, S.G., Crommie, M.F. (2014), 'Giant bandgap renormalization and excitonic effects in a monolayer transition metal dichalcogenide semiconductor', *Nat. Mater.* **13**, 1091.

Ulstrup, S., Cabo, A.G., Biswas, D., Riley, J.M., Dendzik, M., Sanders, C.E., Bianchi, M., Cacho, C., Matselyukh, D., Chapman, R.T., Springate, E., King, P.D.C., Miwa, J.A., Hofmann, P. (2017), 'Spin and valley control of free carriers in single-layer WS_2', *Phys. Rev. B* **95**, 041405.

Ulstrup, S., Čabo, A.G., Miwa, J.A., Riley, J.M., Grønborg, S.S., Johannsen, J.C., Cacho, C., Alexander, O., Chapman, R.T., Springate, E., Bianchi, M., Dendzik, M., Lauritsen, J.V., King, P.D.C., Hofmann, P. (2016a), 'Ultrafast band structure control of a two-dimensional heterostructure', *ACS Nano* **10**, 6315.

Ulstrup, S., Katoch, J., Koch, R.J., Schwarz, D., Singh, S., McCreary, K.M., Yoo, H.K., Xu, J., Jonker, B.T., Kawakami, R.K., Bostwick, A., Rotenberg, E., Jozwiak, C. (2016b), 'Spatially resolved electronic properties of single-layer WS_2 on transition metal oxides', *ACS Nano* **10**, 10058.

van Le, Q., Nguyen, T.P., Kim, S.Y. (2014), 'UV/ozone-treated WS_2 hole-extraction layer in organic photovoltaic cells', *Phys. Status Solidi RRL* **8**, 390.

Vaughan, D.J., Tossell, J.A. (1986), 'Interpretation of the auger electron spectra (AES) of sulfide minerals', *Phys. Chem. Miner.* **13**, 347.

Wan, A., Hwang, J., Amy, F., Kahn, A. (2005), 'Impact of electrode contamination on the α-NPD/Au hole injection barrier', *Org. Electron.* **6**, 47.

Wang, G., Chernikov, A., Glazov, M.M., Heinz, T.F., Marie, X., Amand, T., Urbaszek, B. (2018), 'Colloquium: Excitons in atomically thin transition metal dichalcogenides', *Rev. Mod. Phys.* **90**, 021001.

Wilson, J.A., Yoffe, A.D. (1969), 'The transition metal dichalcogenides discussion and interpretation of the observed optical, electrical and structural properties', *Adv. Phys.* **18**, 193.

Winkler, R. (2003), *Spin-orbit coupling effects in two-dimensional electron and hole systems*, volume 191 of *Springer tracts in modern physics*, Springer, Berlin and New York.

Wissing, S.N.P., Eibl, C., Zumbülte, A., Schmidt, A.B., Braun, J., Minár, J., Ebert, H., Donath, M. (2013), 'Rashba-type spin splitting at Au(111) beyond the Fermi level: The other part of the story', *New J. Phys.* **15**, 105001.

Wissing, S.N.P., Schmidt, A.B., Mirhosseini, H., Henk, J., Ast, C.R., Donath, M. (2014), 'Ambiguity of Experimental Spin Information from States with Mixed Orbital Symmetries', *Phys. Rev. Lett.* **113**, 116402.

Wolverson, D., Crampin, S., Kazemi, A.S., Ilie, A., Bending, S.J. (2014), 'Raman Spectra of Monolayer, Few-Layer, and Bulk $ReSe_2$: An Anisotropic Layered Semiconductor', *ACS Nano* **8**, 11154.

Wortelen, H., Mirhosseini, H., Miyamoto, K., Schmidt, A.B., Henk, J., Donath, M. (2015), 'Tuning the spin signal from a highly symmetric unpolarized electronic state', *Phys. Rev. B* **91**, 115420.

Xiao, D., Liu, G.B., Feng, W., Xu, X., Yao, W. (2012), 'Coupled Spin and Valley Physics in Monolayers of MoS_2 and Other Group-VI Dichalcogenides', *Phys. Rev. Lett.* **108**, 196802.

Xiao, D., Yao, W., Niu, Q. (2007), 'Valley-Contrasting Physics in Graphene: Magnetic Moment and Topological Transport', *Phys. Rev. Lett.* **99**, 236809.

Yang, F., Wang, L., Wu, M.W. (2015), 'Hole spin relaxation in bilayer WSe_2', *Phys. Rev. B* **92**, 155414.

Ye, Y., Wong, Z.J., Lu, X., Ni, X., Zhu, H., Chen, X., Wang, Y., Zhang, X. (2015), 'Monolayer excitonic laser', *Nat. Photonics* **9**, 733.

Ye, Z., Cao, T., O/'Brien, K., Zhu, H., Yin, X., Wang, Y., Louie, S.G., Zhang, X. (2014), 'Probing excitonic dark states in single-layer tungsten disulphide', *Nature* **513**, 214.

Yeh, P.C., Jin, W., Zaki, N., Zhang, D., Liou, J.T., Sadowski, J.T., Al-Mahboob, A., Dadap, J.I., Herman, I.P., Sutter, P., Osgood, R.M. (2015), 'Layer-dependent electronic structure of an atomically heavy two-dimensional dichalcogenide', *Phys. Rev. B* **91**, 41407.

Yu, D., Math, C., Meier, M., Escher, M., Rangelov, G., Donath, M. (2007), 'Characterisation and application of a SPLEED-based spin polarisation analyser', *Surf. Sci.* **601**, 5803.

Yu, H., Yao, W. (2017), 'Valley-Spin Physics in 2D Semiconducting Transition Metal Dichalcogenides', in P. Avouris, T. Low, T.F. Heinz (eds.) '2D Materials: Properties and Devices', Cambridge University Press, Cambridge, 279.

Yuan, H., Liu, Z., Xu, G., Zhou, B., Wu, S., Dumcenco, D., Yan, K., Zhang, Y., Mo, S.K., Dudin, P., Kandyba, V., Yablonskikh, M., Barinov, A., Shen, Z., Zhang, S., Huang, Y., Xu, X., Hussain, Z., Hwang, H.Y., Cui, Y., Chen, Y. (2016), 'Evolution of the Valley Position in Bulk Transition-Metal Chalcogenides and Their Monolayer Limit', *Nano Lett.* **16**, 4738.

Zeng, H., Dai, J., Yao, W., Di Xiao, Cui, X. (2012), 'Valley polarization in MoS_2 monolayers by optical pumping', *Nat. Nanotechnol.* **7**, 490.

Zhang, C., Chen, Y., Johnson, A., Li, M.Y., Li, L.J., Mende, P.C., Feenstra, R.M., Shih, C.K. (2015), 'Probing critical point energies of transition metal dichalcogenides: Surprising indirect gap of single layer WSe_2: Nano letters', *Nano Lett.* **15**, 6494.

Zhang, X., Liu, Q., Luo, J.W., Freeman, A.J., Zunger, A. (2014a), 'Hidden spin polarization in inversion-symmetric bulk crystals', *Nat. Phys.* **10**, 387.

Zhang, X.X., Cao, T., Lu, Z., Lin, Y.C., Zhang, F., Wang, Y., Li, Z., Hone, J.C., Robinson, J.A., Smirnov, D., Louie, S.G., Heinz, T.F. (2017), 'Magnetic brightening and control of dark excitons in monolayer WSe_2', *Nat Nano* **12**, 883.

Zhang, Y., Chang, T.R., Zhou, B., Cui, Y.T., Yan, H., Liu, Z., Schmitt, F., Lee, J., Moore, R., Chen, Y., Lin, H., Jeng, H.T., Mo, S.K., Hussain, Z., Bansil, A., Shen, Z.X. (2014b), 'Direct observation of the transition from indirect to direct bandgap in atomically thin epitaxial $MoSe_2$', *Nat Nano* **9**, 111.

Zhang, Y., Ugeda, M.M., Jin, C., Shi, S.F., Bradley, A.J., Martín-Recio, A., Ryu, H., Kim, J., Tang, S., Kim, Y., Zhou, B., Hwang, C., Chen, Y., Wang, F., Crommie, M.F., Hussain, Z., Shen, Z.X., Mo, S.K. (2016), 'Electronic structure, surface doping, and optical response in epitaxial WSe_2 thin films', *Nano Lett.* **16**, 2485.

Zhao, H., Wu, J., Zhong, H., Guo, Q., Wang, X., Xia, F., Yang, L., Tan, P., Wang, H. (2015), 'Interlayer interactions in anisotropic atomically thin rhenium diselenide', *Nano Res.* **8**, 3651.

Zhao, W., Ghorannevis, Z., Chu, L., Toh, M., Kloc, C., Tan, P.H., Eda, G. (2013), 'Evolution of Electronic Structure in Atomically Thin Sheets of WS_2 and WSe_2', *ACS Nano* **7**, 791.

Zhong, H.X., Gao, S., Shi, J.J., Yang, L. (2015), 'Quasiparticle band gaps, excitonic effects, and anisotropic optical properties of the monolayer distorted 1T diamond-chain structures ReS_2 and $ReSe_2$', *Phys. Rev. B* **92**, 115438.

Zhou, Y., Scuri, G., Wild, D.S., High, A.A., Dibos, A., Jauregui, L.A., Shu, C., de Greve, K., Pistunova, K., Joe, A.Y., Taniguchi, T., Watanabe, K., Kim, P., Lukin, M.D., Park, H. (2017), 'Probing dark excitons in atomically thin semiconductors via near-field coupling to surface plasmon polaritons', *Nat. Nanotechnol.* **12**, 856.

Zhu, Z.Y., Cheng, Y.C., Schwingenschlögl, U. (2011), 'Giant spin-orbit-induced spin splitting in two-dimensional transition-metal dichalcogenide semiconductors', *Phys. Rev. B* **84**, 153402.

Zumbülte, A., Schmidt, A.B., Donath, M. (2015), 'Momentum resolution in inverse photoemission', *Rev. Sci. Instrum.* **86**, 013908.

Publications and Presentations *

Publications in Refereed Journals

Eickholt P., Krüger P., Stolwijk, S.D., Schmidt A. B., Donath M. (2016), 'Effects of orbital composition in a pair of spin-orbit-split surface bands at Tl/Ge(111)',

Phys. Rev. B **9**3, 085412.

Eickholt P., **Noky. J**, Schwier E.F., Shimada K., Miyamoto K., Okuda, T., Datzer C., Drüppel M., Krüger P., Rohlfing M., Donath M. (2018), 'Location of the valence band maximum in the band structure of anisotropic *1T'* - $ReSe_2$',

Phys. Rev. B **97**, 165130.

Eickholt P., Sanders C., Dendzik M., Bignardi L., Lizzit D., Lizzit S., Bruix A., Hofmann P., Donath M. (2018), 'Spin Structure of the *K* Valleys in Single-Layer WS_2 on Au(111)',

Phys. Rev. Lett. **121**, 136402.

Conference Presentations

Eickholt P., Stolwijk S.D., Schmidt A. B., Krüger P., Donath M. (2014), 'Spin-split surface states in the unoccupied electronic structure of Tl/Ge(111)-(1x1)', DPG Spring Meeting, Dresden.

* The presenting or corresponding authors are printed in bold face. The underlining marks the author of this thesis.

Eickholt P., Krüger P., Stolwijk S.D., Schmidt A. B., Donath M. (2016), 'Effects of orbital composition in a pair of spin-orbit-split surface bands at Tl/Ge(111)', DPG Spring Meeting, Regensburg.

Eickholt P., Datzer C., Miyamoto K., Schwier E.F, Noky J., Drüppel M., Krüger P., Rohlfing M., Donath M. (2017), 'Study of the anisotropic electronic structure of $ReSe_2$', DPG Spring Meeting, Dresden.

Eickholt P., Holtmann M., Sanders C., Hofmann P., Donath M. (2017), 'Direct observation of the conduction bands of single-layer WS_2 on Au(111)', DPG Spring Meeting, Dresden.

Eickholt P., Holtmann M., Sanders C.E., Dendzik M., Bianchi M., Hofmann P., Donath M. (2017), 'Single-Layer TMDC's on Au(111): Dispersion and Spin Structure of Conduction Bands (Poster)', Graphene Week, Athens.

Eickholt P., Holtmann M., Sanders C.E., Dendzik M., Bianchi M., Hofmann P., Donath M. (2017), 'Dispersion and Spin Structure of Conduction Bands of Single-layer TMDCs on Au(111)', AVS 64th International Symposium & Exhibition, Tampa.

Eickholt P., Holtmann M., Sanders C.E., Dendzik M., Bianchi M., Hofmann P., Donath M. (2018), 'Dispersion and spin structure of conduction bands of single-layer WS_2 on Au(111) (Poster)', 5th International Workshop on the optical properties of nanostructures, Münster.

Eickholt P., Bruix A., Holtmann M., Sanders C.E., Bianchi M., Hofmann P., Donath M. (2018), 'Spin structure of the K valleys in single-layer WS_2 on Au(111)', DPG Spring Meeting, Berlin.

Eickholt P., Bruix A., Holtmann M., Sanders C.E., Bianchi M., Bignardi L., Lizzit S., Hofmann P., Donath M. (2018), 'Spin structure of the K valleys in single-layer WS_2 on Au(111)', 14th International Conference on Electronic Spectroscopy and Structure (Poster), Shanghai.

Co-Authored Conference Presentations

Donath M., Stolwijk S.D. Eickholt P., Schmidt A. B.,Sakamoto K and Krüger P. (2014), 'Spin Chirality in Momentum Space for Surface States on Tl/Si(111) and Tl/Ge(111)', AVS 61th International Symposium & Exhibition, Baltimore.

Stolwijk S.D., Eickholt P., Sakamoto K., Schmidt A. B., Krüger P., Donath M. (2015), 'Spin Chirality in Momentum Space for Surface States on Tl/Si(111) and Tl/Ge(111)', DPG Spring Meeting, Berlin.

Krüger P., Förster T., Rohlfing M., Eickholt P., Schmidt A. B., Donath M. (2016), 'Spin-Orbit Induced Surface States of Rashba Systems and Topological Insulators', AVS 63th International Symposium & Exhibition, Nashville.

Noky, J., Drüppel M., Eickholt P., Deilmann T., Miyamoto K., Krüger P., Donath M., Rohlfing M. (2017), 'Band structure and excitons of monolayer and bulk $ReSe_2$: A many-body view', DPG Spring Meeting, Dresden.

Grenz, P., Eickholt P., Schmidt A. B., Miyamoto K., Sakamoto K., Donath M. (2018), 'Preparation and Characterization of a Monolayer Thallium on Si(110) (Poster)', DPG Spring Meeting, Berlin.

Musiol, L., Eickholt P., Donath M. (2019), 'The unoccupied electronic structure of 2H tungsten disulfide', DPG Spring Meeting, Regensburg.

Grenz, P., Eickholt P. , Miyamoto K., Schwier E.F., Okuda T., Donath M. (2019), 'Interplay of spin-orbit and exchange interaction in ultrathin Ni films on W(110)', DPG Spring Meeting, Berlin.

Student Award

The ICESS-14 (2018) student award at the fourteenth International Conference on Electronic Spectroscopy and Structure was granted for the work on "Spin structure of the K valleys in single-layer WS_2 on Au(111)".

Curriculum Vitae

Acknowledgment

Finally, I wish to thank all of those who supported me in carrying out the research and helped me during my PhD period.

Abschließend möchte ich mich bei allen Personen bedanken, die mich bei meiner wissenschaftlichen Arbeit unterstützt haben und mir während meines Promotionsstudium zur Seite standen.

- An erster Stelle geht mein Dank an **Prof. Dr. Markus Donath** für die Möglichkeit diese Arbeit in einem angenehmen Umfeld und unter guten wissenschaftlichen Bedingungen durchzuführen. Insbesondere möchte ich mich für die Möglichkeit der Teilnahme an den zahlreichen internationalen Konferenz- und Forschungsaufenthalte bedanken. Dass du jederzeit bereit warst über neu gewonnene Erkenntnisse zu diskutieren, hat mir sehr geholfen. Auch im Falle einer schwierigen Datenlage hat dieser stets positive Diskurs immer wieder zu hilfreichen Ideen und fruchtbaren Lösungen geführt. Ich habe diese lehrreiche und schöne Zeit sehr genossen!

- Bei Herrn **Prof. Dr. Peter Krüger** bedanke ich mich für die Bereitschaft die Ämter des Zweitbetreuers und Zweitgutachters zu übernehmen. Darüber hinaus danke ich für die Rechnungen, welche mir ein genaueres Verständnis der experimentellen Daten ermöglicht haben. Besonders hilfreich waren die vielen Diskussionen zur Bandstruktur, Spinpolarisation und anderen theoretischen Aspekten bei denen Sie mit großem Interesse stets auch experimentelle Aspekte diskutiert und berücksichtigt haben.

- Ich danke **Prof. Dr. Ursula Wurstbauer** für das Bereitstehen als dritte Prüferin.

- Bedanken möchte ich mich bei **Dr. Anke B. Schmidt** für die stete Bereitschaft Fragen zu beantworten. Die konstruktive Kritik bei der Erstellung von Präsentationen war immer eine große Hilfe, welche zum Erfolg beigetragen hat.

- Ein weiterer Dank gilt der **Arbeitsgruppe von Prof. Dr. Michael Rohlfing** für die Unterstützung von theoretischer Seite beim $ReSe_2$ Projekt. Insbesondere bedanke ich mich bei **Jonathan Noky**, der die Rechnungen maßgeblich durchgeführt hat und mit welchem ich in unermüdlicher Weise damit beschäftigt war das Zusammenspiel von theoretischen und experimentellen Ergebnissen zu verstehen.

- I am grateful to **Prof. Dr. Taichi Okuda**, **Dr. Eike Schwier** and the rest of the HiSOR team that was involved in my projects. A special thank you goes to **Assoc. Prof. Dr. Koji Miyamoto**, who not only supported me in Hiroshima, but also gave me experimental advise when he was in Münster.

- I am also thankful to the **research group of Prof. Dr. Philip Hofmann**, in particular to **Dr. Charlotte Sanders** and **Dr. Albert Bruix**, for providing the SL TMDC samples and helpful discussions.

- Eine wichtige Rolle haben **Werner Mai** und **Dr. Richard Heming** gespielt. Ihr habt dafür gesorgt, dass die Messelektronik auch im Störfall zügig wieder einsatzbereit war.

- Ob die Konstruktion von Probenträgern, die Wartung von Vakuumpumpen oder aber die Lösung von anderen diversen mechanischen Problemen,**Martin Hiller** ist dabei unabdingbar gewesen. Ich möchte auch dem gesamten Team der **feinmechanischen Werkstatt** meinen Dank zollen, die Konstruktionen und Reperaturen durchgeführt haben.

- Ich danke **Sabine Goßling** für ihre Hilfe bei bürokratischen Dingen. Du hast aber nicht nur für eine gute Organisation gesorgt, sondern auch mit

deiner guten Seele zu der hervorragenden Atmosphäre innerhalb der Arbeitsgruppe maßgeblich beigetragen.

- Mein Dank gilt auch meinen ehemaligen Büro- und Laborkollegen. **Dr. Sebastian Stolwijk** und **Dr. Henry Wortelen** haben mir hervorragend ihr Wissen weiter gegeben. Auch die Zeit gemeinsam mit **Katharina Ritter**, **Bernd Engelkamp**,**Andre Reimann** und **Fabian Schöttke** habe ich sehr genossen. Bei **Dr. Christian Datzer** möchte ich mich für die Zusammenarbeit an ELWIS und eine schöne Zeit (insbesondere in Hiroshima) bedanken.

- Hervorheben möchte ich **Pascal Grenz**, den ich gerne während seiner Bachelor- und Masterarbeit betreut habe. Du hast unser Büro und Labor bereichert.

- Mein Dank gilt zudem **Marcel Holtmann** und **Lukas Musiol**, die im Rahmen ihrer Bachelorarbeiten die Forschung über SL WS_2 vorangetrieben haben und auch über ihre Arbeiten hinaus apparativ stets bereit zu helfen waren.

- Die gesamte **AG Donath** hat dafür gesorgt, dass ich immer gerne gekommen bin und an die Zeit mit Euch mit Freude zurück denken werde!

- Ich bedanke mich bei **allen meinen Freunden**. Durch euch habe ich auch einmal den Kopf frei bekommen, um dann umso besser weiter forschen zu können.

- Für die bedingungslose Unterstützung vor und während des Studiums, möchte ich mich bei meiner Patentante **Barbara** bedanken.

- Ein großer Dank geht an meine Eltern **Claudia und Georg** und meine Schwester **Franziska**. Ihr habt mir stets in meiner persönlichen und beruflichen Entwicklung geholfen und mir den Rücken gestärkt.

- Ein ganz besonderer Dank gilt meiner Frau **Corinna**, die ich am Anfang meiner Promotionszeit kennen und lieben lernen durfte. Deine Geduld und dein Verständnis haben mir einen großen Rückhalt gegeben. Danke für die Liebe und die Kraft, ohne die ich das alles nicht geschafft hätte!